May 2023

Investigation into Strain Sensing with Reduced Graphene Oxide, and Applications in Low-cost Leak Detection and Health Monitoring of Water Equipment

Armin Yazdi
University of Wisconsin-Milwaukee

INVESTIGATION INTO STRAIN SENSING WITH REDUCED GRAPHENE OXIDE, AND APPLICATIONS IN LOW-COST LEAK DETECTION AND HEALTH MONITORING OF WATER EQUIPMENT

by

Armin Yazdi

A Dissertation Submitted in

Partial Fulfillment of the

Requirements for the Degree of

Doctor of Philosophy

in Engineering

at

The University of Wisconsin-Milwaukee

May 2023

ABSTRACT

INVESTIGATION INTO STRAIN SENSING WITH REDUCED GRAPHENE OXIDE, AND APPLICATIONS IN LOW-COST LEAK DETECTION AND HEALTH MONITORING OF WATER EQUIPMENT

by

Armin Yazdi

The University of Wisconsin-Milwaukee, 2023
Under the Supervision of Professor Nathan P. Salowitz

Strain gauges are one of the most important transducers that can be used in many applications such as robotics, structural health monitoring, medicine etc. The expensive mass production, as well as lack of high sensitivity, high strain tolerance or high quality can be some of the challenges with the current strain gauges. The reduced graphene oxide possesses many of the excellent properties of graphene while being easy and inexpensive to be mass-produced. However, its electromechanical behavior under strain (especially large strains) has not been well studied. In this dissertation, strain sensing by reduced graphene oxide with Polydimethylsiloxane substrate is investigated and the applications in low-cost leak detection and health monitoring of water equipment is explored.

Initial test results showed that with increase in area density of the graphene oxide of the reduced graphene oxide (rGO) sensor, the average strain tolerance of the sensor could be increased.

Resistive response of the sensor was tested in the directions aligned with, perpendicular to and at an angle with the direction of applied uniaxial tension up to 20.72% induced strain. The sensor showed mostly linear-nonlinear and increasing behavior in the directions aligned with the direction of applied tension. The linear behavior was consistent with the bulk-like material behavior and the nonlinear behavior was consistent with the percolative like behavior. Mathematical models also matched the increasing linear-nonlinear trend.

In the direction perpendicular to the direction of applied tension, sensor showed decreasing trend that could be due to contraction in the rGO caused by the Poisson's effect in the PDMS substrate. The mathematical model also showed an decreasing trend in the resistive response of the sensor in this direction.

In the direction that was at an angle with respect to the direction of the applied tension, sensor showed increasing resistive response similar to that in the aligned direction which was also explained with a mathematical modeling.

Cyclic analysis showed that generally the deviation in the resistive response of the sensor in the aligned direction between the first and the second cycles was significant compared to the deviation between other cycles. It could be attributed to the residual microcracks observed in the microscopic images forming after the first cycle of uniaxial tension.

Confocal and atomic force microscopic images also suggested the possibility of percolative behavior of rGO in higher strains and accumulation of rGO flakes creating cracks that could be linked to the nonlinear resistive response of the rGO.

Furthermore, a novel application of the rGO strain sensor in leak detection and health monitoring of the water equipment was explored and tested under different flowrates. Furthermore, creep, fatigue and high flowrate survival of the sensor were tested.

TABLE OF CONTENTS

LIST OF FIGURES

LIST OF TABLES

ACKNOWLEDGEMENTS

I would like to thank my supervisor, Professor Nathan P. Salowitz, for providing me with invaluable guidance and support throughout my doctoral studies. Additionally, I would like to thank my mother, father, wife, and other family members for their invaluable encouragement and support, without which this achievement would not have been possible.

This project was supported by The Water Equipment & Policy Research Center (WEP) located at University of Wisconsin-Milwaukee and Marquette University. WEP operates under the auspices of the National Science Foundation Industry/University Cooperative Research Center Program. This project was also mentored by following companies: Badger Meter and Zurn/Rexnord, Sloan, A.O Smith, Watts Water, GE Appliance and Pentair. Atomic Force Microscopy imaging was performed in Nanoscale Imaging and Analysis Center (NIAC) of Wisconsin Centers for Nanoscale Technology at University of Wisconsin Madison.

I also would like to thank anyone who may have assisted me in any way during my PhD research including but not limited to my current and former colleagues, the managers and staff in the University of Wisconsin Milwaukee (UWM)'s Machine Shop, Advanced Analysis Facility Laboratory, Structural Engineering Research Laboratory, Advanced Structures Laboratory and other laboratories, centers and facilities that have assisted me with their resources during this research.

1. INTRODUCTION

This chapter is an introduction to the history, definitions, importance, required basics and mechanism of strain sensors.

1.1. Motivation

Strain gauges are one of the most versatile and common transducers. Strain gauges directly and indirectly are employed to create sensors in many applications like robotic, structural health monitoring, human movement monitoring, pressure sensors, etc. They can transduce mechanical displacement or deformation into electrical signals. Two major types of strain sensors are resistive and capacitive strain sensors. Other types of strain sensors that are not as common as resistive and capacitive strain sensors are optical and piezoelectric [1].

1.2. Background

1.2.1. Definition of strain

Strain (ε) is a Geometric quantity that quantifies the relative deformation of the particles of an object. It is defined as deformation (Δl) divided by the initial length (l) as shown in equation (1-1). Strain is an unitless value and usually is expressed in percent [2]–[4].

$$\varepsilon = \Delta l / l \qquad (1\text{-}1)$$

According to Hook's law in mechanics of materials, strain can be calculated from stress (σ) divided by the Young's Modulus (E) (equation (1-2)) [2].

$$\varepsilon = \frac{\sigma}{E} \qquad (1\text{-}2)$$

Stress is defined as the force exerted on an object divided by its cross-section area and has the unit of force over area. (e.g N/m^2) [4]. In 3 dimensions a state of stress is characterized by 3 normal stresses plus either 3 shear stresses or a specific orientation.

1.2.2. Poisson's effect

Poisson's effect is the contraction of the object in the direction perpendicular to the direction of the applied force. Poisson's effect in a material can be evaluated with the Poisson's ratio which is a unitless value. It can be calculated as the negative value of the transverse strain divided by the strain aligned with the direction of applied force. This ratio is usually denoted by the letter ν and can be formulated as equation (1-3).

$$\nu = -\frac{strain\ in\ the\ transverse\ direction}{strain\ in\ the\ aligned\ direction\ with\ the\ applied\ force} \qquad (1\text{-}3)$$

1.2.3. Passive and Active sensors

Passive sensors are sensors that generate output signals themselves, employing energy from the stimuli. Thermocouples and piezoelectric sensors are some examples of this type of sensor. Active sensors on the other hand, require an external source of energy input to produce a signal. Strain gauges, thermistors and capacitive transducers are examples of this type [5]

1.2.4. Characteristics of strain sensors:

1.2.4.1. Gauges Factor

Gauge factor (GF) is a value by which the sensitivity of a strain gauge is determined. Gauge factor can be calculated by dividing change in resistance (ΔR) by initial resistance (R_0), all divided by strain (ε) that is applied to cause the relative resistance change ($\frac{\Delta R}{R_0}$) (equation (1-4)) [5].

$$GF = \frac{\frac{\Delta R}{R}}{\varepsilon} \qquad (1\text{-}4)$$

1.2.4.2. Maximum strain tolerance

The maximum strain tolerance is the strain which the sensor can function up to before failure. The strain sensors that tolerate high strains can be beneficial for applications like robotics, wearable electronics [1], [6]–[9].

1.2.4.3. Transfer function

Transfer function defines the equation relating a sensor's output signal to the stimulus. For instance, strain sensors when under strain create output signals. The output signal can be estimated by an equation relating the value of output signals to the applied strain's value. This equation can be linear or non-linear [5].

1.2.4.4. Fatigue

Fatigue characterizes the behavior of the sensor under cyclic load. It indicates how much the response of a sensor offsets from its initial state after a cyclic load is applied to it. In the case of strain sensors, a shift in the magnitude of the output signal can be observed when the strain sensor have been used for multiple cycles [10]

1.2.4.5. Creep

Creep is defined as permanent deformations in sensors after being in service for a long period of time [10]. Shift in output signal of a sensor can be resulted of a creep phenomenon.

1.2.5. Types of Strain sensors

1.2.5.1. Fiber optic strain gauges

This type of strain gauge measures strains based on changes in light transmission. Fiber optic strain sensors are very durable (can be used over a long time). Unlike resistive types, Fiber optic strain sensors are not effected by electromagnetic fields. One downside of this type of strain gauges is that they require high frequency optical equipment to create and interpret the signal. [11], [12].

1.2.5.2. Piezoelectric Strain Gauges

Piezoelectric strain gauges function based on piezoelectric effect that is the ability of generating an electrical charge displacement when subjected to mechanical deformation. This effect exists in a number of materials including lead zirconate titanate (PZT) and barium titanate. Piezoelectric strain gauges have the advantage of fast response time and the capability to be used as passive sensors (i.e. it produces enough electric energy to function). However, the output signal in this type dissipates very fast and needs to be used in high frequency stimuli application to be functional. Another limitation of piezoelectric materials is that they are usually brittle. Therefore, they can be used in limited applications [11], [13], [14].

1.2.5.3. Capacitive strain sensors:

To explain capacitive strain sensor, it is first necessary to know what capacitance is. Capacitance is the property of an electrical system. It can be described as the ability of an electrical system to store electrical charges. As is shown in equation (1-5), capacitance (C) can be defined as the relative permittivity of the dielectric material between two plates (e_r) multiplied by the

permittivity of vacuum (e_0) multiplied by the area of the plates the (A_p), all divided by the distance between two plates (d_p)..

$$C = \frac{e_r . e_0 . A_p}{d_p} \qquad (1\text{-}5)$$

There has been extensive research on capacitive sensing mechanisms over the past decades. It has become more popular due to its highly sensitive and contactless mechanism that offers low-cost solutions. It can be used in applications such as proximity and material analysis sensors [15]. To have a capacitive strain sensor, two conductive material and one dielectric material in between is required [9]. When the sensor is strained the capacitance of the conductors changes due to the change in their area. Also, the thickness of the dielectric layer in between is reduced causing decrease in the distance between two conductors [5], [16].

1.2.5.4. Resistive strain sensors:

A resistive sensor is made of a material whose resistivity changes when it is deformed. [5], [15].

Resistance (*R*) can be calculated by the equation (1-6), where *ρ*, *l, and A* are resistivity, length, and the cross-section area of the strain sensor respectively [5], [17]–[19]. Change in resistance is a combined result of change in the resistivity (ρ) and geometry (*l* and *A*).

$$R = \rho . \frac{l}{A} \qquad (1\text{-}6)$$

1.2.6. The history of strain gauges

1.2.6.1. Cemented wire type.

This type of strain sensor was the first generation of strain gauges that was introduced by Professor Arthur C. Ruge and his graduate student, Edward E. Simmons in 1938. It was made of

wire cemented to a specific type of paper that was used for cigarette production. Resistance of the wire could change with change in length and the cross-section area of the wire to measure strain according to equation [11]. These common foil strain gauges are passive sensors meaning they need voltage difference as the stimulus. Therefore, electrical energy is required for this type of strain sensor to function. The response of this type of strain sensor is linearly proportional to the strain (linear transfer function between strain and resistance). The gauge factor of this type of strain gauges is about 2 [11]

1.2.6.2. Foil strain gauges

During the World War II, this type of strain gauge was introduced and has been used ever since. Equation (1-6) is also valid for foil strain gauges [20]. Foil strain gauges usually have a zig-zag pattern. This feature helps the strain gauge have greater length of the conductive foil or wire. The greater the conductive foil or wire contributes to greater sensitivity to deformation according to equation (1-6). Foil Strain Gauges have two terminals which lead wires can be attached to, to measure voltage change across them. The response of this type of strain sensor is linearly proportional to the strain (linear transfer function between strain and resistance). The gauge factor of this type of strain gauges is about 2 [20].

1.2.6.3. Semiconductor strain gauges

Semiconductor strain gauges were introduced in 1957. This type of strain sensor has a crystalline structure. Electrical properties of the semiconductor strain gauges can be altered by introducing impurities with a method called doping. By doping, a strain gauge can be created that its resistance under tension decreases (n-type) or increases (p-type). Equation (1-6) is valid for this type of strain gauge where all 4 parameters can change including, ρ, l, w and t. The accuracy and

sensitivity of this type of sensor is greater than the foil and wire type strain gauges. The gauge factor of 100 to 200 have been reported for this type of strain gauge. Furthermore, semiconductor strain gauges possess high fatigue life compared to foil and wire types. Their strain survival can range from 1% to greater than 25% [21]–[24]. However, this type of strain gauge is expensive. Therefore, it is feasible to be used only in specific applications where accuracy and sensitivity are vital. The response of the sensor is nonlinearly proportional to the stimulus (nonlinear transfer function). Another limitation of this type of strain gauge is that they are highly fragile and prone to breakage [15], [25]–[29].

1.2.6.4. Nano-particle strain gauges

Nanoparticles are small materials with the size of 1 to 100 nm which are not visible by human eye. Because of their size and high surface area, they possess unique chemical, mechanical, and optical properties. Based on their size and shape and morphology they can be divided into several groups such as, Carbon based, metal based, semiconductor based etc. Over the last decades there has been significant progress in the field of nanotechnology and nanoparticle synthesis such as spinning, chemical vapor deposition (CVD) method, mechanical milling and chemical etching [30], [31].

Nanoparticle strain gauges have become more popular over the last decades due to their energy efficiency and high performance. They possess high sensitivity to strain with the GFs of two order of magnitude greater than foil or cemented wire types [27], [32]

Nanoparticle materials such as carbon nanotubes and graphene have high GF due to an excellent resistive property. In addition, researchers have found that nanostructured assemblies of

metallic strain sensors contribute to greater GF compared to their continues metallic wire counter parts. Furthermore, nanoparticle-based strain sensors have shown a high survivability to strains up to 50% [27], [32]. However, one of the issues of nanoparticle materials is their toxicity [33], [34]. Also, their synthesis and manufacturing are very expensive. The cost of component materials is usually high, coupled by the cost of controlled synthesis processes. These drawbacks make some other types, including the foil strain gauges the prevailing type in the market. However, nanoparticle-based strain gauges can still be tailored to specific applications.

1.2.6.5. Graphene

Recent studies suggest that graphene has many excellent properties such as excellent electrical conductivity, high strength to failure, high sensitivity to strain with GF about 200 reported and high strain tolerance up to 20% reported [35]–[40]. However its mass production is expensive unless the quality or uniformity is compromised [41], [42]. Graphene is monolayer hexagonal-structured material that contains sp^2 hybridized carbon atoms. Graphene can be derived from graphite using a simple "Scotch Tape Method". Graphite is composed of graphene layers stacked on the top of each other. In the scotch tape method, graphite flakes are exfoliated one after another until only one layer of graphene is left. This process is a very time-consuming process and requires a great deal of workforce for mass production. This issue resulted in invention of another method to make graphene indirectly using Hummer method [43]. The Hummer method creates graphene oxide directly using graphite, acids and oxidizing materials. Graphene oxide can also be produced using graphite oxidation and ball milling process [44] or high-shearing of pre-oxidized graphite [45]. However, the resulting graphene oxide product must be reduced to rGO. There are some methods including chemical vapor deposition [46] to make graphene directly [47].

1.2.6.6. Reduced graphene oxide

Reduced graphene oxide can be derived from graphene oxide sheets by losing the oxygen atoms from the surface [48]. Reduced graphene oxide (rGO) possesses many great properties of graphene including high sensitivity to strain and high strain tolerance while its synthesis can be inexpensive. rGO can be made from graphene oxide (GO) which is an abundant material. GO can be deposited on the substrate and easily be reduced to the rGO. One important deference between GO and rGO is their oxygen content. The ratio of carbon to oxygen in GO is very small making the oxygen the prominent element in it. Whereas the oxygen content of the rGO is close to zero [48]. One method to create rGO directly on the substrate is GO deposition followed by reduction of GO.

Deposition of GO can be performed by several methods, including drop casting by pipette [49]–[54], Spin coating [55], [56], layer by layer assembly method of Langmuir−Blodgett [57], [58]. Deposition of graphene oxide using Langmuir−Blodgett technique can be inconsistent. The shape and morphology of the deposited material can be different in different samples [59]. Spin coating is another method to deposit graphene oxide on the substrate using centrifugal force. The size of the substrate is one of the limitations of this method. Drop casting using pipette is a simple method that requires no complicated or expensive device. Controlling the thickness of the graphene layers in this method is difficult [49]–[54].

Reduction of GO to rGO can be performed using different methods including electrochemical, thermal and chemical reduction of GO. Some chemical methods to reduced GO involves hydrazine hydrate [60]. According to The National Institute for Occupational Safety and Health (NIOSH) [61], Hydrazine is a hazardous material and using it need special caution. Electrochemical

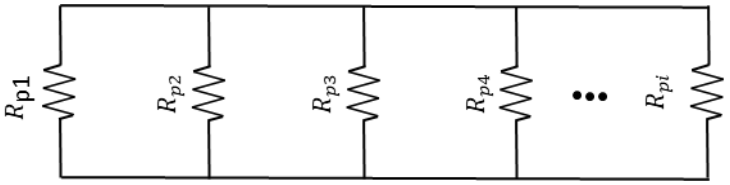

FIGURE 1-1. RESISTORS IN PARALLEL

reduction of GO can be complex [47], [62]. However, thermal reduction of GO can be relatively easy [49]–[54].

1.2.7. Arrangement of electrical components in series and parallel:

Many components like capacitors, resistors, or inductors of an electrical circuits can be used in series or parallel arrangements. By adding them in either series or parallel, their effects on the circuit may be different and values of electrical current, voltage difference and resistance would be different. For instance, considering resistors that are arranged in series like Figure 1-1, the total electrical resistance (R_{si}), current (I_{si}) and voltage difference V_{si} would be calculated by equation (1-7), (1-8), and (1-9) where *i* is the number of the component added to the circuit [17], [19], [63]. The total resistance ($R_{s,total}$) can be calculated as the superposition of the resistances.

$$R_{s,total} = R_{s1} + R_{s2} + R_{s3} + R_{s4} \dots R_{si} \quad (1\text{-}7)$$

$$V_{s,total} = V_{s1} + V_{s2} + V_{s3} + V_{s4} \dots V_{si} \quad (1\text{-}8)$$

$$I_{s,total} = I_{s1} = I_{s2} = I_{s3} = I_{s4} \dots I_{si} \quad (1\text{-}9)$$

However, if the resistors are connected in parallel (Figure 1-2), the total electrical resistances (R_{pi},) can be calculated as equation (1-10).

FIGURE 1-2. RESISTORS IN SERIES

$$\frac{1}{R_{p,total}} = \frac{1}{R_{p1}} + \frac{1}{R_{p2}} + \frac{1}{R_{p3}} + \frac{1}{R_{p4}} + \cdots \frac{1}{R_{pi}} \qquad (1\text{-}10)$$

Total electrical voltage differences (V_{pi}) can be calculated as equation (1-11)

$$V_{p,total} = V_{p1} = V_{p2} = V_{p3} = V_{p4} \ldots V_{pi} \qquad (1\text{-}11)$$

Total electrical currents (I_{pi}) can be calculated using Kirchhoff's current law combined by Ohm's law by equation (1-12)

$$I_{s,total} = I_{p1} + I_{p2} + I_{p3} + I_{p4} \ldots I_{pi} \qquad (1\text{-}12)$$

1.2.8. How resistance can be measured in resistive strain sensors

By change in the resistance of the strain gauge caused by the mechanical deformation or mechanical force, the voltage measurement would change consequently. The measured voltage difference can then be converted to resistance using Ohm's law (equation (1-13)) and Kirchhoff's laws (equation (1-14) and (1-15)). Equations (1-14) states that sum of current entering and leaving a junction are equal values and equation (1-15) shows that algebraic sum of voltage in a closed circuit is zero, where *Δv*, *R* and *I* are potential (voltage) difference, resistance and electrical current respectively. [5], [15], [17], [19], [63], [64]

$$\Delta v = RI \qquad (1\text{-}13)$$

$$\Sigma I_{entering\ a\ junction} = \Sigma I_{leaving\ a\ junction} \qquad (1\text{-}14)$$

$$\Sigma V_{closed\ circuit} = 0 \qquad (1\text{-}15)$$

Calculating resistance change and with the knowledge of the initial resistance, the change in resistance can easily be calculated.

1.2.8.1. Wheatstone Bridge

Wheatstone bridge is an electrical circuit that consists of 4 resistors. This device is used to calculate the unknow resistance in circuits using voltage measurements. Wheatstone bridge has multiple types of configurations such as full half, quarter Wheatstone bridges [17], [19], [63].

1.2.8.2. Wheatstone bridge types

1.2.8.2.1. QUARTER BRIDGE

In quarter bridge whose schematic is shown in Figure 1-3, only one of the resistors can vary by applying stimulus which in this case is a mechanical strain. This type of Wheatstone bridge has a relatively low sensitivity to the stimuli [20], [63], [65]. The *R* with subscripts *u* and *k* in Figure 1-3, Figure 1-4, and Figure 1-5 denote unknown (variable) and known resistances respectively.

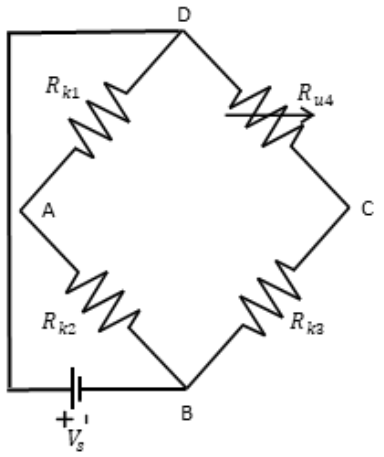

FIGURE 1-3. QUARTER WHEATSTONE BRIDGE

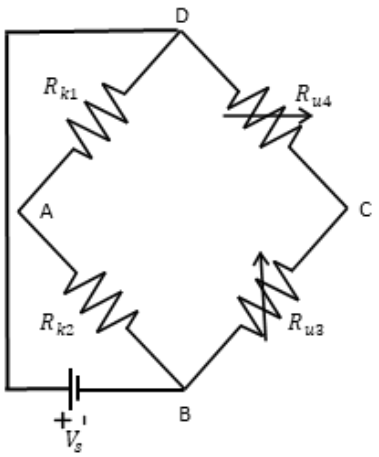

FIGURE 1-4. HALF WHEATSTONE BRIDGE

Voltage difference is measured between A and C. Using Ohm's Law and that the current passing through resistors in series at any point remains the same, the unknow resistance can be calculated [5], [19].

1.2.8.2.2. HALF BRIDGE

In half bridge-type (Figure 1-4), there are two resistors with variable resistances (e.g. two strain gauges). For instance, if two strain gauges are to be connected to a beam to be able to measure the strain in the bent position, they can be attached to both the front and back of the beam to show twice as much sensitivity as that of the quarter bridge. Also, this arrangement features

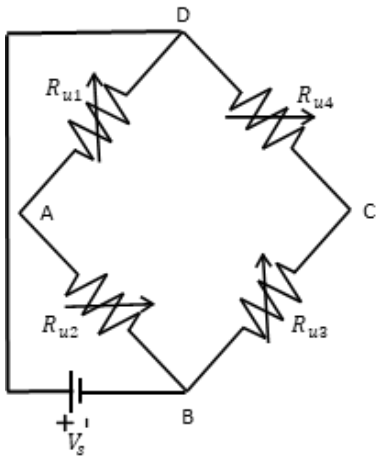

FIGURE 1-5. FULL WHEATSTONE BRIDGE

better temperature compensation. Using this arrangement, the front side strain gauge is stretched, and the back side strain gauge is contracted. The sign of the resistance of strain gauges attached to back and front are different. Because one of them is in compression (contraction) and the other in tension (extension). Using Ohm's Law and that the current passing through resistors in series at any point remains the same, the unknow resistances can be calculated [19], [63], [65].

1.2.8.2.3. FULL BRIDGE

In the full bridge structure (Figure 1-5), all 4 resistors have variable resistances. In this arrangement the sensitivity of the sensor is 4 times as that of quarter bridge. Another benefit of this arrangement is temperature compensation. Like quarter and half type bridges, using Ohm's Law and that the current passing through a set of resistors in series at any point remains the same, the unknown resistances can be calculated [63], [65].

1.2.9. Electrical conduction

Electrical conduction in classic physics is defined as the movement of charged particles such as electrons or charged atoms and molecules. In conductors such as copper or silver metal wires, the conduction happens by electrons as carriers. Electrical conductance's unit is Siemens. Electrical conductivity is the property of a material and is measured by Siemens/m [5], [17]–[19], [63], [64].

1.2.9.1. Valence electron

Inside atoms, electrons arrange themselves in shells. The outer shell of the atom is called valence shell. The electron in the valence shell is called valence electron. If the valence shell of the atom

is “closed”, it means that its outer shell is filled with electrons or has given all its valence electrons. Therefore, closed shells are very stable and do not seek chemical bonding with other atoms. Therefore, they are chemically inert. However, if the valence shell is open, it means that it is not completely filled with or emptied of electrons. Hence, it has the tendency to chemically bond with another atom/atoms. The outer shell plays a major role in many elements in electrical conduction of a material by gaining or losing electrons. However, in some elements of the periodic table, the valence electron is in the inner shell of the element.

1.2.9.2. Conductive materials

Conductive materials are materials that conduct electrical current by means of electrons or charged particles [5], [17]–[19], [63], [64].

1.2.9.3. Insulators

Insulators are materials that do not show any electrical conductivity like plastic materials [5], [17]–[19], [63], [64].

1.2.9.4. Semi conductive materials

Semiconductors are materials with crystalline structure and their electrical conductivity values are between insulator and conductor materials. Impurities can be introduced to semiconductors by doping to make them more conductive by creating p-type or n-type semiconductors. In p-type semiconductors, the prevailing number of carriers are electrical holes. Electron holes happen at the places where lack electrons that could potentially exist in. Conversely, in the n-types, the common carriers are electrons [5], [17]–[19], [63], [64].

Another difference between conductors and semiconductors is that with increase in temperature, electrical conductivity of conductors decreases as opposed to semiconductors whose electrical conductivity increases with increased temperature [5], [17]–[19], [63], [64].

1.2.10. Electrical Resistance and Resistivity

Electrical resistivity is the reciprocal of electrical conductance and means the level of resistance of the material to reduce or stop electrical current. The unit of the electrical resistivity is Ohm.m. The electrical resistance however is defined by resistivity of a material multiplied by its length and divided by its cross-section area equation(1-6) [5], [17]–[19], [63], [64].

1.2.11. Percolation theory

Percolation is a theory that characterizes the connectivity of objects or particles that are locally connected to form cluster like structures. Clusters can be defined as a group of objects or particles that are connected to the neighboring objects or particles. Percolation theory studies the probability of connection in the large scale to form clusters that span the entire system. The percolation theory is based on Power law and Scaling law. Percolation can be defined in two different models, The discreet site-bond model in which the spanning percolation can happen through interconnection of clusters that are composed of sites and bonds spanning across the system. The other model is the continuum model in which components are not formed in a certain geometrical lattice type arrangement. In this model sites are not discreetly arranged [66]–[77]

1.2.11.1. Scaling law

It defines how materials properties can change as the dimensions of them decrease. Considering the Hook's law, stress (σ) can be calculated from strain (ε) using Young's Modulus (E) by equation (1-16).

$$\sigma = E.\varepsilon \qquad (1\text{-}16)$$

Stress is defined as force (F) divided by the cross-section area (A) that the force is applied to. Equation (1-17) can be used to calculate the force applied to the material in terms of Young's modulus, the cross-section area and strain. In the context of scaling law, the strength of the material is proportional with characteristic dimension raised to the power 2 (D^2)

$$F = E.A.\varepsilon \qquad (1\text{-}17)$$

Weight, however, can be defined as density of the material (ω) times gravitational acceleration (g) times volume of the object (Volume). As a result, weight is proportional to D^3.

D is characteristic dimension, which can be defined as volume of a respective system on its surface area [78]–[80].

1.2.11.2. Power law

Conduction in materials with percolative behavior can follow the universal Power Law in which *n* is the percolation exponent, *t* is the thickness of the percolative film and t_c is the critical thickness of the material below which conductivity does not exist. The value of the *n* is dependent on several factors such as dimensionality and geometry of the constituents [68], [76], [81]–[89]

Conductivity in such materials with percolative behavior can follow the proportionality (1-18) [68], [76], [89], [90].

$$\sigma_{Percolative} \propto (t - t_c)^n \qquad (1\text{-}18)$$

The resistivity is the reciprocal of the conductivity, therefore, can be expressed with proportionality (1-19).

$$\rho_{Percolative} \propto (t - t_c)^{-n} \qquad (1\text{-}19)$$

1.2.11.3. Resistance in percolative material

Resistivity of some nanostructured materials like graphene nanosheets has been reported to be thickness dependent [68], [76]. The resistivity of such materials can change depending on the film's thickness. If the thickness of the film (t) is less than a certain value (t_{min}), the conductivity of film can be calculated as equation (1-20) [68], [76], [89], [90].

$$\sigma_{Percolative} = \sigma_{Bulk} * (\frac{t-t_c}{t_{min}-t_c})^n \qquad (1\text{-}20)$$

Therefore, the resistivity (reciprocal of conductivity) can be calculated by the difference between t_{min} and critical thickness (t_c) divided by the difference of the current thickness of the film and the critical thickness, all raised to the power n and multiplied by the bulk resistivity of the material (ρ_{Bulk}) as shown in equation (1-21)

$$\rho_{percolative} = \rho_{Bulk}(\frac{t_{min}-t_c}{t-t_c})^n \qquad (1\text{-}21)$$

The critical thickness of the film is the thickness below which no electrical conductivity exists. At this state of material, the number of conductive particles or flakes of the material are not enough to make conductive paths. Therefore, the material is insulated [68], [73], [76], [88], [89].

If the thickness of the film is less than t_{min} and larger than t_c, the resistance can be calculated by combining equations (1-6) and (1-21) to obtain equation (1-22)

$$R = \rho_{Bulk}\left(\frac{t_{min}-t_c}{t-t_c}\right)^n . \frac{l}{\text{w.t}} \qquad (1\text{-}22)$$

If the thickness of the film is more than t_{min}, electrical resistivity of the film is not dependent on the thickness. In that case, resistivity of the film may be modeled like a bulk like material and the resistance of the material may be calculated by equation (1-6). The resistivity of the film in this case can be denoted by ρ_{Bulk}.

2. INVESTIGATION INTO STRAIN SENSING WITH REDUCED GRAPHENE OXIDE

2.1. Introduction

In Chapter one, introduction about different types of strain gauges, how they have evolved over time, how they work and how they can be tailored to our needs are discussed. In this chapter challenges, objective, approaches, material and synthesis and major tasks are discussed in detail.

2.2. Challenges

Foil strain gauges can only tolerate strains up to 3 to 5% and cannot function in higher strains. The gauge factor of this type of strain sensor is about 2 [20]. The gauge factor of semiconductor crystalline structured strain gauges are high. However, they are fragile, expensive, and their strain tolerance can be as low as 1% (however in some cases it can be beyond 25%). Nanoparticle based strain gauges have showed high strain tolerance of up to 50% while possessing gauge factors ranging up to 200 [27], [37], [91], [92]. Scientists have expressed concerns about the toxicity of some nanoparticles [30], [34]. Also, the mass production of nanoparticles can be complex and expensive. Graphene has recently shown incredible electromechanical and high strain survival [91], [93]. However, its mass production is complex and expensive. Reduced graphene oxide has recently been found to benefit from many incredible properties of graphene as well, such as good electromechanical behavior and high strain survivability. Mass production of the rGO is easy and inexpensive [50]–[52], [54] in comparison to graphene. The rGO electromechanical properties

specifically in large strains and in different directions with respect to the direction of applied tension however are not well studied.

2.3. Objective

In this chapter the electromechanical properties of rGO in small and large strains in the direction aligned with (x), perpendicular to (y), and at an angle (d) with the direction of the applied tension is investigated.

2.4. Approach

In this study, rGO strain sensor was subjected to uniaxial tension creating strain in the sensor. Resistive responses of the sensor were investigated in different directions. Additionally, deformation in the sensor was explored using imaging methods like atomic force microscope and confocal microscope.

2.5. Major Tasks

In this section, methods, materials, synthesis of the sensor and the test set-ups for electromechanical testing of the sensor and imaging of the sensor under strain are presented.

2.5.1. Method

Tensile testing was performed on 42 sensors with 3 different average rGO area densities of 0.0069 mg/mm^2, 0.008 mg/mm^2 and 0.0091 mg/mm^2 (14 samples each) using INSTRON testing machine [94] to determine the average strains at which sensor electrically fail as well as the average sensitivity in the aligned direction with the direction of applied tension. Additionally, the effect of increasing area density of the GO on the average strain of electrical failure and the

average sensitivity was investigated. Only the aligned direction was investigated in this experiment because, according to initial investigations, sensor's resistive response usually showed electrical failure first in the aligned direction. Furthermore, in another test, 19 samples with the area density of 0.0069 mg/mm^2 were tested, up to about 20.72% strain. Resistive response was monitored in x, y and d directions. A 4-cycle testing was performed on 8 random samples (out of 19 samples). More investigation was performed on the samples using a camera, an atomic force microscope and a confocal microscope.

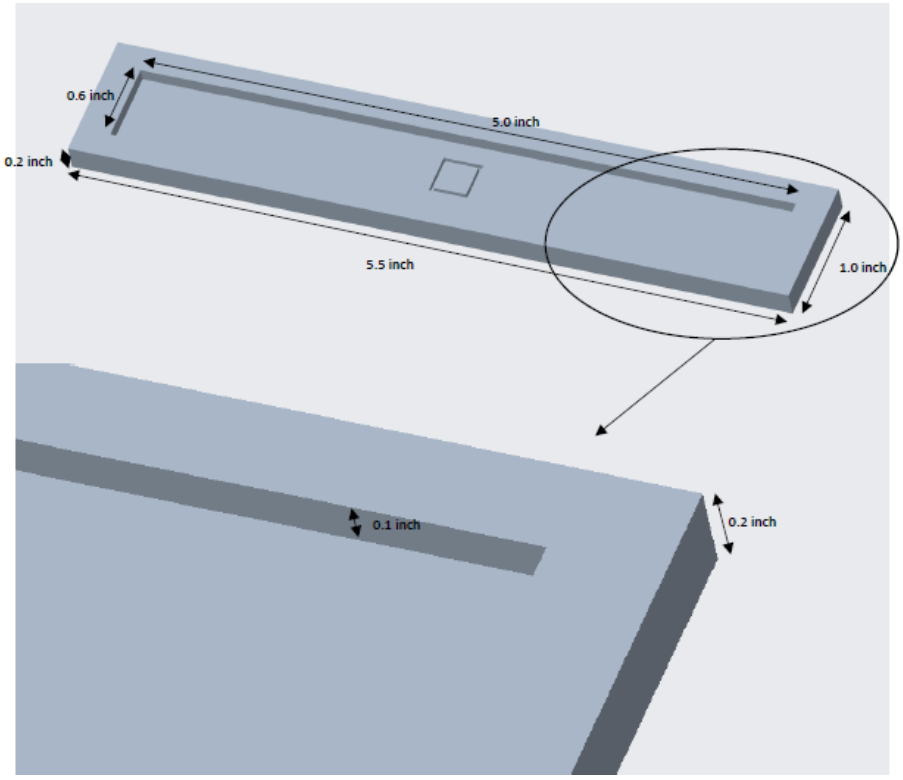

FIGURE 2-1. MOLDS CREATED TO CAST THE BODY OF THE SENSOR

2.5.2. Material and Synthesis

2.5.2.1. Electromechanical testing of the sensor

The sensor was composed of a body (substrate) made of Polydimethylsiloxane (PDMS) and a direct sensing element of reduced graphene oxide. Below is a detailed explanation of how the sensor was made [95], [96]. The PDMS silicone polymer was used for the body of the sensor because of its high flexibility and ease of use specially for prototyping purposes [97].

To synthesize the substrate of the sensor, molds were created. The Molds were designed by Creo PTC (Figure 2-1) and made using a Polycarbonate material. In the middle of the mold there was a cut to create a reservoir for the body of the sensor to contain the graphene oxide. The PDMS was cast into the mold and allowed to be cured in the room temperature for 3 days. To remove the bubbles from the PDMS, it was placed in a vacuum chamber for 80 min first and then cast into molds. SYLGARD 186 Silicone Elastomer (PDMS) was used [98]. The resulting product was cut out of the mold and washed completely by ultrapure deionized water and was dried with a

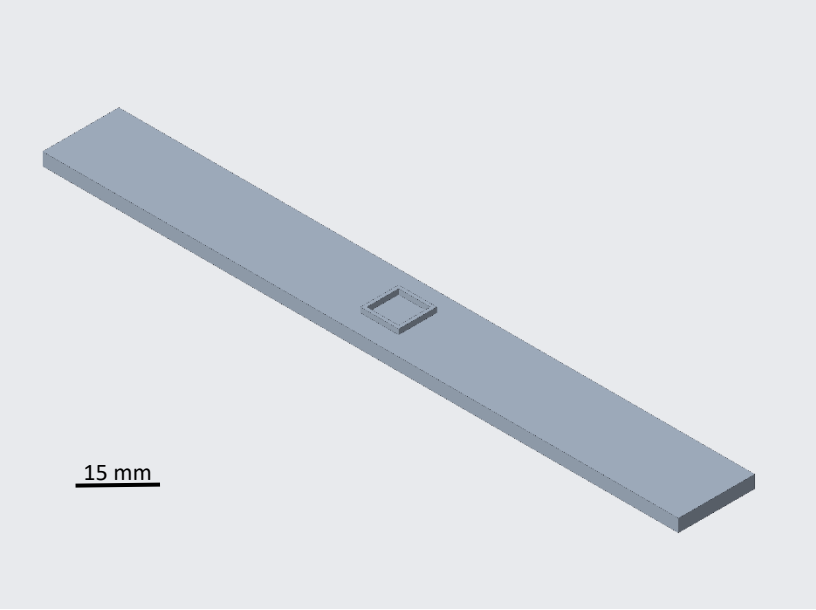

FIGURE 2-2. BODY OF THE SENSOR

fume hood's air fitting (Figure 2-2). The length, width, and thickness of the substrate were 127 mm, 15.24 mm, and 2.54 mm respectively. The small reservoir at the center of the substrate measured 6.35 mm x 6.35 mm. The thickness of the walls around the reservoir to contain the GO deposition was 0.635 mm with the height of 1.016 mm.

In the next step, before depositing the GO on the PDMS substrate, two processes were performed to enhance the adhesion of the PDMS so the GO can suitably be attached to it when deposited. First, PDMS substrate was treated with an O2-Plasma process. In order for the substrate to be treated with O2-Plasma, it was placed in a PE-25 plasma etching machine for 5 minutes [99]. Then the PDMS substrate was immersed in a solution of 2 part (3-Aminopropyl)triethoxysilane and 98 parts Ethanol for 3 hours [100].

To prepare the rGO sensor, graphene oxide (Graphenea 0.4 wt% GO dispersion in water) [101] was agitated in a Cole Parmer ultrasonic cleaner (M-series) for 2 minutes [102]. Graphenea graphene oxide dispersion was also characterized using two methods of ultraviolet–visible spectroscopy (UV Vis Spectroscopy) and the X-ray photoelectron spectroscopy (XPS) which are discussed later in section 2.5.2.3. in the dissertation. 0.0696 ml of the agitated graphene oxide suspension was drop-cast on reservoir of the substrate resulting in a 0.0069 mg/mm^2 area density of the solution of GO. The solution was allowed to be dried for 24 hours. The next step was

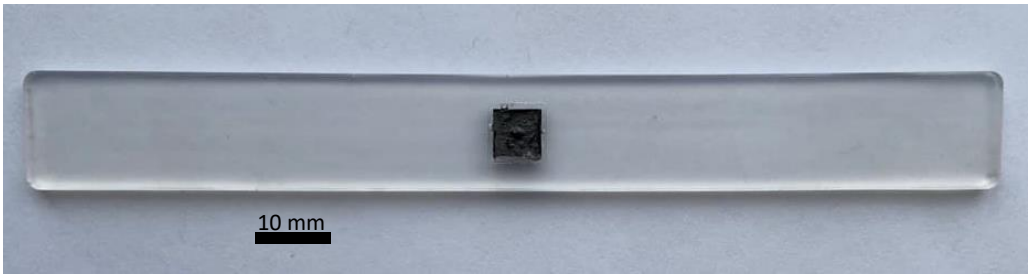

FIGURE 2-3. THE RESULTING SENSOR

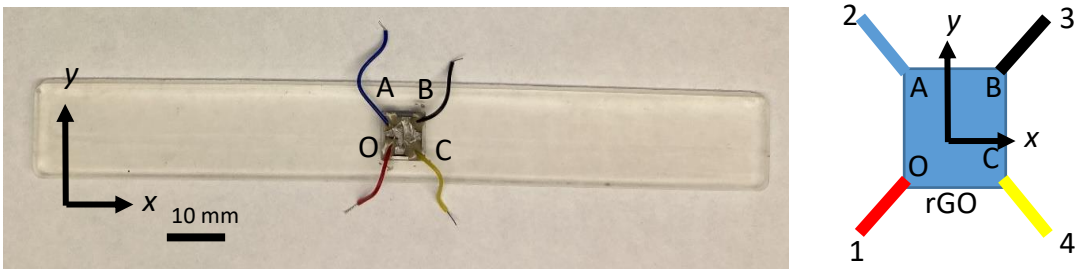

FIGURE 2-4. ARRANGEMENT OF THE ELECTRODES ATTACHED TO THE SENSOR TO COLLECT DATA

thermal reduction of the GO. This process was performed by an OTF-1200 Series Split Tube Furnaces [103] in an Argon environment. In the thermal reduction process, temperature was raised to 180˚c from room temperature in 60 min and kept at the same temperature in 60 min. Again, increased to 200˚c in 5 min and kept at the same temperature for 10 min. Finally brought back to the room temperature in 90 min. The resulting product is demonstrated in Figure 2-3. This overall processing was developed with the assistance and testing of Li-Chih Tsai and Maysam Rezaee and their work is presented in Tsai et al 2019 [51], Rezaee 2021 [104], Rezaee et al 2019 [50] and Rezaee et al 2021 [52].

To be able to read the data a TEKTRONIX-MDO3014 Oscilloscope [105] was used as the data acquisition system. 4 electrodes were added to the rGO sensor at each corner of the square of rGO patch as it is shown in Figure 2-4. Electrodes 1 2, 3 and 4 were attached at points O, A, B and C respectively. The electrode 1 was used as the hot point powered by Arduino Uno [106] using the 5-volt pin. Each of the other electrodes were used later to be used in an electrical divider structure to be able to read the output signal using the oscilloscope device. To be able to tension the samples, 4 plates were created using the 3D printer. The material that was used in the 3D printer was Polylactide (PLA). Each end of the substrates was sandwiched between two plates. The length, width and thickness of each plate was 15.24 mm, 15.24mm and 2.54 mm respectively.

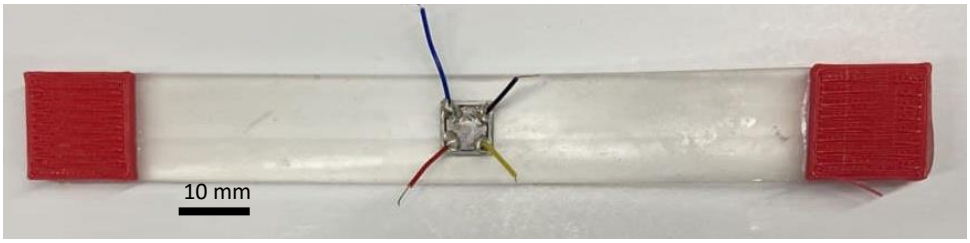

FIGURE 2-5. ADDED HANDLES TO THE SENSOR FOR THE SENSOR TO BE GRIPPED FOR TENSILE TESTING

The initial distance between grips in each sample measured 96.52 mm. After adding plates, the sensor was ready as is shown in Figure 2-5.

For the strain-of-electrical-failure tests (performed on 42 samples) and the tensile tests performed on 19 samples up to the 20.72% strain, distances between electrodes are provided in Table 2-1 and Table 2-2 respectively.

TABLE 2-1. DISTANCES BETWEEN ELECTRODES IN THE 42 SAMPLES UNDER STRAIN OF FAILURE TEST

	OC (mm)	Area Density (mg/mm2)
Sample 1	2.27	0.0069
Sample 2	1.48	0.0069
Sample 3	2.26	0.0069
Sample 4	1.64	0.0069
Sample 5	1.35	0.0069
Sample 6	2.95	0.0069
Sample 7	1.15	0.0069
Sample 8	2.47	0.0069
Sample 9	1.8	0.0069
Sample 10	2.23	0.0069
Sample 11	2.45	0.0069
Sample 12	2.3	0.0069
Sample 13	1.67	0.0069
Sample 14	2.17	0.0069
Sample 15	1.79	0.008
Sample 16	2.06	0.008
Sample 17	1.57	0.008
Sample 18	1.97	0.008
Sample 19	1.75	0.008
Sample 20	2.39	0.008
Sample 21	2.02	0.008

Sample 22	1.71	0.008
Sample 23	2.24	0.008
Sample 24	2.28	0.008
Sample 25	0.73	0.008
Sample 26	1.4	0.008
Sample 27	1.64	0.008
Sample 28	1.91	0.008
Sample 29	1.5	0.0091
Sample 30	0.84	0.0091
Sample 31	2.4	0.0091
Sample 32	0.73	0.0091
Sample 33	0.72	0.0091
Sample 34	1.74	0.0091
Sample 35	2.32	0.0091
Sample 36	2.11	0.0091
Sample 37	1.89	0.0091
Sample 38	1.51	0.0091
Sample 39	1.84	0.0091
Sample 40	1.38	0.0091
Sample 41	1.56	0.0091
Sample 42	1.88	0.0091

Strain in the direction aligned with the direction of applied tension for each increment of applied deformation using INSTRON machine was calculated using equation (1-1). Tension was applied at the pace of 0.1 mm per second and the data was collected at each 1 mm increment.

TABLE 2-2. DISTANCE BETWEEN ELECTRODE 19 SAMPLES UNDER TENSILE TEST

	OC (mm)	OA (mm)	OB (mm)	Area Density (mg/mm2)
Sample 1	1.66	2.33	4.36	0.0069
Sample 2	1.86	2.61	3.76	0.0069
Sample 3	1.6	2.1	4.77	0.0069
Sample 4	2.64	3.29	4.87	0.0069
Sample 5	1.66	1.67	3.84	0.0069
Sample 6	2.07	1.82	3.5	0.0069
Sample 7	1.02	1.99	3.71	0.0069
Sample 8	1.73	1.71	4.33	0.0069
Sample 9	1.04	2.39	3.74	0.0069
Sample 10	1.89	1.57	4.1	0.0069
Sample 11	1.62	1.5	3.52	0.0069

Sample 12	0.79	1.43	3.06	0.0069
Sample 13	2.33	1.42	3.47	0.0069
Sample 14	1.93	1.55	3.75	0.0069
Sample 15	1.55	2.2	4.53	0.0069
Sample 16	0.8	1.22	2.74	0.0069
Sample 17	1.18	0.97	3.05	0.0069
Sample 18	1.06	1.57	2.57	0.0069
Sample 19	0.85	1.38	3.16	0.0069

2.5.2.2. Imaging of the sensor under strain

Due to limitations in portability of the imaging device and the tensioning device to perform imaging while the sample is under tension using the INSTRON tensile testing machine, a portable tensioning device was designed and created to be able to tension the sensor and place it on the stage to be imaged. Therefore, the geometry of the body of the sensor itself was tailored for this specific purpose to fit the straining device. One cut at each edge of the sensor was created (Figure

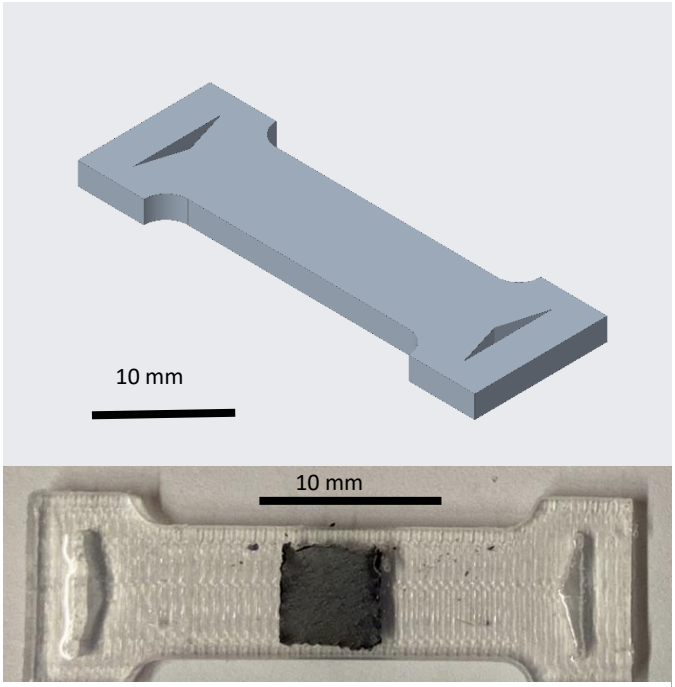

FIGURE 2-6. TO CUTS AT THE ENDS OF THE IMAGING SAMPLE TO FIT ON THE MANUAL TENSIONING DEVICE

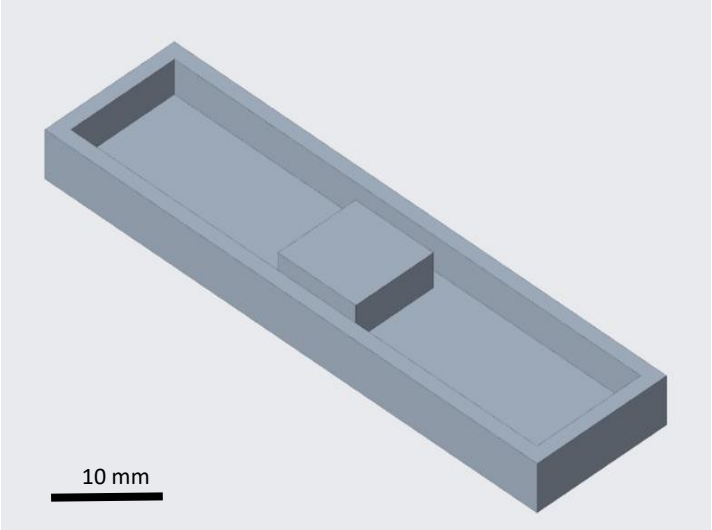

FIGURE 2-7. THE MOLD TO CREATE MASKS

2-6), using mold to be able to place the sensor in the tensioning device. In the early trials, it was realized that the wall of the reservoir in the center of the sensor that helped to contain the GO to ease the deposition, created an obstacle against imaging. In neither confocal telescope nor the atomic force microscope reaching out to the surface of the rGO became difficult (if not impossible) due to the wall around the rGO. Therefore, the reservoir was removed for this type of design. To tackle the problem of GO deposition without reservoir, deposition masks were used.

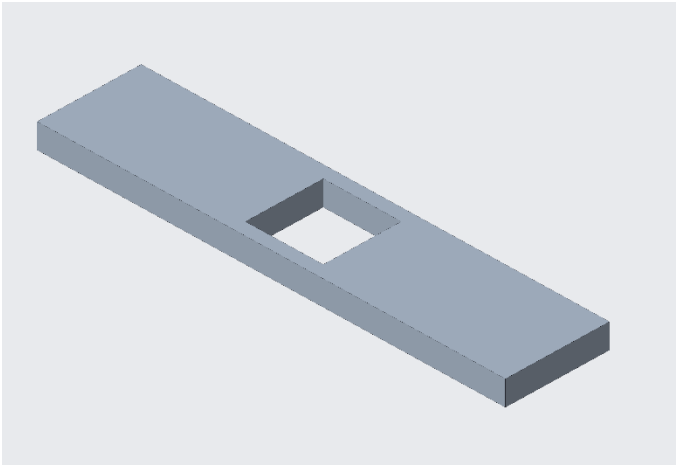

FIGURE 2-8. THE MASK TO CONTAIN THE GO DEPOSITED ON THE PDMS

The masks were created using the same material as the substrate to create more adherence between the mask and the substrate, so the GO did not leak out of the mask. The area of 7.62 mm by 7.62 mm was used to create the masking to create the GO deposition. Figure 2-7 shows the molds designed to create masks only for GO deposition into a square shape area of 7.62 mm by 7.62 mm and Figure 2-8 shows the resulting mask design. The remaining steps of the synthesis were similar with what was discussed before in section 2.5.2.1.

2.5.2.3. Characterization of the Graphenea-Graphene Oxide

Water solvent was used as the solvent to create the dispersion of GO and water, and no surfactant was used to create and stabilize the dispersion of GO in water because of contribution of the oxygen functional groups like hydroxyl, carboxyl etc. present in the GO that make the dispersion very stable without the need to use any surfactant [107]–[111]. Graphenea-graphene oxide dispersion used in the experiments was characterized using two

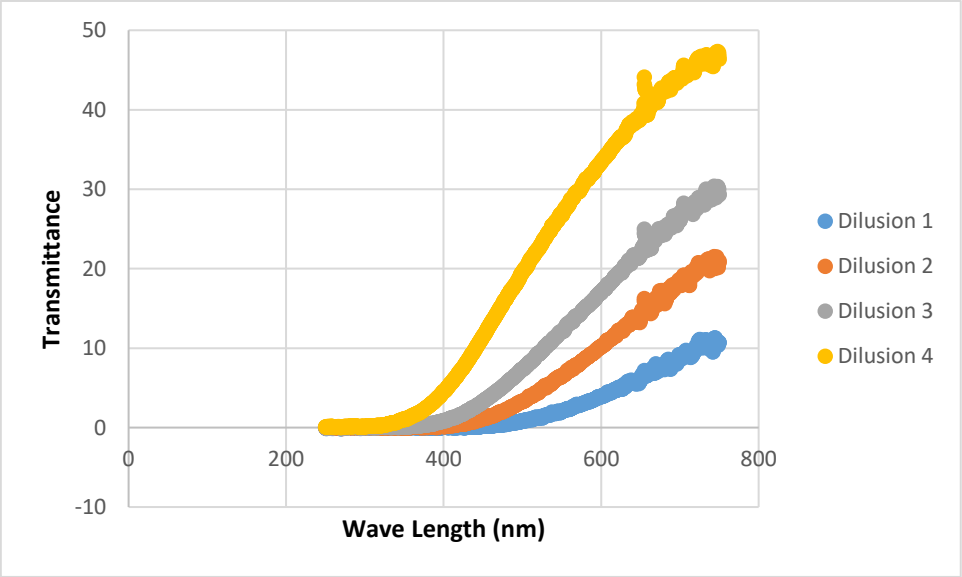

FIGURE 2-9. TRANSMITTANCE WITH RESPECT TO THE WAVELENGTH IN 4 DILUTIONS OF THE GRAPHENEA GO DISPERSION

methods including ultraviolet–visible spectroscopy (UV Vis Spectroscopy) and the X-ray photoelectron spectroscopy (XPS).

2.5.2.3.1. Ultraviolet–Visible Spectroscopy Results

UV Vis spectroscopy was performed on the Graphenea-graphene oxide dispersion. The original concentration was extremely high for the device to be able to transmit UV light. As a result, all the UV light would be absorbed by the GO dispersion making meaningful data collection impossible. Therefore, it was diluted with the ratios of 1ml of GO to 10ml (dilution 1), 15ml (dilution 2), 20ml (dilution 3) and 30ml (dilution 4) of deionized water (DI water). Figure 2-9 shows the results of UV Vis spectroscopy by plotting transmittance with respect to the wavelength for all 4 dilutions.

2.5.2.3.2. X-ray Photoelectron Spectroscopy Results

XPS was also performed on the dried Graphenea GO dispersion. Figure 2-10 shows the percentage of the elements present on the surface of the GO. S 2p, N 1s, O 1s and C 1s were present on the surface of the GO by 1.4%, 1.9%, 32.7% and 64.0% respectively.

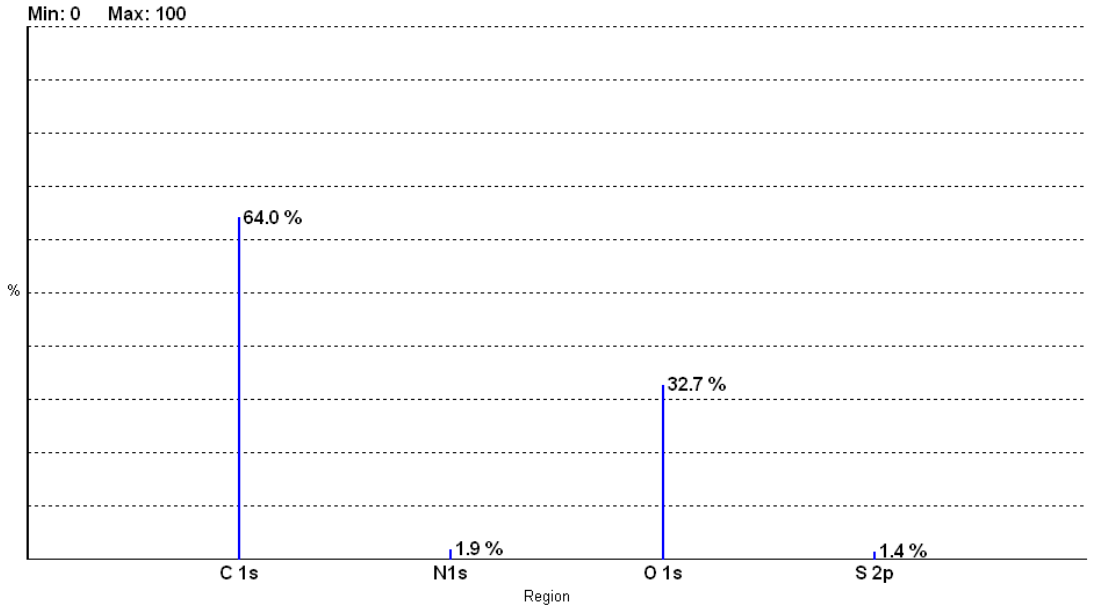

FIGURE 2-10. PERCENTAGE OF THE ELEMENTS PRESENT ON THE SURFACE OF THE DIRED GO DISPERSION

2.5.3. Test set-up and software used.

2.5.3.1. Electromechanical Testing

To perform the tensile test on the sensor, INSTRON 5980 Series Universal at University of Wisconsin-Milwaukee was used. Each end of the sensor was placed between the jaws of the INSTRON tensile testing machine and tension was applied at the rate of 0.1 mm/sec. Output signal was read at each 1mm-increment using the schematic shown in Figure 2-11. Each of the three resistors with the same Resistance (R) of 5600 Ω were connected in series to each of the unknown resistors between points A and ground (G), B and G, and C and G. At each 1 mm-applied tension, voltage between A and G (V_1), B and G (V_2) and cand G (V_3) were measured. Voltages less than 15 mv were considered as an electrical failure. The input excitation voltage at point O was 5v. Unknown Resistances R1, R2 and R3 were calculated using the equation (2-1) [5].

$$R_i = \left(\frac{5}{V_i} - 1\right) * R, i = 1, 2 \; and \; 3 \qquad (2\text{-}1)$$

The software that INSTRON used to interface with the computer was Bluehill Universal.

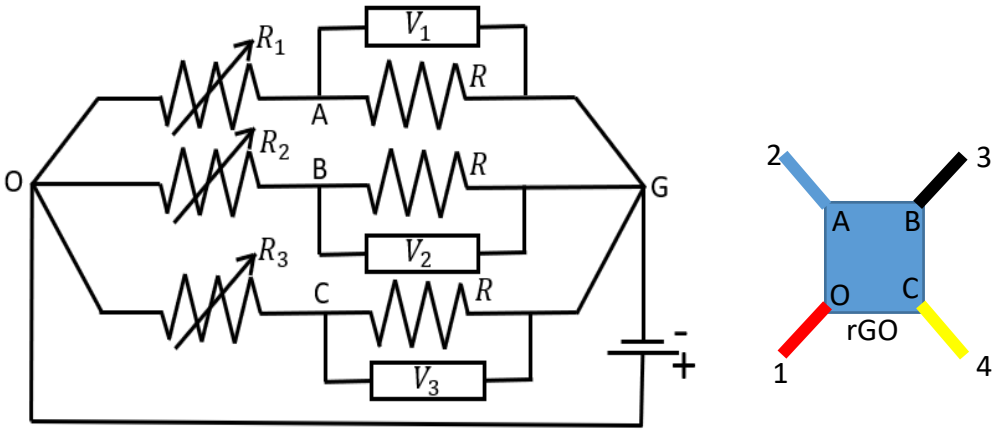

FIGURE 2-11. CIRCUIT USED TO COLLECT DATA COMPOSED OF UNKNOWN VARIABLE RESISTORS, KNOWN RESISTORS, ARDUINO 5 VOLT-VOLTAGE SUPPLY AND OSCILLOSCOPE TO MEASURE VOLTAGE DIFFERENCES

2.5.3.2. Imaging of the sensor under strain

Atomic Force Microscopy (AFM) investigation was performed using Bruker's Dimension Icon® Atomic Force Microscope. Tapping mode was used in the investigations. Two identical rGO-PDMS samples with the same substrate geometry and GO area density of 0.0069 mg/mm^2 were used to be able to perform the test on two identical and intact samples. Furthermore, imaging was performed using OLYMPUS OLS4100 3D laser microscope as well as taking pictures using camera (Canon DS126621).

To be able to image the samples, because of the limitations in simultaneous imaging and tensioning, tensioning devices (brackets) with known inducing strain were designed. The device were designed to apply tension to the samples to create estimated known strains based on the finite element simulation and analysis performed by ANSYS [112]. Finite element analysis (FEA) was performed to help the determination of the required sizing and spacing in the geometry of the tensioning devices to apply the estimated known strains on the sensor as indicated in Figure 2-12. Seven straining devices were designed and created using a 3D printer to create roughly 1.51%, 4.54%, 7.57%, 10.59%, 13.62%, 16.65%, and 19.68% strains at the center where rGO is present. Figure 2-13(a) shows the general geometry of the tensioning device. Figure 2-13(b) shows a picture of a sample tensioned on a bracket.

Furthermore, the change in the height difference between two pre-selected points (one on the substrate and the other on the rGO surface) were measured using a confocal microscope. Figure 2-14(a) and Figure 2-14(b) show the measurement locations on the sensors for sample 1 and sample 2 with 0.0069 mg/mm^2 area density respectively. Height difference measurement was performed using 50x lens on the confocal microscope.

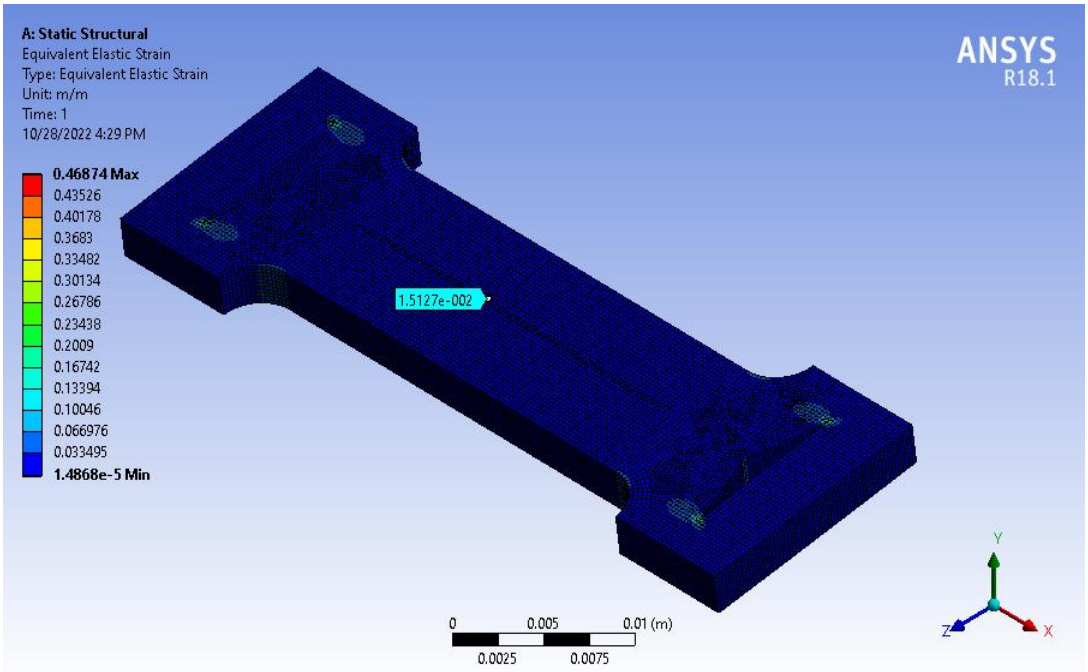

FIGURE 2-12 FINITE ELEMENT ANALYSIS PERFORMED ON THE SENSOR'S BODY

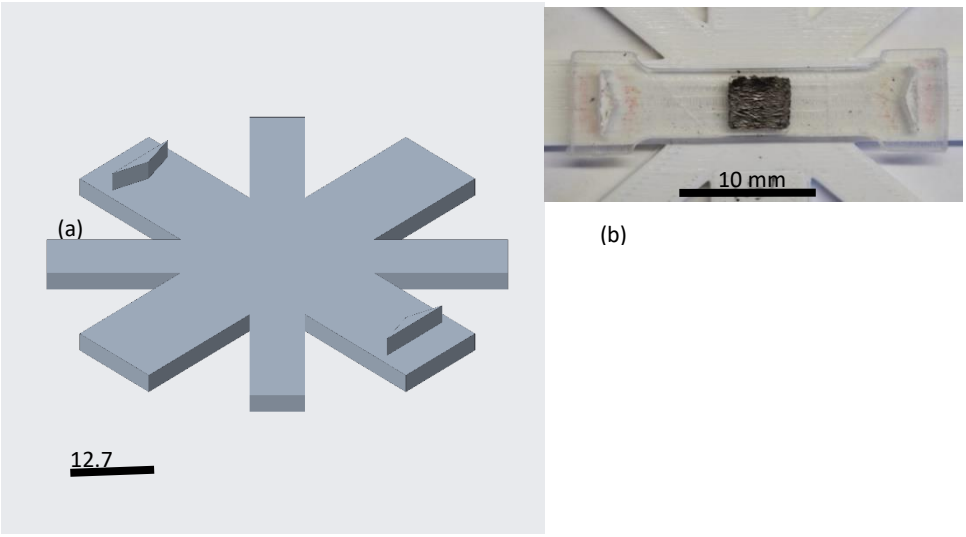

FIGURE 2-13. (A) GENERAL SHAPE OF THE TENSIONING DEVICE. (B) SAMPLE TENSIONED ON THE TENSIONING DEVICE

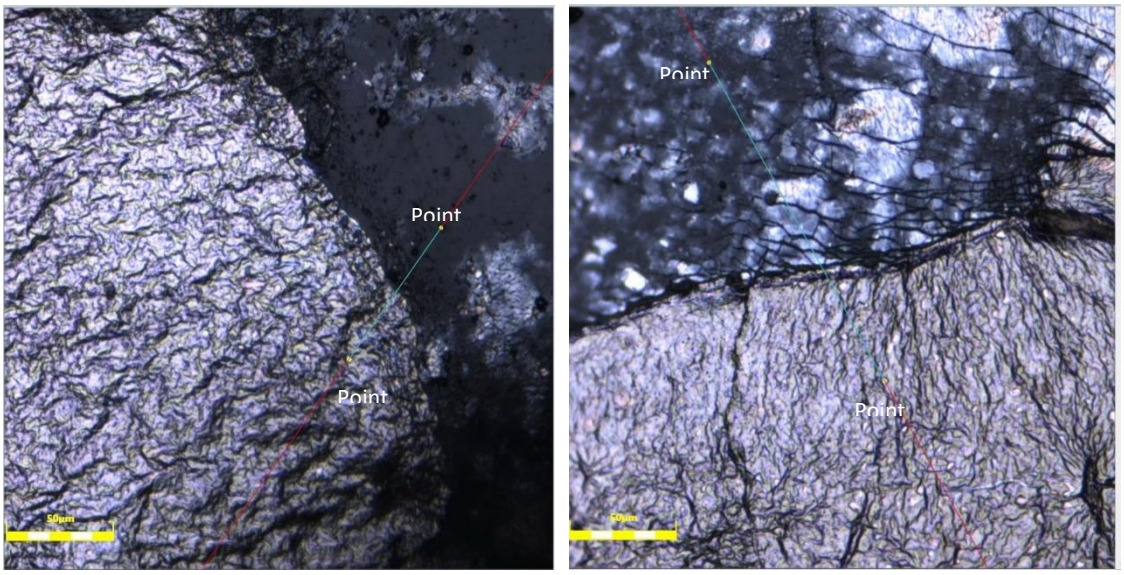

FIGURE 2-14. (A) LOCATION OF CONFOCAL MICROSCOPE MEASUREMENT ON THE SENSOR. (B) LOCATION OF CONFOCAL MICROSCOPE MEASUREMENT ON THE SENSOR

2.6. Results and Discussion

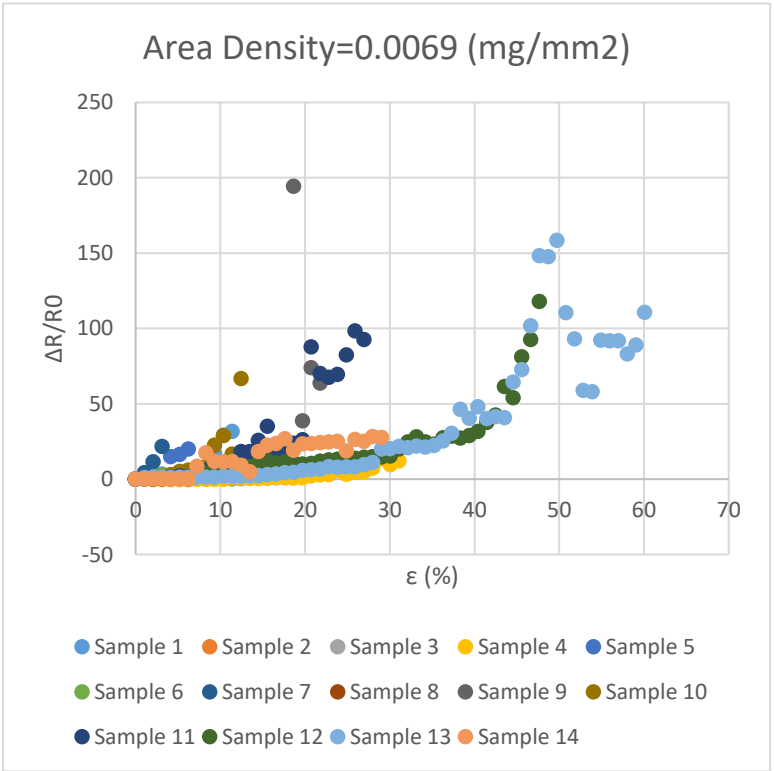

FIGURE 2-15. RESISTIVE RESPONSE OF THE SENSOR IN THE X DIRECTION UP TO THE ELECTRICAL FAILURE STRAIN IN 14 SAMPLES WITH 0.0069 MG/CM2 AREA DENSITY

In this section results of the experiments and investigations are discussed including, the test for determination of strain of failure (electrical failure), test on the electromechanical behavior of the rGO under limited strain, imaging of the rGO under strain using a camera, a confocal microscope and an atomic force microscope and measurements change in height difference between two points using the confocal microscope.

2.6.1. Strain of electrical failure test

Figure 2-15, Figure 2-16 and Figure 2-17 show the resistive response of the sensors up to the strain of electrical failure in samples with 0.0069, 0.0080, 0.0091 mg/mm^2 area densities respectively. The results show that as the area density increases, the maximum strain tolerance of the samples on average increases. 20.36%, 34.19% and 40.92% were the average strain values at which the samples with 0.0069, 0.0080, 0.0091 mg/mm^2 area densities, electrically failed

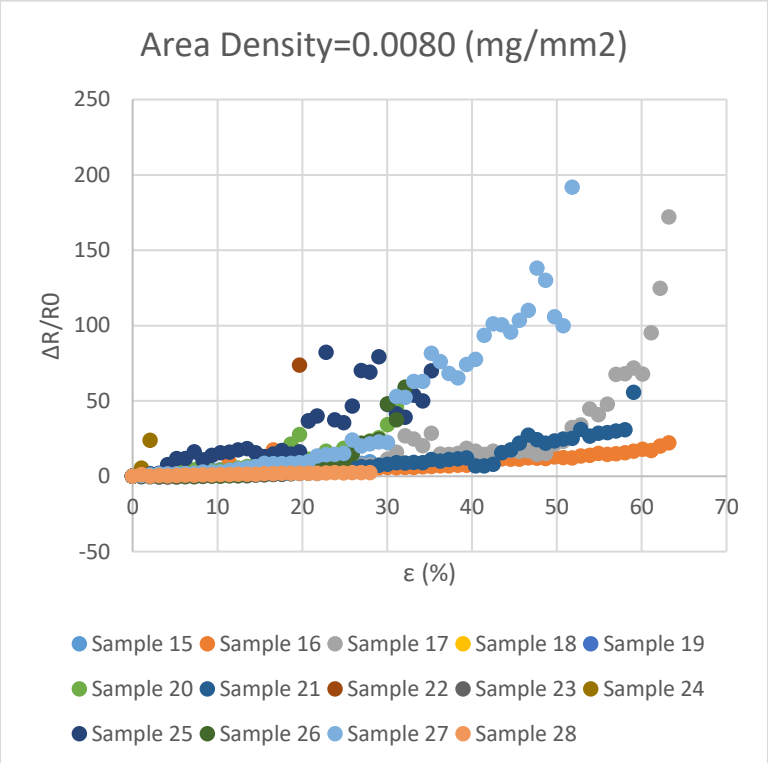

FIGURE 2-16. RESISTIVE RESPONSE OF THE SENSOR IN THE X DIRECTION UP TO THE ELECTRICAL FAILURE STRAIN IN 14 SAMPLES WITH 0.0080 MG/CM2 AREA DENSITY

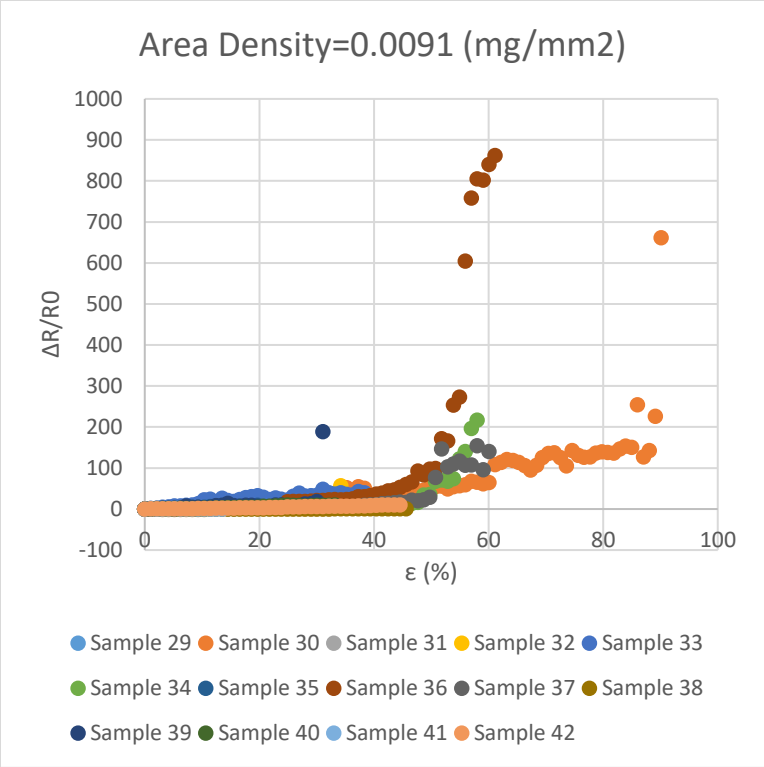

FIGURE 2-17. RESISTIVE RESPONSE OF THE SENSOR IN THE X DIRECTION UP TO THE ELECTRICAL FAILURE STRAIN IN 14 SAMPLES WITH 0.0091 MG/CM2 AREA DENSITY

respectively. Maximum strains of electrical failure in samples with 0.0069, 0.0080, 0.0091 mg/mm^2 area densities were about 60%, 63% and 90% respectively.

Furthermore, gauge factors were calculated with the linear fit approximation on the averaged value within the sensors with the same area densities. GF of 96.47$\frac{\Omega/\Omega}{m/m}$, 26.41$\frac{\Omega/\Omega}{m/m}$, and 31.32$\frac{\Omega/\Omega}{m/m}$, were calculated for samples with area density of 0.0069, 0.0080, 0.0091 mg/mm^2 respectively at the strain of 10.36%. GFs of 142.51$\frac{\Omega/\Omega}{m/m}$,, 52.31$\frac{\Omega/\Omega}{m/m}$, and 33.53$\frac{\Omega/\Omega}{m/m}$, were calculated at 20.72% strain for the same samples. This suggests that the sensitivity of the sensors generally decreased by increase in area density. However, with the greater area densities employed in the experiment, the GFs were still high enough to be considered as highly sensitive sensors compared to the common foil strain gauges with the GF of about 2. It is worth mentioning that all the

samples with 0.0069 mg/mm^2 showed linear-nonlinear resistive behavior. In other words, the resistive response of the sensor eventually at some point changed from linear trend to nonlinear trend. This observation was valid for more than 95% of the remaining samples with 0.0080 mg/mm^2 and 0.0091 mg/mm^2 area densities too.

2.6.2. Test on the electromechanical behavior of the samples in 3 directions under axial tension

2.6.2.1. Resistive response of the rGO in the x-direction

After tensile tests performed on 19 samples, this time in 3 different directions (x, y and at an angle) and up to 20.72% strain, 15 out of 19 samples survived the 20.72% strain. Out of these 15 samples, 12 samples showed linear-nonlinear behavior (Figure 2-18). The remaining 3 samples that survived the 20.72% strain showed only linear behavior as is shown in Figure 2-19. As demonstrated before, all the samples with 0.0069 mg/mm^2 area density, showed nonlinear resistive behavior eventually at a certain value of strain meaning that if the strain was continued

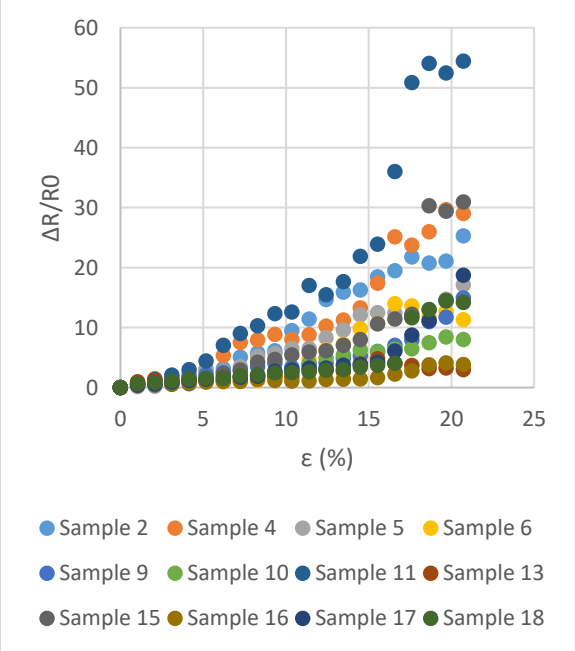

FIGURE 2-18. RELATIVE RESISTANCE CHANGE IN THE DIRECTION ALIGNED WITH THE DIRECTION OF THE APPLIED TENSION FOR 12 SAMPLES WITH LINEAR-NONLINEAR BEHAVIOR

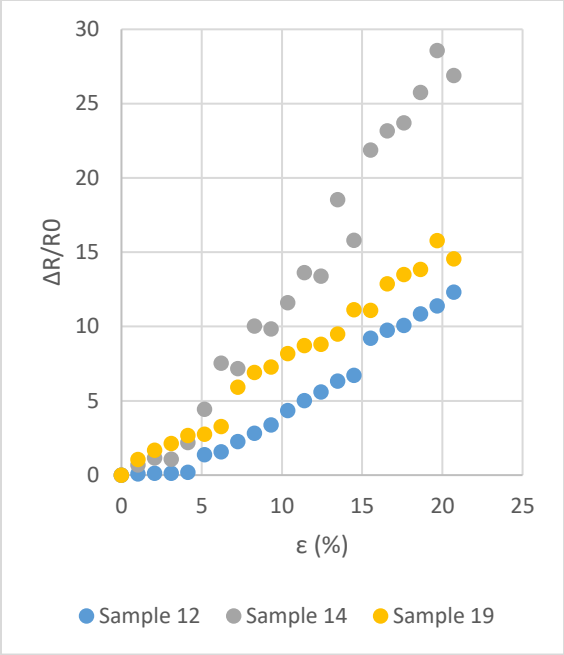

FIGURE 2-19. RELATIVE RESISTANCE CHANGE IN THE DIRECTION ALIGNED WITH THE DIRECTION OF THE APPLIED TENSION FOR 3 SAMPLES WITH ONLY LINEAR BEHAVIOR

increasing further (beyond 20.72%), at a certain strain the resistive behavior of these 3 samples would probably have changed to a nonlinear trend as well. As it is shown in Figure 2-20, 4 samples

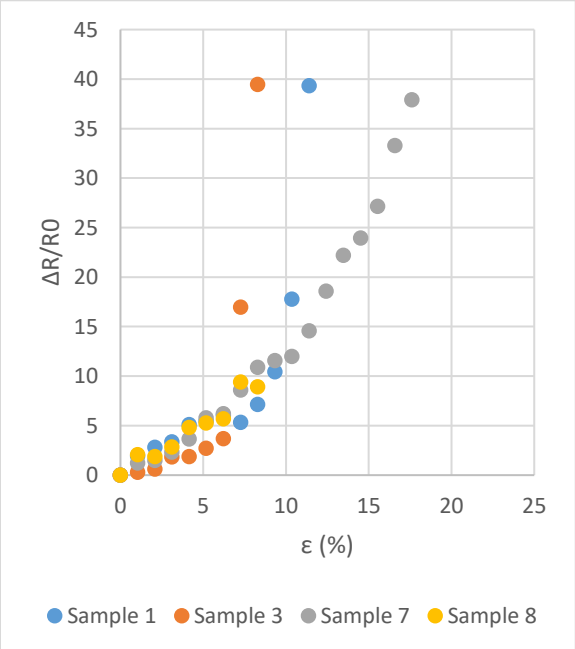

FIGURE 2-20. RELATIVE RESISTANCE CHANGE IN THE DIRECTION ALIGNED WITH THE DIRECTION OF THE APPLIED TENSION FOR 4 SAMPLES THAT SHOWED LINEAR-NONLINEAR BEHAVIOR AND SURVIVED THE STRAIN OF 20.72%

electrically failed before reaching 20.72% strain. As can be seen, all 4 samples showed nonlinear behavior before the electrical failure too.

Resistive response of the 12 sensors fell into two regions. A linear region followed by a nonlinear region. Looking at the resistive response of each of these 12 samples, relative resistance change increased with increase in the strain in the x direction and the trend was reasonably linear until a certain value (between about 3% and 12%). After this strain, while the increasing trend was still maintained, the relationship between strain and the relative resistance change altered to a non-linear relationship. The response in the linear region was consistent with that of bulk-like monolithic material strain gauges. The nonlinear resistive response suggested percolative behavior. To better express the resistive response of the sensor in two linear and nonlinear regions, a mathematical model can be developed as follows.

2.6.2.1.1. BULK LIKE RESISTIVE BEHAVIOR REGION (REGION 1) MATHEMATICAL MODEL

Using equation (1-6), resistance of the sample originally can be written as equation (2-2)

$$R_0 = \rho.\frac{l_0}{w_0 t_0} \qquad (2\text{-}2)$$

The length (l_ε) and width (w_ε) of the rGO film under strain can be calculated as equations (2-3) and (2-4) where ε is the strain in the direction aligned with the direction of applied tension [2], [4], [15], [25], [26].

$$l_\varepsilon = l_0(1+\varepsilon) \qquad (2\text{-}3)$$

$$w_\varepsilon = w_0(1-\nu.\varepsilon) \qquad (2\text{-}4)$$

Assuming the rGO as a material composed of flakes instead of a solid continuous material, its constituents can move over each other and be rearranged instead of being stretched under strain. It means that with change in the length and width of the rGO, the same volume will be occupied by the flakes as it did originally without application of strain. Therefore, by setting the new volume of flakes equal to the original volume, average thickness of the film under strain (t_ε) can be calculated by equation (2-21) [68], [76].

$$t_\varepsilon = \frac{t_0}{(1+\varepsilon)(1-\nu*\varepsilon)} \qquad (2\text{-}5)$$

Using equations (1-6), (2-3), (2-4), and (2-5), resistance of the rGO in the x direction under strain can be obtained from equation (2-6)

$$R_\varepsilon = \rho.\frac{l_0(1+\varepsilon)}{w_0(1-\nu.\varepsilon).\frac{t_0}{(1+\varepsilon)(1-\nu*\varepsilon)}} = \rho.\frac{l_0(1+\varepsilon)^2}{w_0.t_0} \qquad (2\text{-}6)$$

The difference between resistance under strain and the initial resistance of the rGO under strain can be expressed as equation (2-7)

$$\Delta R = \rho.\frac{l_0(1+\varepsilon)^2}{w_0.t_0} - \rho.\frac{l_0}{w_0 t_0} = \rho.\frac{l_0}{w_0 t_0}\ [2\varepsilon + \varepsilon^2] \qquad (2\text{-}7)$$

Relative resistance change can then be expressed as equation (2-8)

$$\frac{\Delta R}{R_0} = 2\varepsilon + \varepsilon^2 \qquad (2\text{-}8)$$

In the range that the strain was applied in the first region of the experiments ($0 < \varepsilon < 0.12$), a linear and increasing graph can be fitted in equation (2-8) with a high coefficient of determination between 99.98% and 100%. In other words, the mathematical model matched the resistive behavior of the rGO in the first region with linear and increasing trend. Even for the 3 samples with only-linear resistive response up to the 2.72% strain (that would probably show nonlinearity in the resistive response at higher strains), even if nonlinearity occurred at 100% strain (very unlikely) the coefficient of determination for the linear fit would have been 99.25% which still was very close to a linear trend.

2.6.2.1.2. PERCOLATIVE LIKE RESISTIVE BEHAVIOR REGION (REGION 2) MATHEMATICAL MODEL

In the second region, assuming, thickness dependency of the resistive response of the rGO,

By substituting l_ε, w_ε and t_ε into equation (1-22), the resistance of the film under tension can be calculated as equation (2-9).

$$R_\varepsilon = \rho_{Bulk}\left(\frac{t_{min}-t_c}{t_\varepsilon-t_c}\right)^n * \frac{l_0(1+\varepsilon).(1+\varepsilon).(1-\nu*\varepsilon)}{w_0.(1-\nu*\varepsilon).t_0} \qquad (2\text{-}9)$$

By rearranging, the equation (2-10) can be obtained.

$$R_\varepsilon = \rho_{Bulk}\left(\frac{t_{min}-t_c}{t_\varepsilon-t_c}\right)^n * \frac{l_0(1+\varepsilon)^2}{w_0 t_0} \qquad (2\text{-}10)$$

Original resistance (R_0) can be calculated as equation (2-11) by substituting l_0, w_0 and t_0 into length, width and thickness in equation (1-22).

$$R_0 = \rho_{Bulk}\left(\frac{t_{min}-t_c}{t_0-t_c}\right)^n * \frac{l_0}{w_0 t_0} \qquad (2\text{-}11)$$

The difference between resistance of the film under strain and in the original state can be calculated as equation (2-12).

$$R_\varepsilon - R_0 = \rho_{Bulk}\frac{l_0}{w_0 t_0}(t_{min}-t_c)^n\left(\frac{(1+\varepsilon)^2}{(t_\varepsilon-t_c)^n} - \frac{1}{(t_0-t_c)^n}\right) \qquad (2\text{-}12)$$

Finally relative resistance change can be calculated as equation (2-13).

$$\frac{\Delta R}{R_0} = \frac{R_\varepsilon-R_0}{R_0} = (1+\varepsilon)^2.\left(\frac{t_0-t_c}{t_\varepsilon-t_c}\right)^n - 1 \qquad (2\text{-}13)$$

The nonlinearity seen in the second region in Figure 2-18 can be attributed to the nonlinearity exists in equation (2-13) with the exponents 2 for $(1+\varepsilon)$ and n for $\left(\frac{t_0-t_c}{t_\varepsilon-t_c}\right)$ that shows that relative

resistance change has a nonlinear relation with the thickness of the film under strain and the strain itself in the direction aligned with the direction of the applied tension.

Additionally, by taking derivative of the average thickness with respect to ε from equation (2-5) to obtain the equation for the slope of the average thickness, equation (2-14) can be obtained.

$$\frac{dt_\varepsilon}{d\varepsilon} = -t_0 \frac{1-2\nu.\varepsilon-\nu}{(1+\varepsilon)^2(1-\nu.\varepsilon)^2} \qquad (2\text{-}14)$$

Considering the range of strain values that the sensor is under in the aligned direction and the Poisson's ratio value of the PDMS, and that the denominator of the fraction on the right side of equation (2-14) is a positive value, the value of this equation (2-14) is a negative value. It means that in both linear and nonlinear regions the average thickness decreases by increase in strain in the x direction.

Considering equation (2-13) for relative resistance change, and knowing that the average thickness decreases with increase in strain in the x direction, and that the t_0, t_c and n are values with a positive sign [76], and t_c is less than or equal to t_ε, it can be concluded that the $(\frac{t_0-t_c}{t_\varepsilon-t_c})^n$ increases with increase in strain. As a result, with increase in strain, $\frac{\Delta R}{R_0}$ increases (according to equation (2-13)). The nonlinearity and increasing trend seen in equation (2-13) in the range that strain is induced in the x direction, is consistent with the nonlinearity and increasing trend shown on the plot in Figure 2-18.

Also, it was noticed that the electrical failure of the resistive response usually occurred in the x direction first.

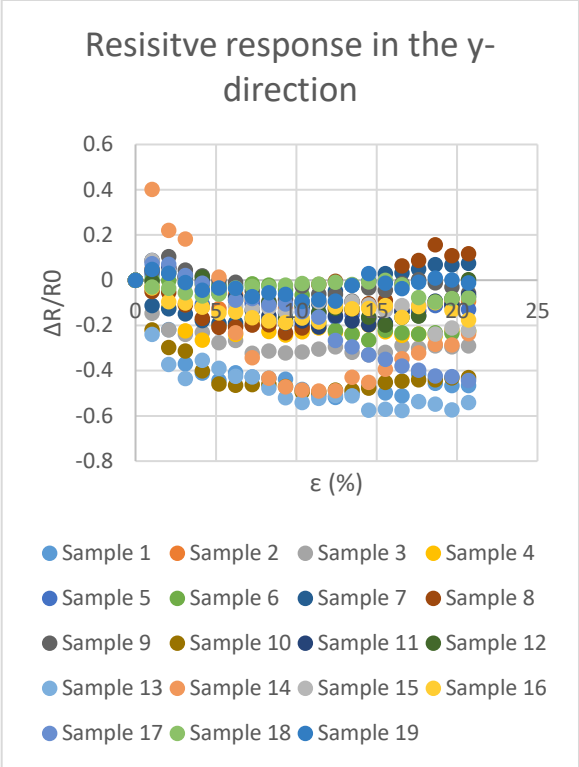

FIGURE 2-21. RELATIVE RESISTANCE CHANGE IN THE DIRECTION PERPENDICULAR TO THE DIRECTION OF APPLIED TENSION.

2.6.2.1.3. GAUGE FACTOR QUANTIFICATION OF RGO-BASED STRAIN GAUGE

The rGO strain gauge showed the gauge factor of 91.503 averaged over all the samples calculated with a linear fit approximation which is significantly greater than that of common metal foil strain gauges with GF of about 2.

2.6.2.2. Resistive response of the rGO in the direction perpendicular to the direction of applied tension

As is shown in Figure 2-21, the general trend of the plot was decreasing which could be due to contraction in the rGO in the direction perpendicular to the direction of the applied tension caused by Poisson's effect of the PDMS. However, in some of the samples, partially increasing

trends were observed which could be attributed to the local cracks forming aligned with the direction of the applied tension creating local disconnections in the interconnection between flakes in the direction perpendicular to the direction of applied tension. These cracks will be discussed more later when the imaging of the samples is discussed.

Equation (2-15) can be derived from Ohm's law (equation (1-6) by replacing the roll of width and length of the rGO film investigating the mathematical model of the resistive response of the sensor in the y direction:

$$R_y = \frac{\rho.w}{l.t} \qquad (2\text{-}15)$$

2.6.2.2.1. BULK LIKE RESISTIVE BEHAVIOR REGION (REGION 1)

The following mathematical model can be suggested in the first region. By combining equations (2-3), (2-4), (2-5) and (2-15), equation (2-16) can be obtained for resistance in the y direction.

$$R_y = \rho.\frac{w_0(1-\nu.\varepsilon)}{l_0(1+\varepsilon).\frac{t_0}{(1+\varepsilon)(1-\nu*\varepsilon)}} = \rho.\frac{w_0(1-\nu.\varepsilon)^2}{l_0.t_0} \qquad (2\text{-}16)$$

Assuming no thickness dependency in the resistive response in this region, relative resistance changes in the Y direction ($\frac{\Delta R}{R_{y_0}}$) can be obtained using equation (2-17) where R_{y_0} is original resistance in the y direction and can be obtained by setting ε to zero in equation (2-16).

$$\frac{\Delta R}{R_{y_0}} = \frac{R_y - R_{y_0}}{R_{y_0}} = (1-\nu.\varepsilon)^2 - 1 = \nu^2.\varepsilon^2 - 2\nu.\varepsilon \qquad (2\text{-}17)$$

Taking the derivative of this equation with respect to ε, the slope of the $\frac{\Delta R}{R_{y_0}}$ can be obtained by equation (2-18).

$$\frac{\partial(\frac{\Delta R}{R_{y_0}})}{\partial \varepsilon} = 2\nu^2.\varepsilon - 2\nu \qquad (2\text{-}18)$$

This equation is representative of the slope of the $\frac{\Delta R}{R_{y_0}}$ as the function of the strain. This value is always negative considering the range of the strain and the Poisson's ratio of the PDMS (0.45< ν <0.5) which is again consistent with the experimental observations plotted in Figure 2-21 suggesting that the relative resistance change in the y direction decreases in this region with increase in strain in the x direction.

2.6.2.2.2. PERCOLATIVE LIKE RESISTIVE BEHAVIOR REGION (REGION 2)

2.6.2.2.2.1. SLOPE AND THE TREND OF THE RESISITVE RESPONSE

In the second region where rGO's resistivity changes l_ε, w_ε and $t_\varepsilon$can be calculated by equations (2-3), (2-4), (2-5). Resistance in the perpendicular direction can then be calculated by equation (2-19) by replacing the length by the width and the width by the length in equation (1-22).

$$R_y = \rho_{Bulk}\left(\frac{t_{min}-t_c}{t-t_c}\right)^n.\frac{w}{l.t} \qquad (2\text{-}19)$$

Substituting l_ε, w_ε and t_ε in *l*, *w,* and *t*, equation (2-20) can be obtained.

$$R_y = \rho_{Bulk}(\frac{t_{min}-t_c}{t_\varepsilon-t_c})^n * \frac{w_0(1-\nu*\varepsilon)}{l_0(1+\varepsilon).\frac{t_0}{(1+\varepsilon)(1-\nu*\varepsilon)}} \qquad (2\text{-}20)$$

Rearranging the equation (2-20), equation (2-21) can be obtained.

$$R_y = \rho_{Bulk}(\frac{t_{min}-t_c}{t_\varepsilon-t_c})^n * \frac{w_0(1-\nu*\varepsilon)^2}{l_0.t_0} \qquad (2\text{-}21)$$

Substituting $l_0,\ w_0$ and t_0 in $l_\varepsilon,\ w_\varepsilon$ and t_ε in equation (2-21), equation (2-22) can be obtained.

$$R_{y_0} = \rho_{Bulk}(\frac{t_{min}-t_c}{t_0-t_c})^n * \frac{w_0}{l_0.t_0} \qquad (2\text{-}22)$$

By factoring out the same terms exist in equations (2-21) and (2-22), equations (2-23) and (2-24) can be obtained.

$$R_y = \frac{w_0}{l_0.t_0}\rho_{Bulk}(t_{min}-t_c)^n\left[(\frac{1}{t_\varepsilon-t_c})^n * \frac{(1-\nu*\varepsilon)^2}{1}\right] \qquad (2\text{-}23)$$

$$R_{y_0} = \frac{w_0}{l_0.t_0}\rho_{Bulk}(t_{min}-t_c)^n\left[(\frac{1}{t_0-t_c})^n\right] \qquad (2\text{-}24)$$

Difference between R_y and R_{y_0} can then be calculated by equation (2-25).

$$R_y - R_{y_0} = \frac{w_0}{l_0.t_0}\rho_{Bulk}(t_{min}-t_c)^n\left[\left(\frac{1}{t_\varepsilon-t_c}\right)^n.(1-\nu.\varepsilon)^2 - (\frac{1}{t_0-t_c})^n\right] \qquad (2\text{-}25)$$

Relative resistance change can then be calculated by equation (2-26).

$$\frac{\Delta R}{R_{y_0}} = \frac{R_y-R_{y_0}}{R_{y_0}} = \frac{\frac{w_0}{l_0.t_0}\rho_{Bulk}(t_{min}-t_c)^n\left[\left(\frac{1}{t_\varepsilon-t_c}\right)^n.(1-\nu*\varepsilon)^2-(\frac{1}{t_0-t_c})^n\right]}{\rho_{Bulk}(\frac{t_{min}-t_c}{t_0-t_c})^n*\frac{w_0}{l_0.t_0}} \qquad (2\text{-}26)$$

By rearranging the equation (2-26), equation (2-27) can be obtained.

$$\frac{\Delta R}{R_{y_0}} = \frac{\left[\left(\frac{1}{t_\varepsilon-t_c}\right)^n.(1-\nu*\varepsilon)^2-(\frac{1}{t_0-t_c})^n\right]}{(\frac{1}{t_0-t_c})^n} \qquad (2\text{-}27)$$

With factoring out and rearranging, relative resistance change in the second region can be obtained by equation (2-28)

$$\frac{\Delta R}{R_{y_0}} = (1-\nu.\varepsilon)^2.\left(\frac{t_0-t_c}{t_\varepsilon-t_c}\right)^n - 1 \qquad (2\text{-}28)$$

According to equation (2-14), with increase in strain in the direction aligned with the direction of applied tension, average thickness of the rGO film decreases.

Using equation (2-5) and substituting it in equation (2-28), equation (2-29) can be obtained:

$$\frac{\Delta R}{R_{y_0}} = (1 - \nu * \varepsilon)^2 . \left(\frac{t_0 - t_c}{\frac{t_0}{(1+\varepsilon)(1-\nu*\varepsilon)} - t_c} \right)^n - 1 \qquad (2\text{-}29)$$

By arranging, equation (2-30) can be obtained.

$$\frac{\Delta R}{R_{y_0}} = (1 - \nu * \varepsilon)^2 . [(1+\varepsilon)(1-\nu.\varepsilon)]^n . \left(\frac{t_0 - t_c}{\frac{t_0 - t_c(1+\varepsilon)(1-\nu*\varepsilon)}{1}} \right)^n - 1 \qquad (2\text{-}30)$$

With factoring out and rearranging, relative resistance change in the second region in the y direction can be obtained by equation (2-31).

$$\frac{\Delta R}{R_{y_0}} = (1+\varepsilon)^n (1-\nu.\varepsilon)^{n+2} . \left(\frac{t_0 - t_c}{t_0 - t_c(1+\varepsilon)(1-\nu*\varepsilon)} \right)^n - 1 \qquad (2\text{-}31)$$

2.6.2.2.2.2. THE MAGNITUDE OF THE RESISITVE RESPONSE

The reason why in this region (percolative like behavior region), the magnitude of relative resistance change in the perpendicular direction (equation (2-28)) is less than the magnitude in the aligned direction (equation (2-13)) can be explained by showing that $(1+\varepsilon)^2 > (1-\nu.\varepsilon)^2$ as follow:

Considering $\varepsilon > -\nu.\varepsilon$, by adding 1 to both sides of the inequality, it can be shown that $(1+\varepsilon)$ is greater than $(1-\nu.\varepsilon)$. Therefore, $(1+\varepsilon)^2$ is greater than $(1-\nu.\varepsilon)^2$.

Therefore, the relative resistance change in the x direction is larger in magnitude compared to the y direction.

2.6.2.3. Resistive response of the rGO in the direction at an angle with respect to the direction of applied tension

Relative resistance change in the direction that was at an angle (d direction) with respect to the direction of the applied tension generally followed that of aligned direction in all the samples. In the same 12 samples that survived 20.72% strain and their resistive response were linear-nonlinear with increasing trend in the x direction, the similar pattern was observed in the d direction (Figure 2-22). Furthermore, the same 3 samples that showed completely linear behavior in the x direction with an increasing trend showed the similar behavior in the d direction (Figure 2-23(a)). Figure 2-23(b) shows the resistive response at the angle, of the 4 samples that showed electrical failure in the x direction.

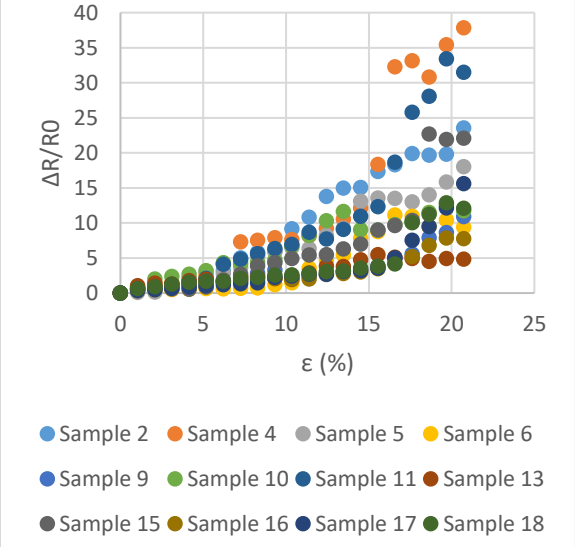

FIGURE 2-22. RESISTIVE RESPONSE OF THE 12 SAMPLES IN THE OBLIQUE DIRECTION WITH LINEAR-NONLINEAR AND INCREASING TREND

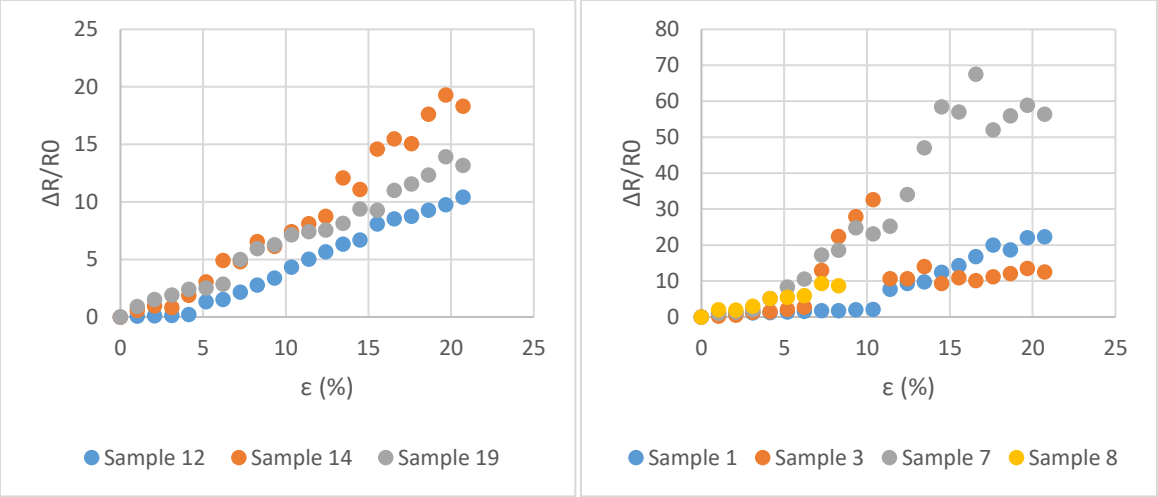

FIGURE 2-23. RESISTIVE RESPONSE (A) OF THE 3 SAMPLES IN THE OBLIQUE DIRECTION WITH COMPLETELY LINEAR AND INCREASING TREND THROUGHOUT THE EXPERIMENT (B) AT THE ANGLE, OF THE 4 SAMPLES THAT SHOWED ELECTRICAL FAILURE IN THE X DIRECTION

These similar patterns can show that, in the oblique direction, the resistive response is mostly affected by the effects of the resistive response in the x direction rather than those of the y direction.

However, the magnitude of the changes is reduced in the oblique directi on in comparison with the x direction which can be due to the cancellation of only a small part of the effects in the x-direction by the effects of the resistive response in the y-direction.

To investigate why the resistive response in the oblique direction follows mostly the resistive response of the sensor in the x direction, a mathematical model can be suggested. From mechanics of materials, the transformation of an strain in the rotated element can be mathematically described by equation (2-32) where λ, ε_λ, ε_x, ε_y and γ_{xy} are the angle of the rotated element with respect to the positive side of the x axis, normal strains in the λ, x and y directions, and shear strain in the xy plane respectively. Since the specimen is under a uniaxial tension, the shear strain in the original element can be set to zero and if a fictitious line is drawn

between the electrode O and B, the angle of that line with respect to the positive side of the x-axis can be measured as $\lambda = 45^{\circ}$.

$$\varepsilon_{\lambda} = \varepsilon_x \cos^2\lambda + \varepsilon_y \sin^2\lambda + \gamma_{xy}.\sin\lambda.\cos\lambda \qquad (2\text{-}32)$$

Therefore, strain in the rotated element at the $\lambda = 45^{\circ}$ can be calculated using equation (2-33)

$$\varepsilon_{45^{\circ}} = \frac{1}{2}(\varepsilon_x + \varepsilon_y) \qquad (2\text{-}33)$$

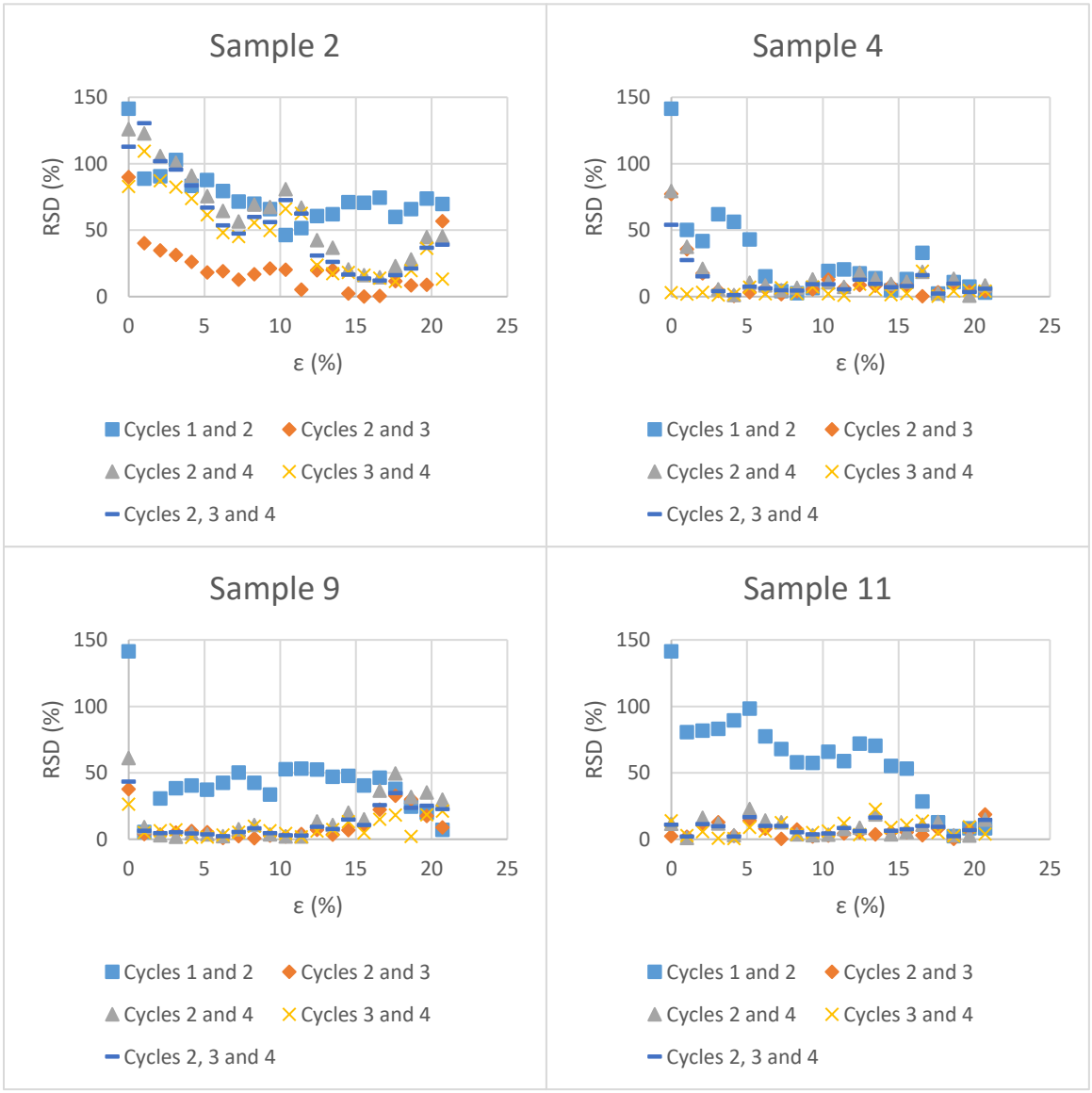

FIGURE 2-24. RSD BETWEEN CYCLES IN SAMPLES 2,4, 9 AND 11

It was shown previously that the absolute value of strain in the x direction is significantly greater than that in the y direction. This shows that only a small fraction of the resistive response of the sensor in the x direction can be canceled by that in the y direction which matches the experimental results. In other words, ε_x is a greater value compared to the absolute value of ε_y. Therefore, its effects on the oblique direction are greater too.

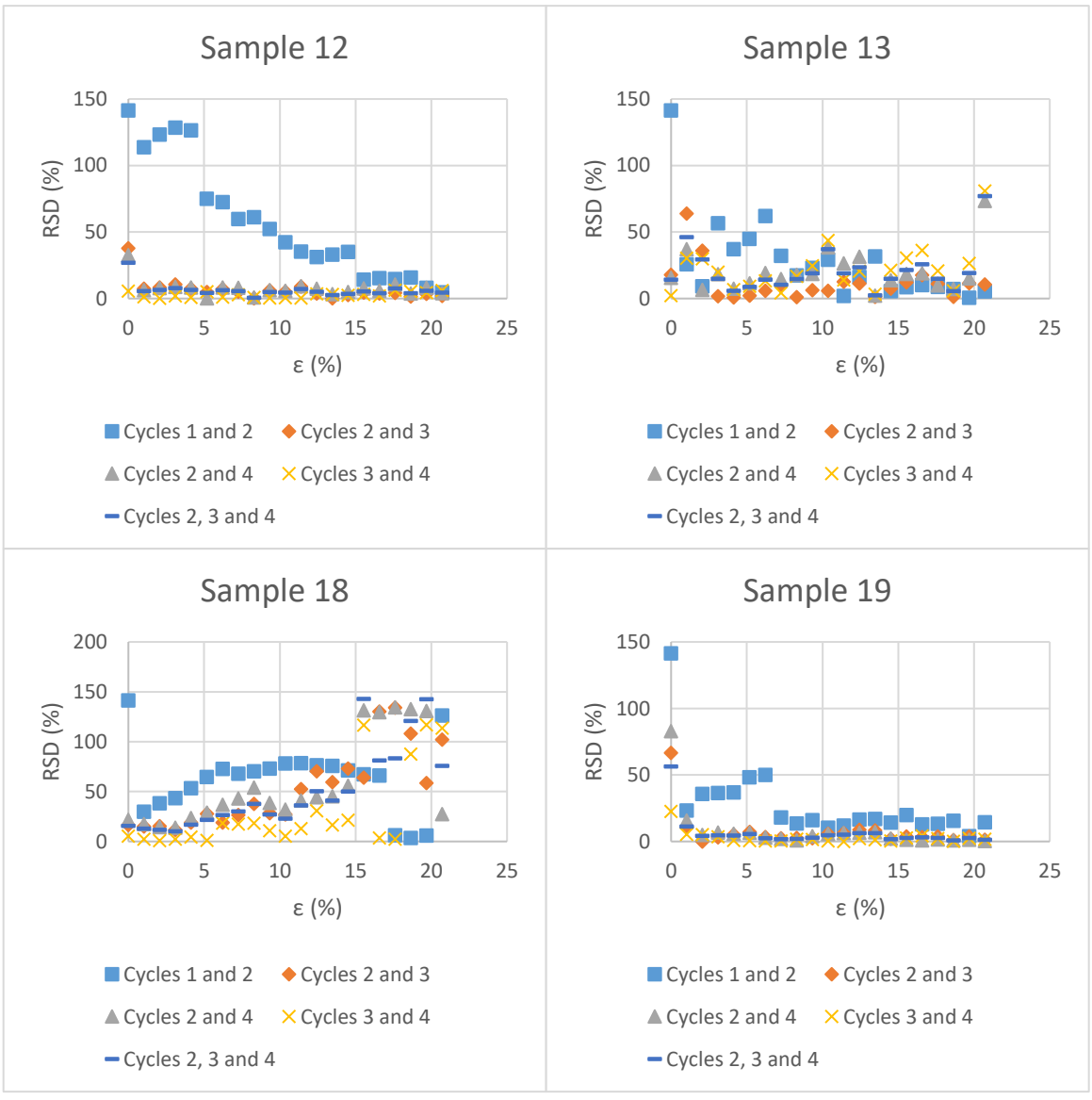

FIGURE 2-25. RSD BETWEEN CYCLES IN SAMPLES 12, 13, 18 AND 19

2.6.2.4. Resistive response under cyclic loading

In Figure 2-24 and Figure 2-25 relative standard deviation (RSD) of the resistive response of the rGO sensor in the x-direction between cycles are demonstrated in samples 2, 4, 9, 11, 12, 13, 18, 19 which were randomly selected. As can be seen in most cases, RSD calculated between cycles 1 and 2 is greater than between cycles 2 and 3, 2and 4, 3 and 4, as well as 2, 3 and 4. This difference suggests a variation in the resistive response of the samples occurring between the resistive responses of cycles 1 and 2 compared to those between cycles 2 and 3, 2and 4, 3 and 4, as well as 2, 3 and 4. In most cases, the variations in the resistive response that were observed between other cycles were smaller.

This variation in the resistive response can be attributed to the formation of residual microcracks during the first cycle which will be discussed later in the imaging section.

2.6.3. Imaging under strain

2.6.3.1. Camera

2.6.3.1.1. MOVEMENT AND SHIFTING OF THE RGO FLAKES UNDER TENSION.

Figure 2-26 shows a sample being stretched (in the x direction) and the rGO geometry was captured by the camera at each increment at 0%, 1.51%, 4.54%, 7.57%, 10.59%, 13.62%, 16.65% and 19.68%. As can be seen the number of cracks increased by increase in tension creating disconnections between electrical paths in the direction aligned with the direction of applied tension. These increasing disconnections are the reasons why the relative resistance change

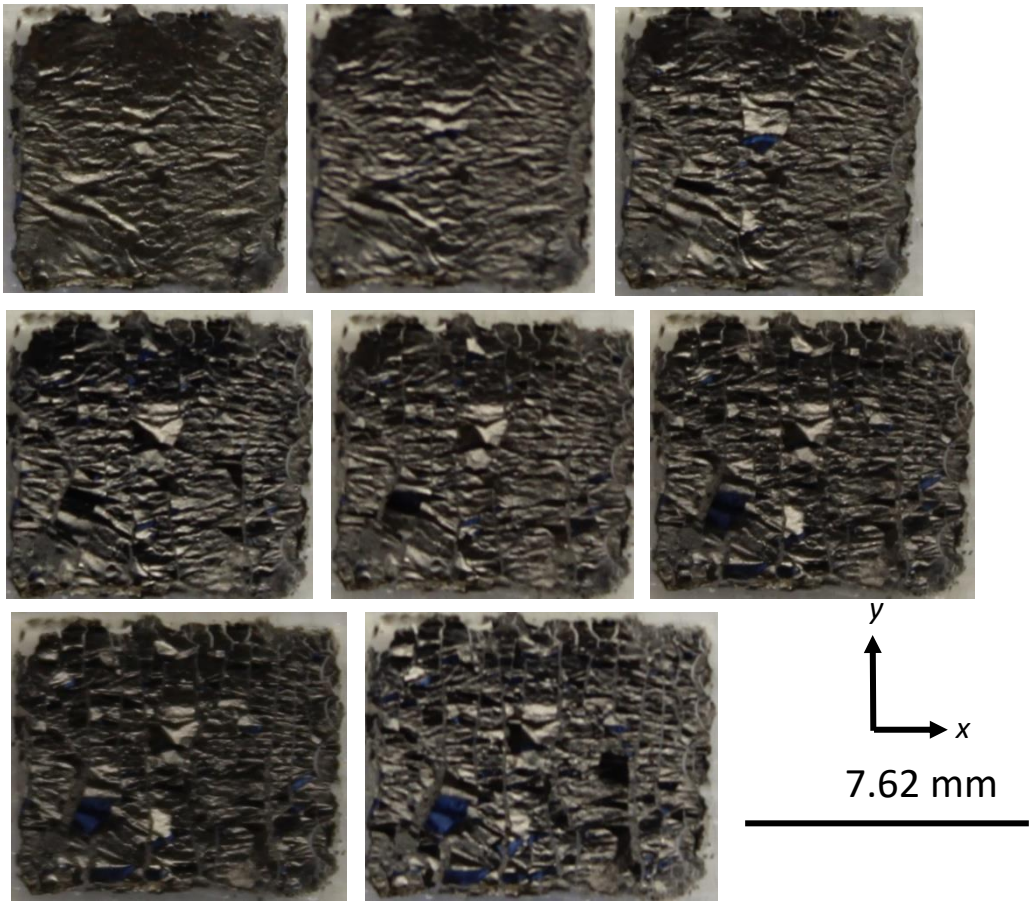

FIGURE 2-26. PICTURES OF THE RGO UNDER TENSION AT 0% , 1.51%, 4.54%, 7.57%, 10.59%, 13.62%, 16.65% AND 19.68% FROM THE TOP LEFT TO THE BOTTOM RIGHT OF THE PICTURE

increases in the x direction by increase in the applied tension which previously was explained in Figure 2-18, Figure 2-19, and Figure 2-20.

2.6.3.1.2. Crack closure after the sample being released.

The surface profile of the rGO film after each step of releasing from the applied tension at each increment looked the same in the macroscale, as it is shown in Figure 2-27. In the macroscale, the profile of the surface showed that the cracks were closed after releasing the sample under tension at each increment. However, the changes in the profile of the rGO will be discussed later using higher resolution images.

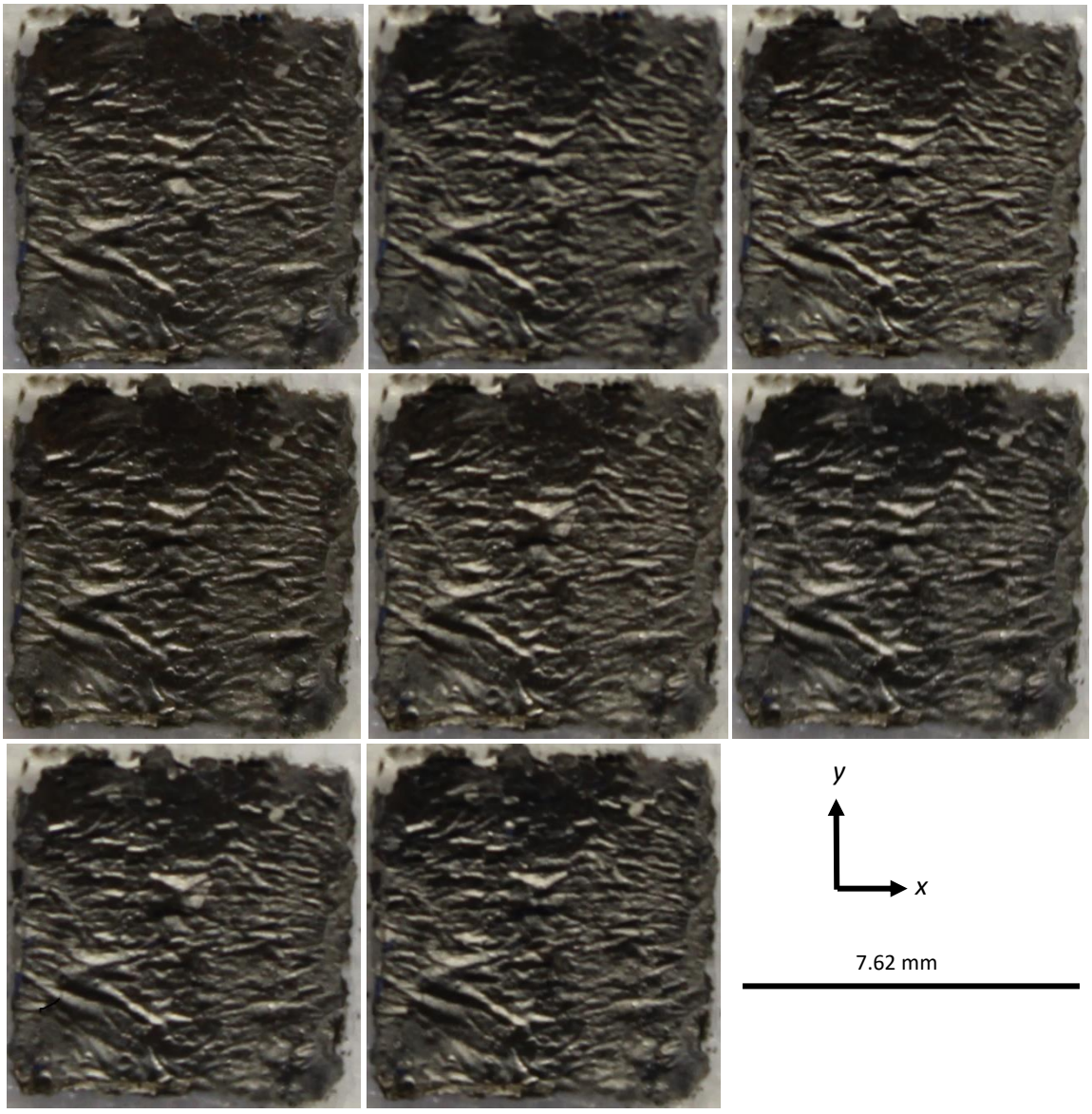

FIGURE 2-27. RGO SURFACE IMAGES AFTER RELEASING THE SAMPLE UNDER TENSION AT EACH INCREMENT

2.6.3.2. Confocal microscopic imaging

Results from confocal microscope imaging in Figure 2-28 show that there had been some pre-existed cracks in the surface of the rGO even prior to uniaxial tension application. After application of the tension (applied in the x direction), no significant brand-new crack was observed until 7.57% strain. Cracks started to form with the higher speed starting at 7.57% strain

which could correspond with the strain level at which the rGO sensor started to show nonlinear resistive response. The accumulated length of cracks started to increase with a higher rate beginning at 7.57% strain. This value was approximated using the scale bar and as 0 mm, 0 mm, and 1.64 mm were the accumulated length of cracks measured at 0%, 1.51% and 4.54% strains respectively. Suddenly this value increased significantly from 1.64 mm to 7.62 mm at 7.57% strain and continued to increase to 8.74mm at 10.59% strain. This could be attributed to the movement of the flakes of rGO over each other due to percolative like behavior resulting in accumulation of flakes in some areas leaving the adjacent areas empty (crack formation). Furthermore, as Figure 2-28 suggests, there are some cracks formed aligned with the direction of applied tension

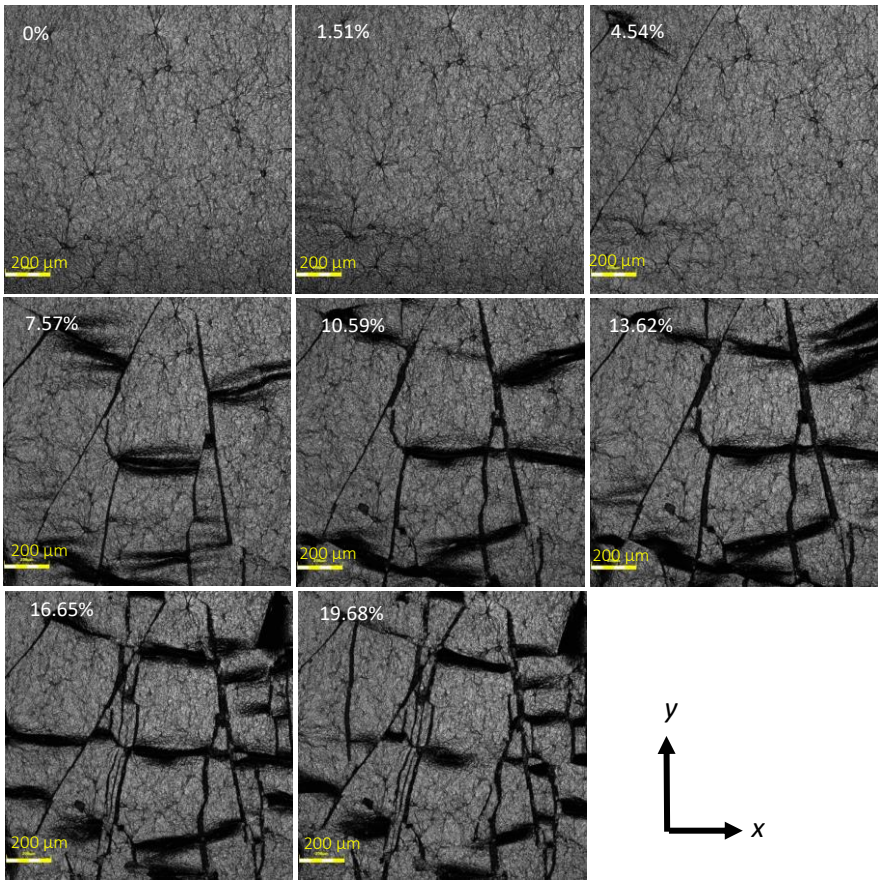

FIGURE 2-28. SLIDING AND SHIFTING OF THE RGO FLAKES AND CRACK FORMATION

creating local disconnections in the electrical paths in the y direction which was consistent with the partial increasing trends shown in Figure 2-21.

Figure 2-29 shows that there were residual microcracks that formed after the first cycle of tension (tension applied in the x direction). As can be seen, these microcracks are present for the rest of the cycles an became a part of the permanent profile of the rGO after the first cycle. This phenomenon can explain Figure 2-24 and Figure 2-25 that in most of the cases showed greater deviation in the relative standard deviations between cycles 1 and 2, versus between other cycles (i.e. cycles 2 and 3, 2 and 4, 3 and 4 and even 2, 3 and 4).

Figure 2-30 and Figure 2-31 demonstrate the change in the height difference between point 1 on the PDMS surface and point 2 on the rGO surface in sample 1 and 2 respectively. These measurements that were performed using the confocal microscope suggest that the elevation difference between the two points on the PDMS substrate and the rGO surface decreased with increase in strain in the x direction in both samples until 4.54% strain. However, at 7.57% strain and further the general trend of the height difference between the two points increased. This increase could be attributed to the

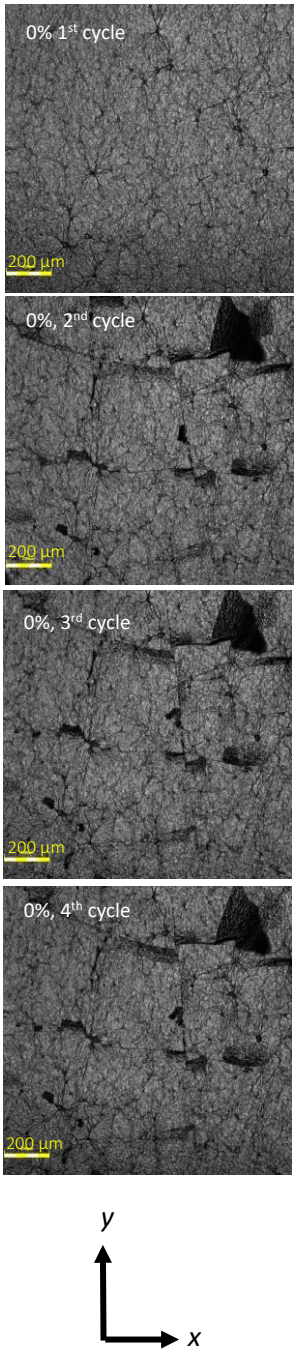

FIGURE 2-29. PERMANENT RESIDUAL CRACKS AFTER THE END OF FIRST CYCLE

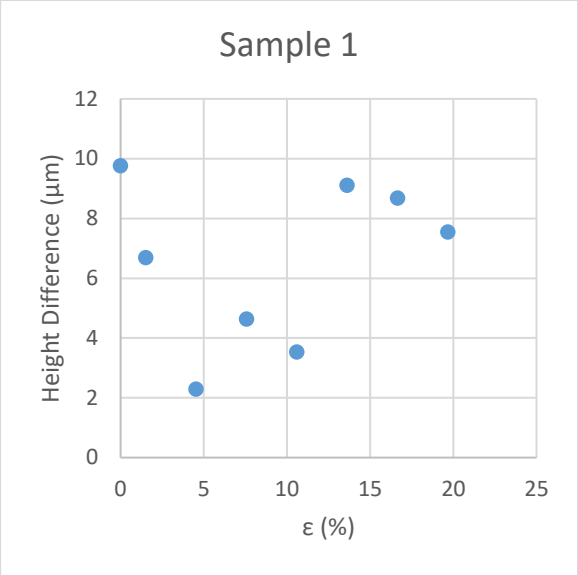

FIGURE 2-30. CHANGE IN HEIGHT DIFFERENCE BETWEEN POINT 1 ON THE PDMS SURFACE AND 2 ON THE RGO SURFACE IN SAMPLE 1

percolative behavior of the rGO film. In other words, this could be due to the accumulation of rGO flakes because of the interconnection between flakes leaving empty parts in the adjacent areas (crack formation).

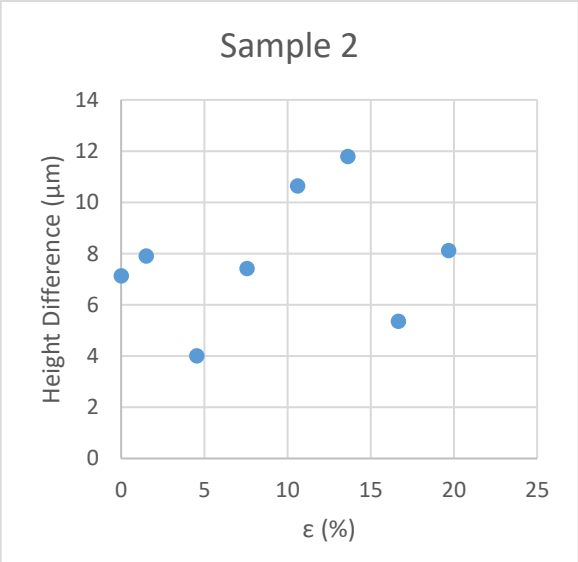

FIGURE 2-31. CHANGE IN HEIGHT DIFFERENCE BETWEEN POINT 1 ON THE PDMS SURFACE AND 2 ON THE RGO SURFACE IN SAMPLE2

2.6.3.3. Atomic force microscopic imaging

As it can be seen from Figure 2-32(a), and Figure 2-32(b), the topography of the rGO surface at 7.57% suggested a rougher surface than that at the 0% strain. This can be due to the movements of rGO flakes over each other under strain at 7.57% due to percolative behavior making the edges or tips of the flakes visible. This matches the results discussed in the confocal microscopic images (Figure 2-28) where the sample started to show higher rate of crack formation on the rGO surface starting at 7.57% strain suggesting movements of the flakes over each other representing a percolative behavior resulting in accumulation of flakes in some areas leaving the adjacent areas empty (crack formation).

Furthermore, measurements by the atomic force microscope showed that the maximum and minimum elevations at 0% strain were 1.6 nm and -1.5 nm. At 7.57% strain, the maximum and minimum elevations were measured as 2.4 nm and -1.4 nm. Therefore, the difference of elevations at 0% was 3.1 nm and at 7.57% was 3.8 nm. The greater value between elevations at

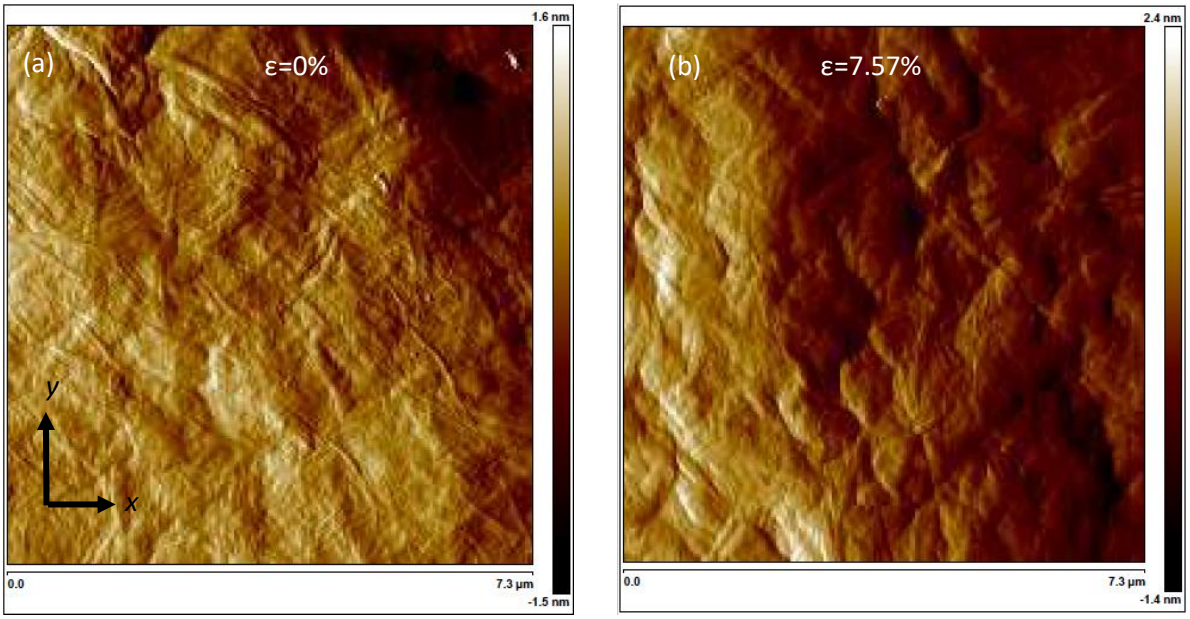

FIGURE 2-32. (A) ATOMIC FORCE MICROSCOPE AT 0% STRAIN. (B) ATOMIC FORCE MICROSCOPE AT 7.57% STRAIN

7.57% strain can be attributed to the accumulation of the flakes leaving the adjacent parts empty (crack formation) at this strain which could match the results from confocal microscope measurements shown in Figure 2-30 and Figure 2-31 too.

2.7. Summary of Experimental Investigation

Initial tests on the specimens tested under strains up to the electrical failure showed that rGO sensors with area densities of 0.0069 mg/mm^2, 0.0080 mg/mm^2, and 0.0091 mg/mm^2, electrically failed on average at 20.36%, 34.19% and 40.92% strains. It showed that as the area density increased, the average strain values of electrical failure increased too. On average, the increase in the area density of the GO deposited on the substrate increased the strain tolerance of the samples. Samples with greater area densities showed reduction in gauge factors. However, GF values were still high enough for the sensors to be considered as highly sensitive strain sensors compared to common foil strain gauges. Sensors in most cases showed linear-nonlinear resistive behavior with the increasing trend in the x direction while under strain in the x direction. The linear resistive behavior of the sensor under strain was consistent with that of bulk like materials. The nonlinear resistive behavior of the sensor under strain was aligned with that of percolative materials. The linear-nonlinear and increasing resistive behavior of the sensor matched the mathematical models. In the y direction, the resistive response of the sensor was decreasing. This behavior of the sensor could be due to contraction in the rGO in the direction perpendicular to the direction of applied tension caused by Poisson's effect in the PDMS substrate. This decreasing trend matched the mathematical model. Partial positive slopes observed in the resistive response of the sensor in the y direction could be attributed to the cracks that formed locally in the direction aligned with the direction of applied tension creating local disconnections in the

electrical paths in the y direction. At the angle, resistive response of the sensor was mostly affected by the resistive response of the sensor in the x direction rather than the y direction. This major influence matched the equations derived from the concept of the transformation of strains in the rotated elements. Furthermore, the rGO strain gauge showed the average gauge factor of 91.503 with a linear fit which was significantly greater than GF of metal foil strain gauges (about 2). 4-cycle cyclic testing results showed that in most cases, there were noticeable variations between the resistive response values between cycles 1 and 2. The variation decreased between the next cycles. According to the confocal microscope images, this phenomenon could be attributed to the formation of the residual microcracks after the first cycle causing deviation in the resistive response between cycles one and two. These residual microcracks remained in place for the rest of the cycles causing smaller resistive response deviations between other cycles after the first cycle. Confocal microscope images also revealed that the cracks formation rate increased starting at 7.57% strain and beyond which could be attributed to the movement of the flakes of rGO over each other due to percolative like behavior resulting in accumulation of flakes in some areas leaving the adjacent areas empty (crack formation). Measurements by the confocal microscope suggested an accumulation of the rGO flakes because of their interconnections starting at 7.57% strain further, leaving the adjacent areas empty (crack formation). The elevation differences observed in the atomic force microscopy images taken at 0% and 7.57% strains could be because of this accumulation of flakes as well.

3. APPLICATION OF THE STRAIN SENSOR IN LOW-COST LEAK DETECTION FOR HEALTH MONITORING OF WATER EQUIPMENT

3.1. Introduction

3.1.1. Potential Applications of The rGO Strain Sensor

Due to low-cost and easy mass production and high sensitivity of the rGO strain sensor, it can be employed for multiple applications especially in highly sensitive, low-cost applications that require mass production and internet of things. Here two potential applications are presented including highly sensitive and low-cost substitute for Rosette strain gauge configurations and highly sensitive leak detectors.

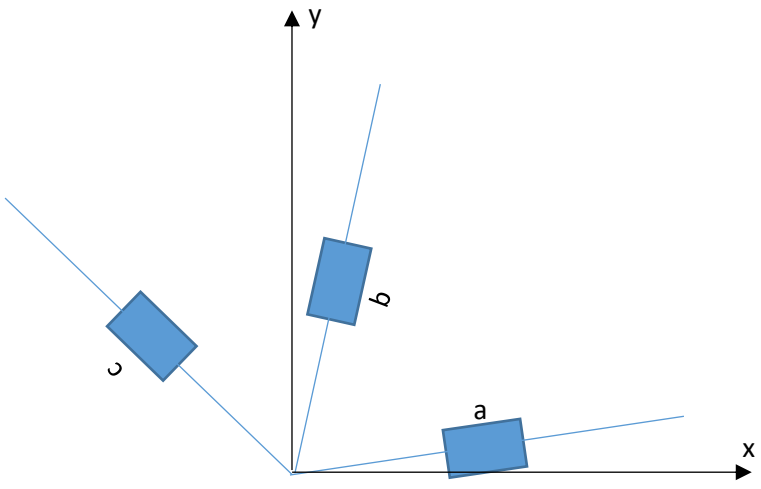

FIGURE 3-1. ROSETTE STRAIN SENSING CONFIGURATION

3.1.1.1. Rosette strain gauge

The rGO strain gauge can be used for applications where 3 in-plane components of strain tensor are to be measured like a Rosette strain measurement configuration (Figure 3-1). In Rosette arrangement, 3 separate strain gauges are required. However, using rGO strain gauge, only one patch of rGO strain sensor with 3 conductive paths would suffice to calculate 3 unknown strains in the plane strain state ε_{xx}, ε_{yy} and γ_{xy}. Plane strain is a state of strain in which out-of-plane strain components are equal to zero (thick plate theory) [2], [4]. 3 unknown strains in the plane strain state can be calculated by measurement of normal strains at a (ε_a), b (ε_b) and c (ε_c), with knowing the angles between axis x and the axis of strain gauges a (θ_a), b (θ_b) and c (θ_c). Three unknowns can be calculated using three sets of equation (3-1), equation (3-2) and equation (3-3) [2], [4].

$$\varepsilon_a = \varepsilon_{xx}\, cos^2\theta_a + \varepsilon_{yy} sin^2\theta_a + \gamma_{xy}.sin\theta_a.cos\theta_a \qquad (3\text{-}1)$$

$$\varepsilon_b = \varepsilon_{xx}\, cos^2\theta_b + \varepsilon_{yy} sin^2\theta_b + \gamma_{xy}.sin\theta_a.cos\theta_a \qquad (3\text{-}2)$$

$$\varepsilon_c = \varepsilon_{xx}\, cos^2\theta_c + \varepsilon_{yy} sin^2\theta_c + \gamma_{xy}.sin\theta_c.cos\theta_c \qquad (3\text{-}3)$$

Additionally, cost effectiveness can be another major benefit of using an rGO patch in this specific application. A single patch versus 3 separate strain gauges that can play a Rosette strain sensing role can be significantly less expensive than the current commercial ones especially when mass production is the target. In addition to being low-cost it can provide significantly higher sensitivity to strain compared to the commercial metallic rosette strain gauges as demonstrated by the high gauge factors observed.

3.1.1.2. Highly sensitive leak detector

Cost effectiveness of rGO strain sensors can be employed for applications where internet of things and mass production are necessary. Additionally, high sensitivity of a sensor can play a major role in applications like leak detection of water equipment. Therefore, detecting leaks with low-cost sensors that can be mass produced can be one of the applications that is well suited for rGO strain sensor. In this chapter the novel design of rGO strain-based sensor for leak detection and health monitoring of water equipment is discussed.

3.1.2. Motivation

Water resources are limited, and water treatment is a time consuming and expensive process. Hence, water preservation is important. In north America, 20% to 50% of water is wasted through leaks in the supply system [113]. Leak detection is an important measure to monitor the health of the water equipment to prevent waste of water or any further damage to them. There is a hole in the market for low-cost flow meters capable of measuring ultralow flow rates; a highly sensitive strain gauge-based flowmeter that can detect water leakage for instance.

3.1.3. Background

Water is a precious resource without which no one can live. Clean water resources are limited. According to the Centers for Disease Control and Prevention (CDC), more than 1/10 of the world's population do not have access to clean water[114]. Thus, this precious resource should be conserved and not wasted. According to United States Environmental Protection Agency (EPA) 900 billion gallons of water nationwide is being wasted due to leaks in households annually [115].

3.1.3.1. Importance of water leak detection

- To prevent pressure-drop in the water distribution systems and consequently energy loss prevention, water leak detection is critical. Water leaks can cause significant pressure drop in water distribution networks that needs to be compensated by consuming more energy to create the same amount of pressure in the system [116].
- To support environmental sustainability by preventing loss of energy that has been consumed to produce clean water. A significant amount of energy has been consumed to treat and produce a single drop of clean water. Therefore, wasting clean water equals wasting significant amount of energy used to produce it [117]
- To prevent water contamination in the pipelines and consequent health issues. Water distribution networks are usually underground systems surrounded by soil that contain contaminants and microorganisms that can be threatening to human health. Even a small leak in the pipes can contribute to the penetration of that contaminants to the water systems due to possible negative pressure occurring in the system [118] causing potential infectious diseases[116]. Furthermore, non-potable water can flow into the drinking water due to leakage of the pipes[117], [119], [120] Early leak detection can help preventing introduction of contaminants into to the clean water systems from the surrounding environment.

3.1.3.2. Importance of inline water leak monitoring

- Because the majority of water distribution networks are underground and require time and energy to be reached, inline leak detection is a faster and more energy and cost efficient to locate the leak. [116]
- Inline leak detection can be employed for real time monitoring unlike common methods that need shutting down the system and time for diagnosis phase.

3.1.3.3. Causes of pipe leakage

- According to EPA most of the United States' water distribution systems were constructed more than 50 years ago which makes them prone to deterioration and consequently leak [119].
- Fluctuation in water pressure can cause leaks in the pipes.
- Inadequate maintenance can contribute to pipe leakage.
- Harsh service environment can cause issues like corrosion. Corrosion usually occurs when the water pipe is made of metal and is surrounded by reactive substances or chemicals in the soil [117], [121]

3.1.3.4. Leak detection methods

Leak detection can be defined as 3 major phases. Identifying the leak which is the investigation of whether the sensed stimuli initiated by a leak or other potential factors like signals from a pump. The second major factor is localizing which is determination of the

proximity of the part of the water system that is suspected to be damaged and leaking, The last phase is locating the leak [122].

3.1.3.5. Methods of leak detection

- **Acoustic leak detection**: Acoustic principles have widely been used to detect the leak. One of the first experiments with under water acoustics was performed by Leonardo Da Vinci in 1490 and became important during WWI to detect the presence or distance of submarines. Acoustic leak detection can be performed by characterization of the leakage sound in the pipe. locating a leakage point in the pipe can be a hard task due to many sounds present in the pipe [123]–[126]. Ultrasonic leak detection focuses on detection of specific frequencies caused by the leak. [127], [128]
- **Gas Injection Method**: in this method helium or more commonly hydrogen is injected into the pipe as the tracer gas. The location of the leak can be detected once the gas escapes from the leaking area and appears on the surface. Drawback of the Gas Injection Method is that the water in the pipe should sometimes be partially or completely evacuated. Sometimes the pipeline branches should be shut off which cause a downtime [129]. This method also needs trained personnel and specialized equipment to be performed.
- **Manually listening stick:** in this method the leakage presence can be detected using an earpiece. It is commonly used for pipes with pressure higher than 10 m. The accuracy of this method is highly dependent on the ability of the engineer listening to the signals and the interfering noises created by the materials under the surface of the ground [129]. This method also needs trained personnel and specialized equipment to be performed.

- **Leak noise correlation:** in this method two noise detection are located far from each other. If a leakage occurs, the distance between the leakage location from each sensor is calculated by measuring travel time of the created noise by the leakage considering the pipe material and size. Any source of noise can cause large errors. In plastic pipes, this method shows less accuracy if accelerometer is used as the noise transducer [129]. This method also needs trained personnel and specialized equipment to be performed.
- **Inline leak detection methods:** tethered and free-swimming systems are both well suited for large pipelines where the sensor is inserted into the flow and moves with the flow to arrive at the point of leakage. In both methods pipe tapping is usually required to insert the sensor. Tapping of the pipe usually is associated by a downtime of the part or the whole system.[129].
- **Thermal imaging:** is another approach to detect leaks by thermal infrared images that show the infrared energy of the target pipe. It can be categorized in different levels of surveys. usually interpretation based on the raw data is subjective and a skilled interpretation needed in this method especially in higher level surveys[129]. In this method weather, humidity and environmental conditions can drastically affect the results and undermine the precision of the method [130]
- **Ground penetrating radar:** In this method a low frequency electromagnetic wave is sent underground and sense the reflected signal and creates an image of the underground structure. This method is very time consuming for leak detection and yet the vicinity of the leakage should be apparent for this method to be employed. [131]–[133]

- **Electromagnetic wave sensor:** In this study high frequency electromagnetic waves can be propagated and sensed inside the pipe. Leak can be located by searching for frequency and amplitude changes in the sensed signal [133]. The drawback of this method is that it can only be used in large size metal pipes (100 mm).
- **Flow and pressure monitoring:**
    - One of the main approaches to detect leaks is to constantly monitor the pressure and flow of the pipe. Once a leakage occurs, the flow and pressure change in the pipe. This difference in hydraulic characteristics of the flow can interpreted to the presence of a leak in the system followed by an alarm to notify operator or maintenance personnel in charge to early detect the leakage and repaire it [117]
    - Flow patterns can be monitored to detect a leak. Sudden or abnormal deviation from the normal pattern can be interpreted to the presence of leakage. This method can only be useful for prioritizing the zones in the water network that potentially need more investigation using more reliable methods [134]
    - In steady or a transient flow, a mathematical models can be developed such as Least Squares Minimization [135] or Inverse Transient Analysis [136] to predict the leakage. However this methods can only detect leaks at the nodal points of the model yet requires a significant amount of data to be collected [134]. In a steady flow the condition and properties (e.g. flowrate and pressure) of the system is constant over time whereas in a transient flow in which they change over time [137], [138].

3.1.3.6. Flowrate definition

Flow rate can be defined as the volume of liquid passing through a certain cross section area in a unit of time. It can be formulated as Equation (3-4)

$$Flowrate = \frac{Volume\ of\ the\ liquid}{elappsed\ time} \qquad (3\text{-}4)$$

The unit for flowrate in SI system is cubic meter per second [139]–[141].

3.1.3.7. Flow rate measurement techniques

Flow rate can be measured using either the mass of the liquid over time or the volume of the liquid over time. For this study water was considered incompressible. Many techniques have been developed over the past century to measure flowrate like thermal flow measurement, turbine flow metering, variable area, positive displacement, oscillatory flow metering etc. Some of the common ones are explained below.

3.1.3.7.1. CORIOLIS FLOW METERS

This is a type of mass flow measurement technique based on the angular momentum of the vibrating tube caused by the liquid flowing through the tube. As the flowrate increases the force increases. Therefore, a larger angular momentum would be created. This method of flow metering is expensive and associated with some limitations such as the material that is used and the size of the pipe [96], [142]–[147]

3.1.3.7.2. ELECTROMAGNETIC FLOW MEASUREMENT

The science behind this technique of flow metering is that electrical current can be generated by applying a magnetic field which was discovered by Michael Faraday in 1831. In this method the particles of the conductive liquid like water can be electrically charged by the magnetic field applied by two coils across the pipe and electrical voltage difference can be measured with two installed electrodes. When the liquid begins to flow, the electrically charged particles become attracted to the opposite electrodes and the voltage difference is created. As the flow increases the number of electrically charged particles increases, contributing to the greater voltage difference across the pipe. This method can only be used for liquids that are reasonably conductive. Other disadvantages of this type of flow metering is its relatively complicated installation and its high cost [96], [142]–[148].

3.1.3.7.3. DIFFERENTIAL PRESSURE FLOWMETERS

This common type of flowmeter is composed of a restriction element like an orifice plate which is responsible for creating a pressure drop that can be translated to flowrate values. This type of technology is based on Bernoulli's equation and the continuity in pipes. As Bernoulli's equation

states, in a pipe as the cross-section through which the liquid flows changes, the sum of kinetic, static and potential is nominally conserved. This equation can be formulated as the Equation (3-5).

$$Elevation\ of\ the\ pipe + \frac{pressure}{(density).(gravitational\ acceleration)} + \frac{(velocity)^2}{2.(gravitational\ acceleration)} = constant\ value \quad (3\text{-}5)$$

The continuity equation in pipes can be expressed as the constant value resulting from the multiplication of the velocity of a incompressible liquid like water by the cross sectional area through which it flows. This method of flow metering can be accurate. However it creates pressure drop in the pipe which is not desirable [96], [142]–[149]

3.1.3.7.4. ULTRASONIC FLOWMETERS

This flow measurement technique is based on calculating the flow velocity of the liquid by measurement of the time taken by the signals in the relevant liquid to travel in the direction of the flow and against it. There are different ways to use this technique. One of the common ones is to use several piezoelectric crystals to transmit and receive ultrasound signals into and against the flow. Piezoelectrics can create voltage potential when receive an ultrasonic signal and conversely can create ultrasonic signal when applying a voltage. [96], [142]–[148], [150], [151]

3.1.3.7.5. TARGET FLOWMETERS

Target flow metering is based on the measurement of the flowrate based on the measurement of the force exerted on the object (target) in the water. The force exerted on the target in the water can be calculated from the difference of the pressure in the front and back of the target's area. The force then can be linearly translated to the flowrate. The force proportionality depends on whether the flow is laminar or turbulent. In the turbulent flow the force is proportional with the square of velocity and therefore the square of flow rate. in the laminar flow however, the force is proportional with the velocity and the viscosity of the liquid. The flowmeter in this technique is prone to wear and tear [96], [142]–[148], [152].

3.2. Challenges

Many of the present or previously used leak detection technologies including acoustic detection [153], [154], Fiber Optic Sensing [155], [156], Infrared Radiometric method [157], [158], electromagnetic flow meters etc. can be associated with some challenges. Firstly, they can be labor-intensive, which makes them unsuitable unless necessary. Additionally, they can be very expensive to be mass produced (>$300), very time consuming to be completed, require down-time for maintenance or installation to be operated, subjective and dependent on how good the result interpreter is trained or skilled. In addition, certain techniques may compromise the accuracy or precision of the outcomes, or may lack a range of customizable options suitable for different pipe sizes and materials. [122], [129]–[132], [144], [145], [159].

3.3. Objective

Creation of low-cost leak detection mechanism that is suitable for health monitoring of water equipment.

3.4. Approach

Leak detection by ultra-low flow measurement by taking advantage of high sensitivity of the rGO-based strain gauge. Additionally, to keep the cost down the following approaches were considered.

1. rGO was used due to its potential for low-cost mass production.
2. The leak detector was designed in a fashion that no hinges or moving parts involved. Therefore, low costs of maintenance were another major cost effectiveness of the device.
3. Knowledge about leak was prioritized over high accuracy and precision of the sensor.

3.5. Major Tasks

3.5.1. Sensor Principle of Working

The sensor principle of working is a combination of momentum target metering and differential pressure flow measurement techniques. The rGO was used at the center of the body of the flowmeter as the direct sensing element. Once the flow reaches the flowmeter, the body of the flowmeter bends creating stress (and strain) which can be sensed and picked up by the rGO strain sensor through change in resistance as the rection of the sensor to the stimulus. The design benefits from a novel symmetrical design, with two flaps which can bend out of the way to avoid

creation of a high pressure drop. Flowmeter was also composed a supporting middle beam as the substrate of the rGO film.

3.5.2. Materials and Synthesis

The sensor body was made of PDMS and rGO was used as the sensing element. 186 Silicone Elastomer (PDMS) was used to make the body of the sensor. First the PDMS was cast into the molds. To remove the bubbles from the PDMS, it was placed in a vacuum chamber for 80 min first and then cast into molds. Molds were designed by Creo CAD software, prototyped by a MakerBot replicator+ 3D printer [160] first and after the dimensions, sizes and design were established, the final mold's designs were sent to the University of Wisconsin Milwaukee's Machine Shop to be machined for quality improvement of the resulting specimens. Polycarbonate material was used to create the molds. After the SYLGARD 186 Silicone Elastomer was cast into the molds, it was cured at room temperature for 3 days. Figure 3-2 shows the simulation of the final body of the sensor. After the cured body of the sensor was cut out of the mold, it was washed completely by deionized water and dried by compressed air. To enhance the adhesion of the substrate it was placed in a PE-25 plasma etching machine for 5 minutes. Then it

FIGURE 3-2. BODY OF LEAK DETECTION SENSOR

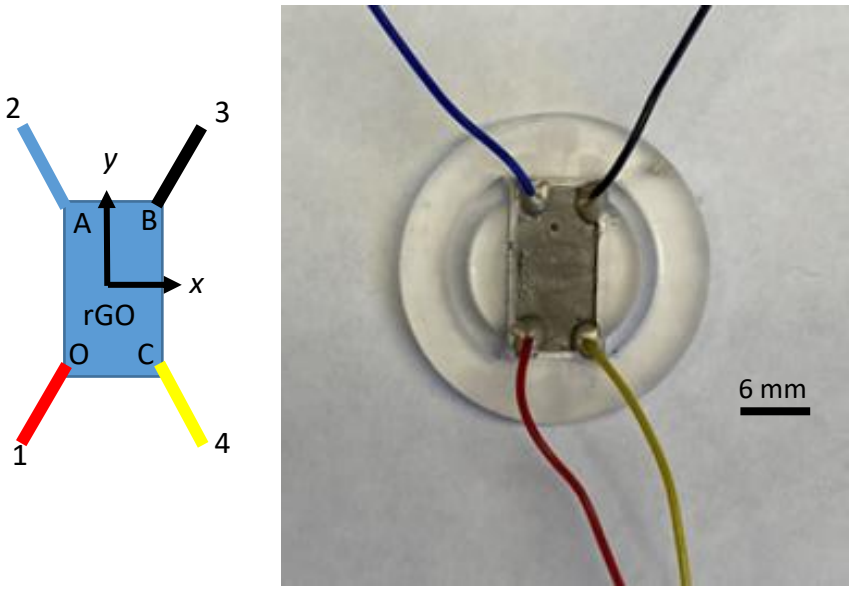

FIGURE 3-3. THE SENSOR AFTER ADDING ELECTRODES

was immersed in a solution of 2 part (3-Aminopropyl)triethoxysilane and 98 parts Ethanol for 3 hours. To prepare the GO (Graphenea 0.4 wt% GO dispersion in water) solution for drop casting, it was agitated in a Cole Parmer ultrasonic cleaner (M-series) for 2 minutes. Graphenea graphene oxide dispersion was characterized in section 2.5.2.3. before. Then 0.1282 ml of the solution was drop cast on to the reservoir of the body of the sensor with the area of 6.096 mm by 12.192 mm to make 0.0069 mg/mm^2 area density of GO on the body of the sensor. Then it was kept in the hood at room temperature to be dried for 24 hours. After being dried, thermal reduction was performed on the Sensor. It was placed in the OTF-1200 Series Split Tube Furnaces in the presence of Argon gas. In the thermal reduction process, temperature was raised to 180˚c from room temperature in 60 min and kept at the same temperature in 60 min. Again, increased to 200˚c in 5 min and kept at the same temperature for 10 min. Finally brought back to the room temperature in 90 min. The temperature was ramped up and down to reach the targeted temperature. This overall processing was developed with the assistance and testing of Li-Chih

Tsai and Maysam Rezaee and their work is presented in Tsai et al 2019 [51], Rezaee 2021 [104], Rezaee et al 2019 [50] and Rezaee et al 2021 [52].

After the thermal reduction process, 4 electrodes (copper wires) were added by the conductive epoxy to the sensor like Figure 3-3 [95], [96]. After adding the electrodes and allowing the conductive epoxy to cure a layer of PDMS was deposited on the rGO patch, the tips of the electrodes on the rGO patch and the conductive epoxy to prevent their contact with water. To measure resistance the same circuit and equation as for the tensile tests were used. Sensor was designed to be used for a 12.7 mm (½ inch) diameter pipe. An air void was designed inside the sensor later during the research for pressure sensing which was not visible from the outside.

3.5.3. Factorial Analysis

A factorial analysis was performed on the body of the flowmeter to investigate some potential parameters of the design with significant effects on the response of the sensor. The parameters that were included in the analysis were thickness of the flaps of the design, thickness of the supporting middle beam of the design (on which the rGO patch is located), width of the supporting middle beam, and flowrate. The sslast factor was whether using a ring made of PDMS on the upstream side next to the sensor to improve the sensitivity of the sensor or not. Factorial analysis was performed with the significance level of 0.5. The factorial analysis was performed in the early stages of the improvement process of the design and some of the dimensions and sizes have been improved ever since.

For design of the experiment, intended values were assigned to the factors. Two levels of 0.001016m and 0.001524m were assigned to the flap thickness, two levels of 0.001651m and

0.002159m to supporting middle beam thickness, two levels of 0.00254m and 0.00508m to middle beam width two levels of 90 ml/min and 150 ml/min to flowrate and finally for backing ring presence two level of “yes” and “no” were assigned. In total, combination of 32 experiments were designed and performed.

3.5.4. Finite Element modeling

Finite element analysis was performed in the x and y directions to determine the best geometry of the rGO patch to improve the sensitivity of the sensor.

3.5.5. Flow meter resistive response testing

Flowrates were varied to investigate the resistive response of the sensor. The test was performed at 137.895 kPa (20 psi) pressure. The sensor was placed in a coupling between two pipes with 12.7 mm (1/2 inch) diameters. The distance between electrodes on the sensor in x, y and at the angle directions were 0.61 mm, 6.37 mm, and 7.16 mm. In addition, the sensitivity and resolution of the sensor were measured. Pressure regulator and pressure gauges were used to reduce and measure the pressure (20 psi) respectively. Arduino Uno was used to supply excitation electrical energy for the data acquisition circuit (Figure 3-4).

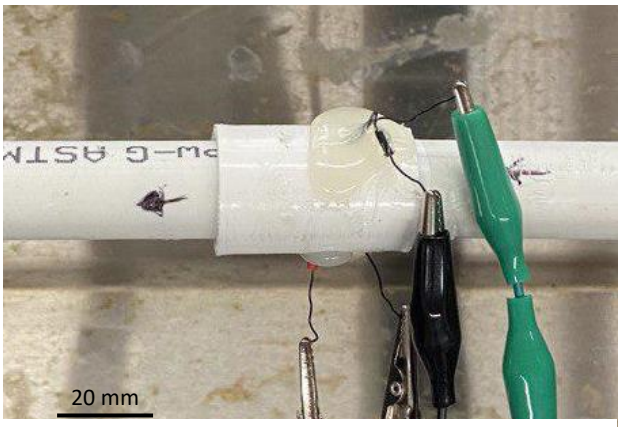

FIGURE 3-4. SENSOR WAS PLACED IN A COUPLING BETWEEN PIPES WITH 12.7 MM IN DIAMETER

3.5.6. Pressure-drop caused by the sensor.

Pressure drop was evaluated on the initial design in the sensor to determine the amount of pressure drop that happened when the sensor was in the pipe. It was tested in a 45.72 cm long pipe. The sensor was placed in a coupling between two pipes with 12.7 mm (1/2 inch) diameters as shown in Figure 3-5.

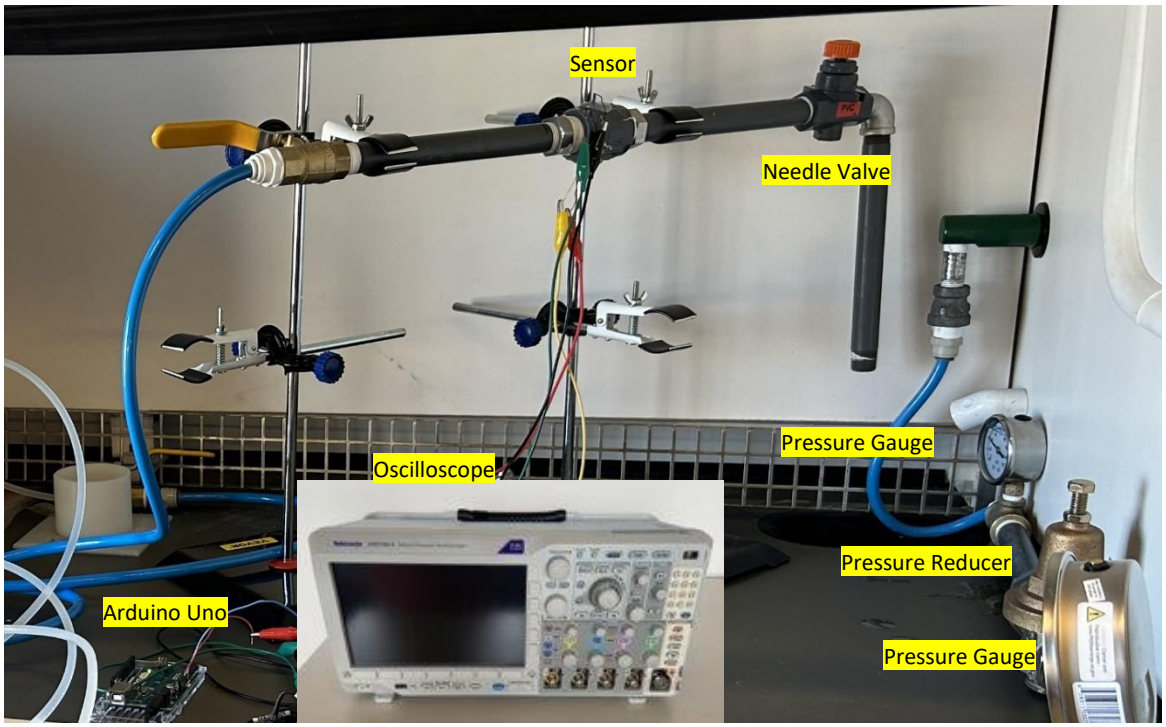

FIGURE 3-5. FLOW METERING TEST SETUP

3.5.7. Creep Test

A sample with the same geometry and size that was used for imaging with the area density of 0.0069 mg/mm2 was tested under constant uniaxial tension for creep. Sample was tested over time under strains of 0%, 7.57% and 10.59% using the same tensioning device that was made using 3D-printer. The distance between electrodes in the x direction was 1.43 mm. Test was performed at room temperature.

3.5.8. Fatigue Test

Fatigue test was performed on the sensor with 0.0069 mg/mm^2 area density by application of cyclic loading with 10 seconds of on-cycles with the average of 2496.871 ml/min flowrate and 10 seconds of off-cycles with zero ml/min of flowrate. The “on” and “off” cycles were created using a solenoid valve and a timer. The flowrate was adjusted by a needle valve. Pressure was adjusted by a pressure reducer to 34.4738 kPa (5 psi) pressure. Distances between electrodes in x, y and the oblique directions were measured as 1.37 mm, 7.28 mm, and 7.4 mm respectively. The same data acquisition system as tensile experiments were used with the same electrical bridges, oscilloscope and Arduino Uno (as a power supply). Temperature was kept in a constant range

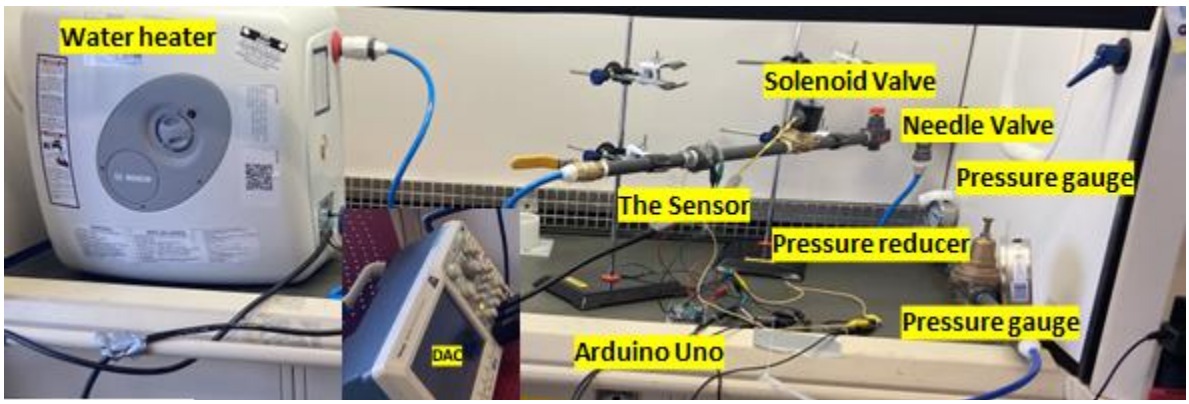

FIGURE 3-6. FATIGUE TESTING SET-UP

with the average of 22.72˚c using a water heater (Figure 3-6) to avoid effects of temperature variation on the resistive response of the sensor.

3.5.9. High Flowrate Survival

Sensor with 0.0069 mg/mm^2 and distances between electrodes of 0.88, 6.85, 7.81 in the x, y and the oblique directions respectively was tested at high flowrates up to 32035.83 ml/min. Test was performed at the average pressure and temperature of 227.52 kPa (33 psi) and 20˚c respectively. The same test set-up as the one used in flowrate testing was used in this experiment.

3.6. Results and Discussion

3.6.1. Factorial Analysis

As the Pareto chart in Figure 3-7 shows, flowrate was identified as the most effective factor. This result shows that the design is well suited for the purpose it was made for (flow metering). The existence of PDMS ring was identified as the second most effective factor. This result suggested that the sensitivity of the sensor could be enhanced by using a ring upstream next to the sensor.

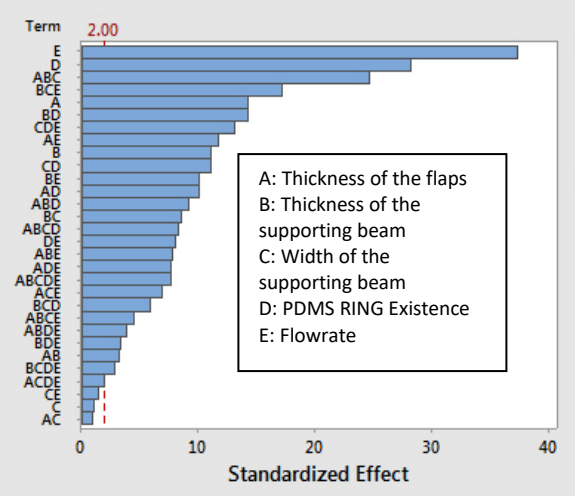

FIGURE 3-7. PARETO CHART OF THE EFFECTS OF THE PARAMETERS ON THE RESISTIVE RESPONSE

Combinatorial effect of all three geometric parameters (Thickness of the flaps and the supporting beam and the width of the supporting beam) was placed in the third rank showing that the effect of the three factors combined had the greater impact on the resistive response of the sensor than that of each factor individually.

3.6.2. Finite Element Analysis

It can be seen from Figure 3-8 that the deformations are the greatest at the tips of the flaps. However, finite element analysis performed in 2 paths at the center of the sensor aligned with y and x directions shown in Figure 3-9(a) and Figure 3-9(b) respectively, suggests that the resulting strains are the greatest on the top and bottom of the supporting beam close to where the sensor is restrained rather than in the middle. The values on the top and the bottom of the supporting middle beam are also greater than those on the tips of the flaps.

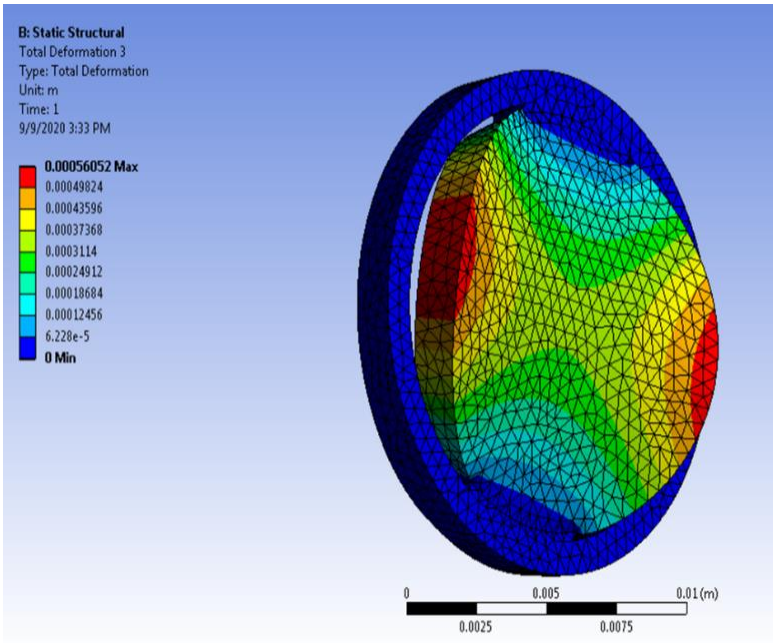

FIGURE 3-8. FINITE ELEMENT ANALYSIS PERFORMED ON THE SENSOR FOR DEFORMATION DEMONSTRATION

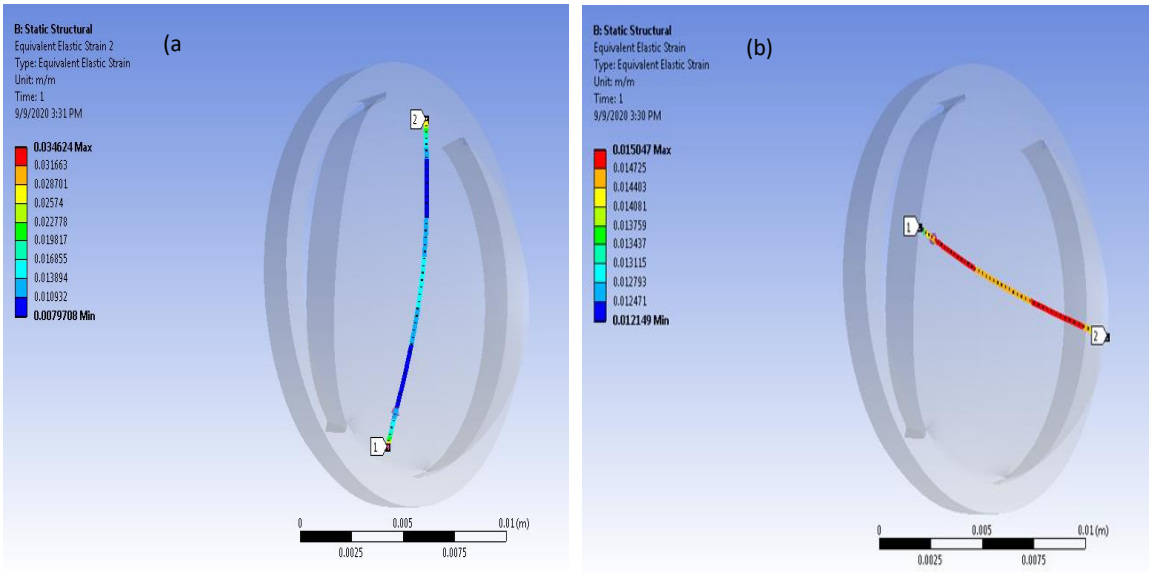

FIGURE 3-9. CONTOUR OF STRAIN WITHIN THE PATH THROUGH THE CENTER (A) IN THE Y DIRECTION (B) IN THE X DIRECTION

As can be seen from the plots of strain versus the length of the analyzed paths on Figure 3-10(a) and Figure 3-10(b) in the y and x directions respectively, magnitude of the strain in the sensor is a greater value at the top and bottom of the supporting beam rather than on the tips of the flaps. As a result of this analysis, the rGO patch was extended in the Y direction to enhance the sensitivity of the sensor to strain. Therefore, the initial square shape of the rGO film was replaced

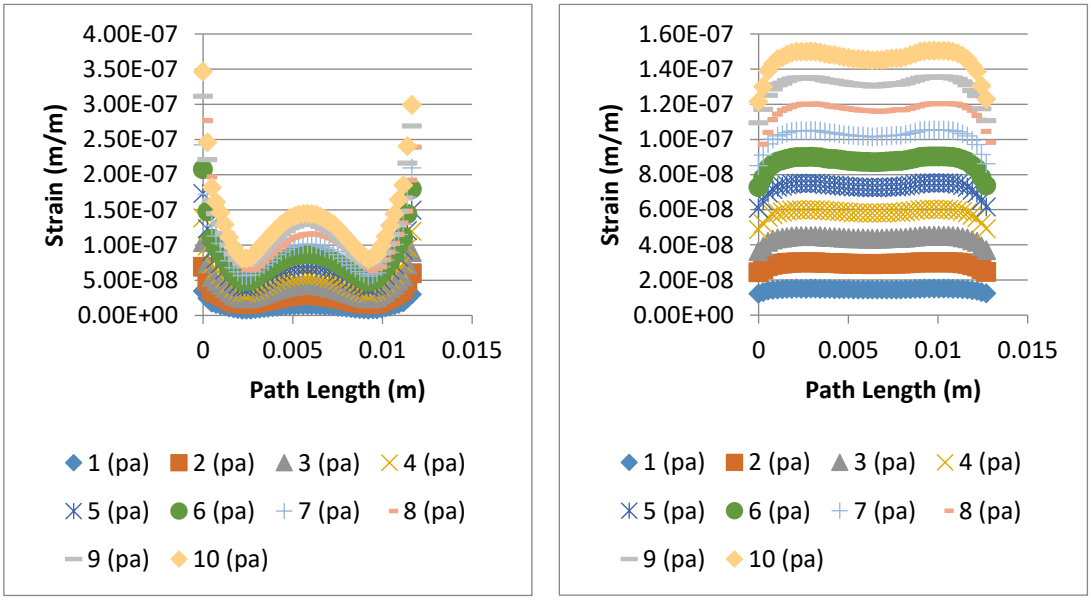

FIGURE 3-10. STRAIN WITHIN THE PATH THROUGH THE CENTER IN THE (A). Y DIRECTION (B). X DIRECTION

with a rectangular shape in the new design (Figure 3-3). Furthermore, the maximum strain that the initial body design of the sensor could be exposed to, under 1000kPa pressure was determined using finite element analysis as less than 3.5%.

3.6.3. Flow meter resistive response testing

Figure 3-11 shows the resistance and relative resistance change in all 3 directions in one plot with respect to applied flowrate. As the figure suggests, the sensor was sensitive to the stimulus. The sensor showed higher sensitivity in the y direction. Resolution of about 2ml/min was measured. The absolute value of the sensitivity of the sensor in the x, y and oblique directions were calculated as 0.0011 $\frac{\Omega/\Omega}{ml/min}$, 0.0036 $\frac{\Omega/\Omega}{ml/min}$ and 0.002020 $\frac{\Omega/\Omega}{ml/min}$ which matches the results of FEM that suggested greater sensitivity of the sensor in the y direction.

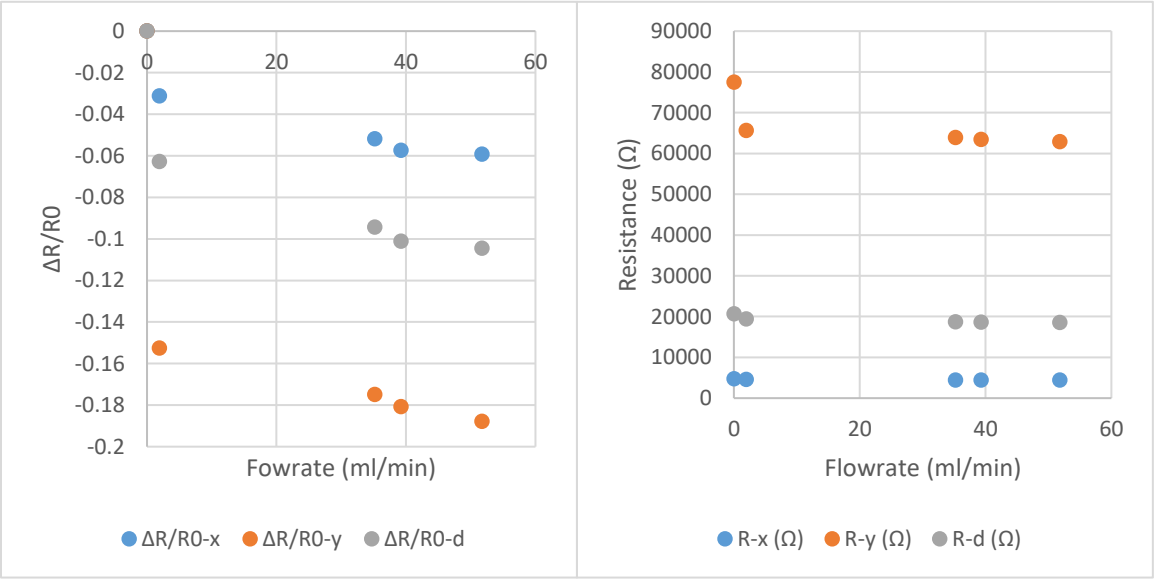

FIGURE 3-11. FE ANALYSIS IN THE PATH THROUGH THE CENTER IN THE (A). Y DIRECTION (B). X DIRECTION

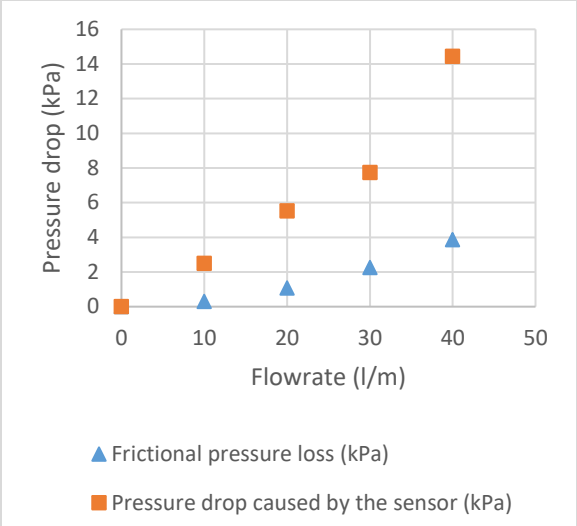

FIGURE 3-12. PRESSURE-DROP AT DIFFERENT FLOWRATES

3.6.4. Pressure-drop caused by the sensor.

As can be seen in Figure 3-12, the pressure-drop that sensor created at 40 l/min flowrate was 18.3 kPa where about 3.86 kPa of that value came from the frictional pressure loss in the pipe with diameter of 12.7 mm (half inch) and 45.72 cm long length. The frictional pressure loss was calculated based on Hazen–Williams Formula [161]. Therefore, only 14.44 kPa of the pressure-

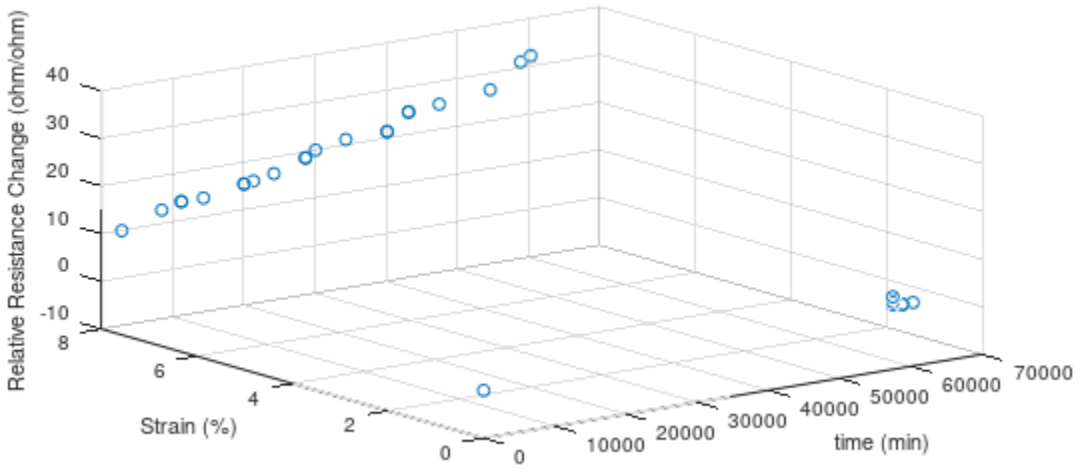

FIGURE 3-13. RESISTIVE RESPONSE OF THE SAMPLE DURING 57444 MIN (ABOUT 40 DAYS) UNDER 7.57% STRAIN

drop was caused by the sensor which is a very small amount of pressure-drop considering the pressure that pipes usually work at. For instance, residential water pressure ranges from about 310 kPa to about 550 kPa.

3.6.5. Creep Test

As shown in Figure 3-13, small increasing changes in the resistive response of the sensor were observed during 57444min (about 40 days) of being under 7.57% strain. After being released, the sensor's relative resistance change returned to almost the same value as its relaxed state's value was (before being strained) with only about 5 Ω/Ω difference. A sensor's ability to return to its initial output value after being released is an important aspect of its performance and can be one of the requirements toward fulfilling good repeatability criteria. The test was performed at room temperature. The sample showed on average an increasing trend over time. Part of the increase in relative resistance change could be attributed to the increase in temperature in the room over time (Figure 3-14).

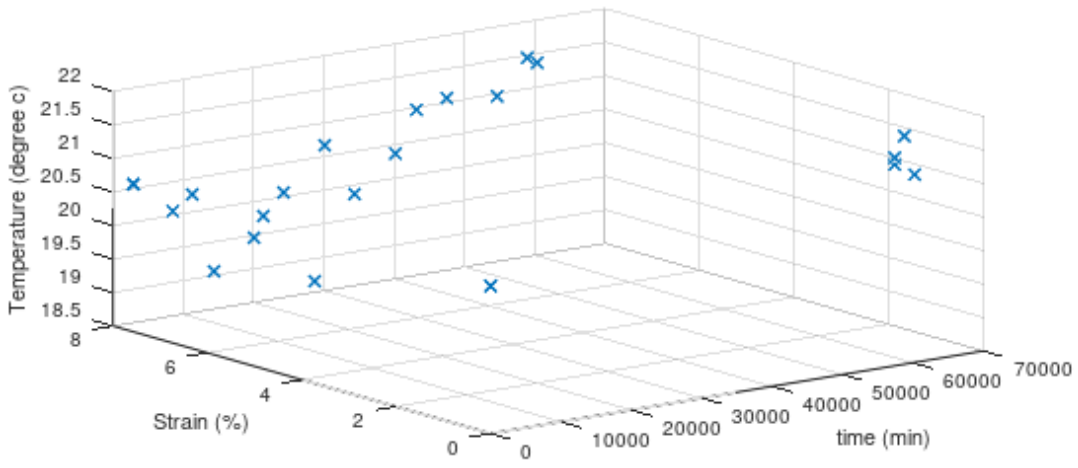

FIGURE 3-14. TEMPERATURE CHANGES DURING 57444 MIN (ABOUT 40 DAYS)

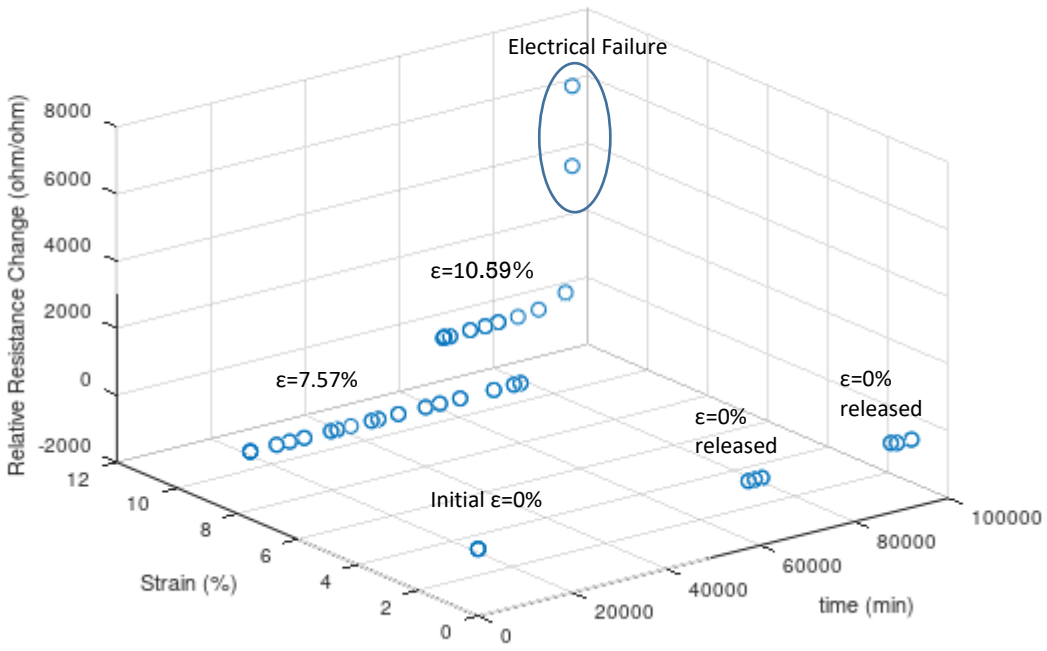

FIGURE 3-15. RESISTIVE RESPONSE OF THE SAMPLE DURING THE 59 DAYS

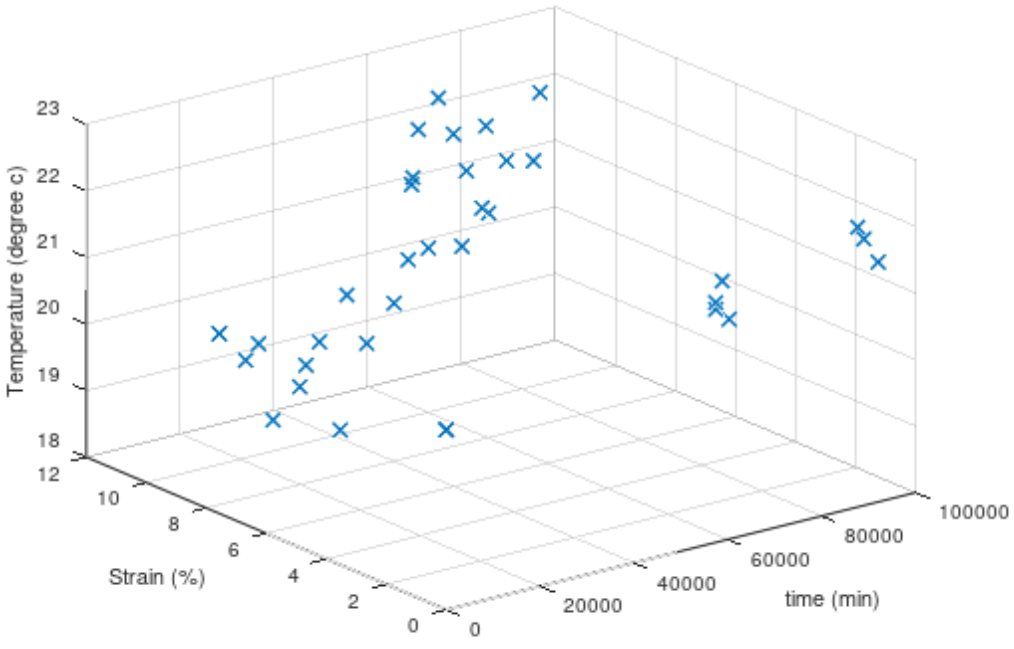

FIGURE 3-16. TEMPERATURE CHANGES DURING THE 59 DAYS

Sample then was tested under 10.59% strain. After 27394min (about 19 days) of constant tension the samples electrically failed (Figure 3-15). However, immediately after releasing the sample, the electrical conductivity of the sample was almost retrieved. After about 22 hours, $\frac{\Delta R}{R_0}$ returned to its initial relaxed state's value (with only 27 Ω/Ω difference). Change in temperature throughout the experiment is shown in Figure 3-16.

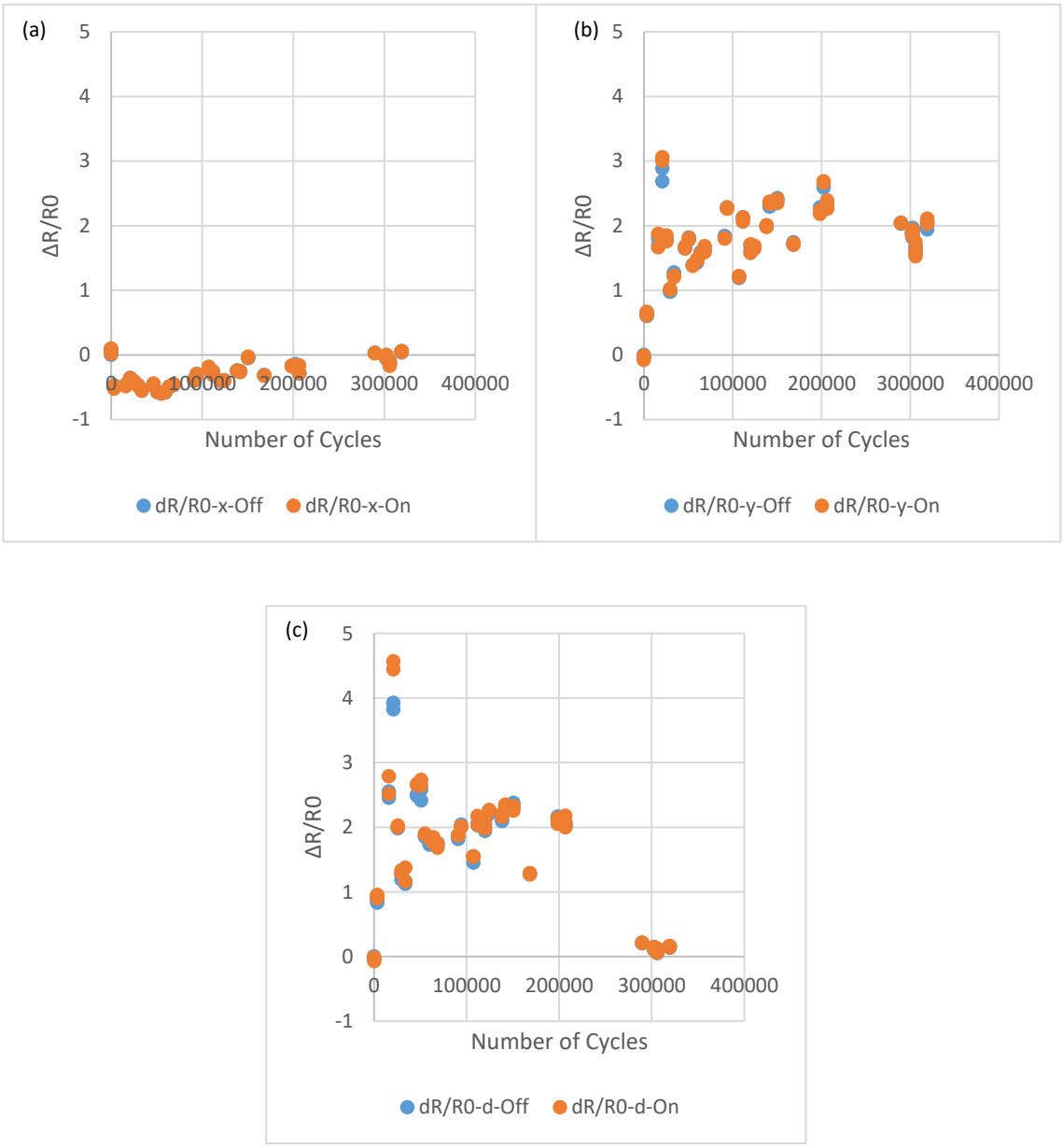

FIGURE 3-17. RESISTIVE RESPONSE OF THE SENSOR IN THE (A) X DIRECTION, (B) Y DIRECTION AND (C) AT THE ANGLE

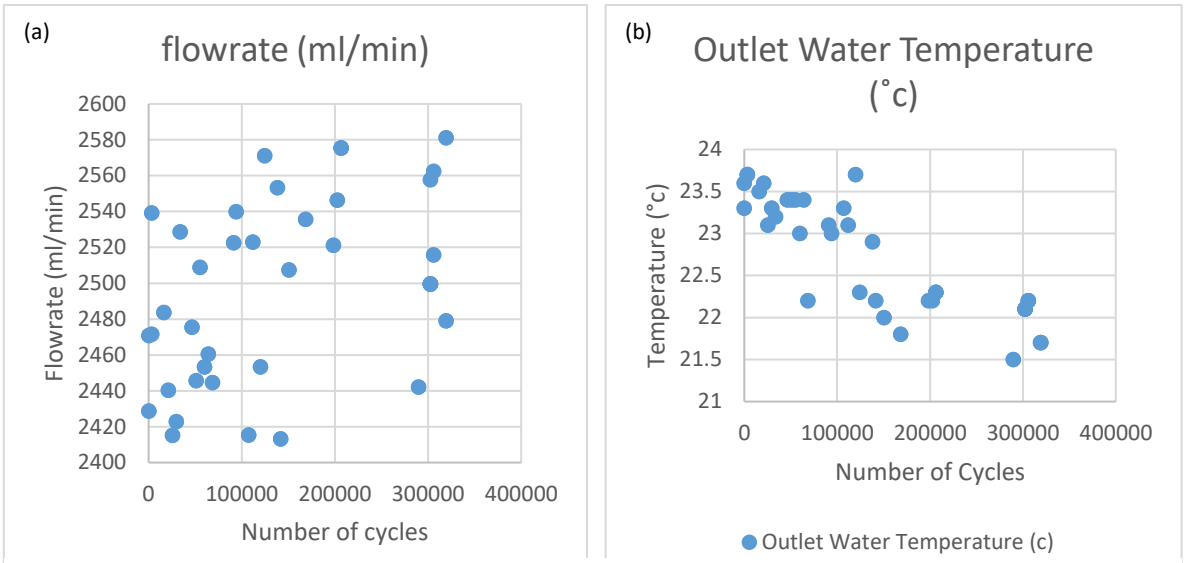

FIGURE 3-18. (A) FLOWRATE AT DIFFERENT CYCLES (B) TEMPERATURE AT DIFFERENT CYCLES.

3.6.6. Fatigue Test

As it is shown in Figure 3-17(a), Figure 3-17(b), and Figure 3-17(c) during about 319000 cycles, the resistive response of the sensor showed very consistent result with variation of only, ±1, ±3 and ±5 in x, y and the oblique directions respectively. Most of these small variations happened in the first 10000 cycles and then resistive response of the sensor was mostly stabilized. The sensor

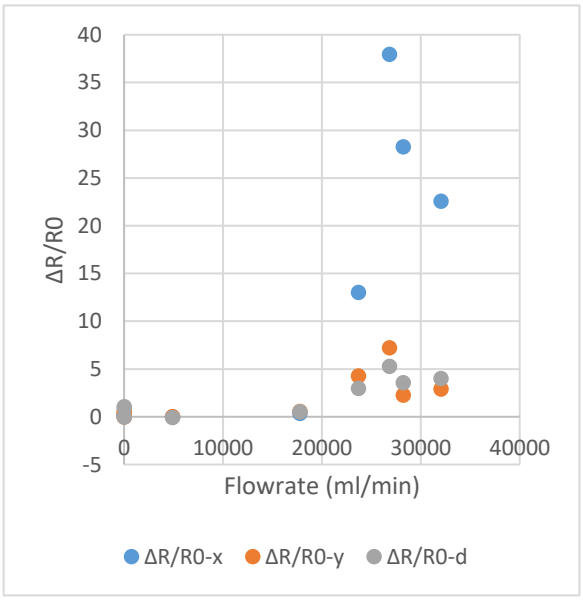

FIGURE 3-19. RESISTIVE RESPONSE OF THE SENSOR UP TO THE HIGHEST FLOWRATE THE SENSOR WAS TESTED

in the x direction showed the most consistency in resistive response during the fatigue test. The flowrate and temperature that were recorded for different cycles are shown in Figure 3-18(a) and Figure 3-18(b).

3.6.7. High flowrate survival

Figure 3-19 shows the highest flowrate that the sensor was tested up to. Not only did the sensor survive the flowrate as high as about 32035.83 ml/min but also once the applied flowrate returned to 0 ml/min, the resistive response of the sensor ($\Delta R/R_0$) returned to its initial value with the very small differences of 0.193999Ω/Ω, 0.424458 Ω/Ω and 0.8882 Ω/Ω in x, y and the oblique directions respectively.

3.7. Summary of Flow Meter Results

Factorial analysis performed on the flowmeter showed that flowrate was the first factor that the sensor was the most impacted by. It could be attributed to the good sensitivity of the sensor to flowrate. The second most effective factor was the presence of the PDMS ring in the upstream next to the sensor. The combinatorial effect of all three geometric parameters (Thickness of the flaps and the supporting beam and the width of the supporting beam) was identified as the third most effective factor. It means that the effect of the three factors combined had a greater impact on the resistive response of the sensor than that of each factor individually. Finite element analysis showed that the rGO film should be extended along the y axis to show the best sensitivity to the flowrate change. The flowrate test on the sensor showed that it was sensitive to flowrate change and the most sensitivity was achieved in the resistive response of the sensor in y direction which was consistent with the results of the finite element analysis. Pressure drop test performed

on the sensor showed that it created 14.44 kPa of pressure drop at 40 l/min flowrate which was a small amount of pressure drop considering residential water pipes being exposed to a pressure ranging from 310 kPa to about 550 kPa. The creep test showed a small increasing shift in the resistive response of the sensor during about 40 days of being under 7.57% strain. The increasing trend of the resistive response can be partially attributed to the increasing trend of temperature change in the room during data collection. During about 319000 cycles of cyclic testing, the resistive response of the sensor showed a very consistent result with variation of only, ±1, ±3 and ±5 in x, y and the oblique directions respectively. Testing the sensor at a flowrate as high as 32035.83 ml/min showed that not only did the sensor survive the high flowrate but also once the applied flowrate returned to 0 ml/min flowrate, the resistive response of the sensor ($\Delta R/R0$) returned to its initial value with the very small differences of 0.193999Ω/Ω, 0.424458 Ω/Ω and 0.8882 Ω/Ω in x, y and the oblique directions respectively.

4. CONCLUSION AND FUTURE WORK

4.1. Conclusion

Initial tests on the sensor tested under strains up to the electrical failure showed that rGO sensors with area densities of 0.0069 mg/mm^2, 0.0080 mg/mm^2, and 0.0091 mg/mm^2, electrically failed on average at 20.36%, 34.19% and 40.92% strains meaning that as the area density increased, the average strain values of electrical failure increased too. On average, the increase in the area density of the GO deposited on the substrate increased the strain tolerance of the samples. Samples with greater area densities showed reduction in gauge factors. However, GF values were still high enough for the sensors to be considered as highly sensitive strain sensors compared to common foil strain gauges. Sensors in most cases showed a linear followed by a nonlinear resistive behavior with the increasing trend in the x direction while under strain in the x direction. The linear resistive behavior of the sensor under strain was consistent with that of bulk like materials. The nonlinear resistive behavior of the sensor under strain was aligned with that of percolative materials. The linear-nonlinear and increasing resistive behavior of the sensor matched the mathematical models. In the y direction, the resistive response of the sensor was decreasing. This behavior of the sensor could be due to contraction in the rGO in the direction perpendicular to the direction of applied tension caused by Poisson's effect in the PDMS substrate. This decreasing trend matched the mathematical model. Partial positive slopes observed in the resistive response of the sensor in the y direction could be attributed to the cracks that formed locally in the direction aligned with the direction of applied tension creating local disconnections in the electrical paths in the y direction. At the angle, resistive response of

the sensor was mostly affected by the resistive response of the sensor in the x direction rather than the y direction. This major influence matched the equations derived from the concept of the transformation of strains in the rotated elements. Furthermore, the rGO strain gauge showed the average gauge factor of 91.503 with a linear fit which was significantly greater than GF of metal foil strain gauges (about 2). 4-cycle cyclic testing results showed that in most cases, there were noticeable variations between the resistive response values between cycles 1 and 2. The variation decreased between the next cycles. According to the confocal microscope images, this phenomenon could be attributed to the formation of the residual microcracks after the first cycle causing deviation in the resistive response between cycles one and two. These residual microcracks remained in place for the rest of the cycles causing smaller resistive response deviations between other cycles after the first cycle. Confocal microscope images also revealed that the crack formation rate increased starting at 7.57% strain and beyond which could be attributed to the movement of the flakes of rGO over each other due to percolative like behavior resulting in accumulation of flakes in some areas leaving the adjacent areas empty (crack formation). Measurements by the confocal microscope suggested an accumulation of the rGO flakes because of their interconnections starting at 7.57% strain further, leaving the adjacent areas empty (crack formation). The elevation differences observed in the atomic force microscopy images taken at 0% and 7.57% strains could be because of this accumulation of flakes as well.

The rGO strain sensor can be used in applications with requirements of high sensitivity, cost efficiency, especially in mass production. One of these applications can be identified as use of rGO strain sensor as a sensor in the body of a low-flowrate leak detection sensor. The application

of rGO strain sensor to create a low-cost, highly sensitive flow meter was investigated in the thesis. Factorial analysis performed on the flowmeter showed that flowrate was the first factor that the sensor was mostly impacted by. It could be attributed to the good sensitivity of the sensor to flowrate. The second most effective factor was the presence of the PDMS ring in the upstream next to the sensor. The combinatorial effect of all three geometric parameters (Thickness of the flaps and the supporting beam and the width of the supporting beam) was identified as the third most effective factor. It means that the effect of the three factors combined had a greater impact on the resistive response of the sensor than that of each factor individually. Finite element analysis showed that the rGO film should be extended along the y axis to show the best sensitivity to flowrate change. The flowrate test on the sensor showed that it was sensitive to flowrate change and the most sensitivity was achieved in the resistive response of the sensor in y direction which was consistent with the results of the finite element analysis. Pressure drop test performed on the sensor showed that it created 14.44 kPa of pressure drop at 40 l/min flowrate which was a small amount of pressure drop considering residential water pipes being exposed to a pressure ranging from 310 kPa to about 550 kPa. The creep test showed a small increasing shift in the resistive response of the sensor during about 40 days of being under 7.57% strain. The increasing trend of the resistive response can be partially attributed to the increasing trend of temperature change in the room during data collection. During about 319000 cycles of cyclic testing, the resistive response of the sensor showed a very consistent result with variation of only, ±1, ±3 and ±5 in x, y and the oblique directions respectively. Testing the sensor at a flowrate as high as 32035.83 ml/min showed that not only did the sensor survive the high flowrate but also once the applied flowrate returned to 0 ml/min flowrate, the resistive response

of the sensor (ΔR/R0) returned to its initial value with the very small differences of 0.193999Ω/Ω, 0.424458 Ω/Ω and 0.8882 Ω/Ω in x, y and the oblique directions respectively.

4.2. Future Work

Based on the results shown in application of the strain sensor in low-cost leak detection for health monitoring of the water equipment, temperature change in the environment that the sensor was tested in could potentially affect the resistive response of the sensor. Therefore, a quantitative investigation into effects of temperature change on the PDMS-rGO film sensor and the potential methods to compensate for these effects could be considered for future work.

REFERENCES

[1] H. Souri *et al.*, "Wearable and Stretchable Strain Sensors: Materials, Sensing Mechanisms, and Applications," *Advanced Intelligent Systems*, vol. 2, no. 8, p. 2000039, 2020, doi: https://doi.org/10.1002/aisy.202000039.

[2] A. C. Ugural, *Mechanics of Materials*, 1st ed. Wiley, 2007.

[3] Q. Xin, "Durability and reliability in diesel engine system design," in *Diesel Engine System Design*, Elsevier, 2013, pp. 113–202. doi: 10.1533/9780857090836.1.113.

[4] Ansel C. Ugural; Saul K. Fenster, *Advanced Mechanics of Materials and Applied Elasticity*, 5th ed. Prentice Hall, 2011.

[5] J. Fraden, *Handbook of Modern Sensors*, 4th ed. New York, NY: Springer New York, 2010. doi: 10.1007/978-1-4419-6466-3.

[6] Shulong Yao, Xu Nie, Xun Yu, Bo Song, and J. Blecke, "Highly Stretchable Miniature Strain Sensor for Large Dynamic Strain Measurement," *IEEE Sens Lett*, vol. 1, no. 3, pp. 1–4, 2017, doi: 10.1109/LSENS.2017.2709943.

[7] H. M. Soe, A. A. Manaf, A. Matsuda, and M. Jaafar, "Development and fabrication of highly flexible, stretchable, and sensitive strain sensor for long durability based on silver nanoparticles–polydimethylsiloxane composite," *Journal of Materials Science: Materials in Electronics*, vol. 31, no. 14, pp. 11897–11910, Jul. 2020, doi: 10.1007/s10854-020-03744-6.

[8] C. Yan *et al.*, "Highly Stretchable Piezoresistive Graphene-Nanocellulose Nanopaper for Strain Sensors," *Advanced Materials*, vol. 26, no. 13, pp. 2022–2027, Apr. 2014, doi: 10.1002/adma.201304742.

[9] J. Shintake, T. Nagai, and K. Ogishima, “Sensitivity Improvement of Highly Stretchable Capacitive Strain Sensors by Hierarchical Auxetic Structures,” *Front Robot AI*, vol. 6, Nov. 2019, doi: 10.3389/frobt.2019.00127.

[10] A. Arkhipov *et al.*, “Mechanical Stability of Filaments for ITER Diagnostic Pressure Gauges Relating to Creep and Fatigue,” *IEEE Transactions on Plasma Science*, vol. 48, no. 6, pp. 1661–1665, Jun. 2020, doi: 10.1109/TPS.2020.2968168.

[11] C. A. Sciammarella and F. M. Sciammarella, *Experimental Mechanics of Solids*. Wiley, 2012. doi: 10.1002/9781119994091.

[12] A. V. Tregubov, V. V. Svetukhin, S. G. Novikov, A. V. Berintsev, and V. V. Prikhodko, “A novel fiber optic distributed temperature and strain sensor for building applications,” *Results Phys*, vol. 6, pp. 131–132, 2016, doi: 10.1016/j.rinp.2016.01.008.

[13] Y.-G. Kim, J.-H. Song, S. Hong, and S.-H. Ahn, “Piezoelectric strain sensor with high sensitivity and high stretchability based on kirigami design cutting,” *npj Flexible Electronics*, vol. 6, no. 1, p. 52, Dec. 2022, doi: 10.1038/s41528-022-00186-4.

[14] M. Schlögl, S. Köpl, J. Hiesberger, M. Schneider, and U. Schmid, “Mechanical and electrical characterization of resonant piezoelectric microbridges for strain sensing,” *Sens Actuators A Phys*, vol. 346, p. 113829, Oct. 2022, doi: 10.1016/j.sna.2022.113829.

[15] M. Bao, “Introduction to MEMS Devices,” in *Analysis and Design Principles of MEMS Devices*, Elsevier, 2005, pp. 1–32. doi: 10.1016/b978-044451616-9/50002-3.

[16] H. Ji *et al.*, “Capacitance of carbon-based electrical double-layer capacitors,” *Nat Commun*, vol. 5, no. 1, p. 3317, Feb. 2014, doi: 10.1038/ncomms4317.

[17] W. Boyes, *Instrumentation Reference Book*. Oxford: Elsevier Science & Technology, 2009.

[18] J. G. Webster, *Wiley Encyclopedia of Electrical and Electronics Engineering*. Wiley, 1999. doi: 10.1002/047134608X.

[19] C. K. Alexander and S. Matthew, *Fundamentals of Electric Circuits*, 7th ed. McGraw-Hill, 2020.

[20] M. SEIKA and K. HOSONO, "Fundamental Study on a Foil Strain Gauge of Electrodeposited Nickel," *Bulletin of JSME*, vol. 25, no. 206, pp. 1240–1246, 1982, doi: 10.1299/jsme1958.25.1240.

[21] S. M. Won *et al.*, "Piezoresistive Strain Sensors and Multiplexed Arrays Using Assemblies of Single-Crystalline Silicon Nanoribbons on Plastic Substrates," *IEEE Trans Electron Devices*, vol. 58, no. 11, pp. 4074–4078, Nov. 2011, doi: 10.1109/TED.2011.2164923.

[22] M. Ying *et al.*, "Silicon nanomembranes for fingertip electronics," *Nanotechnology*, vol. 23, no. 34, p. 344004, Aug. 2012, doi: 10.1088/0957-4484/23/34/344004.

[23] D.-H. Kim *et al.*, "Electronic sensor and actuator webs for large-area complex geometry cardiac mapping and therapy," *Proceedings of the National Academy of Sciences*, vol. 109, no. 49, pp. 19910–19915, Dec. 2012, doi: 10.1073/pnas.1205923109.

[24] S. Yang and N. Lu, "Gauge Factor and Stretchability of Silicon-on-Polymer Strain Gauges," *Sensors*, vol. 13, no. 7, pp. 8577–8594, Jul. 2013, doi: 10.3390/s130708577.

[25] M.-H. Bao, *Micro Mechanical Transducers - Pressure Sensors, Accelerometers and Gyroscopes*, 1st ed. Amsterdam ; New York: Elsevier, 2000.

[26] M. Bao, "Mechanics of Beam and Diaphragm Structures," *Analysis and Design Principles of MEMS Devices*, pp. 33–114, Jan. 2005, doi: 10.1016/B978-044451616-9/50003-5.

[27] J. L. Tanner, D. Mousadakos, P. Broutas, S. Chatzandroulis, Y. S. Raptis, and D. Tsoukalas, "Nanoparticle Strain Sensor," *Procedia Eng*, vol. 25, pp. 635–638, 2011, doi: https://doi.org/10.1016/j.proeng.2011.12.158.

[28] K. K. Ng, "Strain Gauge," in *Complete Guide to Semiconductor Devices*, Hoboken, NJ, USA: John Wiley & Sons, Inc., 2010, pp. 544–550. doi: 10.1002/9781118014769.ch72.

[29] *Molecular Sensors and Nanodevices*. Elsevier, 2019. doi: 10.1016/C2017-0-02290-5.

[30] I. Khan, K. Saeed, and I. Khan, "Nanoparticles: Properties, applications and toxicities," *Arabian Journal of Chemistry*, vol. 12, no. 7, pp. 908–931, Nov. 2019, doi: 10.1016/j.arabjc.2017.05.011.

[31] A. V. Rane, K. Kanny, V. K. Abitha, and S. Thomas, "Methods for Synthesis of Nanoparticles and Fabrication of Nanocomposites," in *Synthesis of Inorganic Nanomaterials*, Elsevier, 2018, pp. 121–139. doi: 10.1016/B978-0-08-101975-7.00005-1.

[32] N. M. Sangeetha, N. Decorde, B. Viallet, G. Viau, and L. Ressier, "Nanoparticle-Based Strain Gauges Fabricated by Convective Self Assembly: Strain Sensitivity and Hysteresis with Respect to Nanoparticle Sizes," *The Journal of Physical Chemistry C*, vol. 117, no. 4, pp. 1935–1940, Jan. 2013, doi: 10.1021/jp310077r.

[33] J. T. Buchman, N. V. Hudson-Smith, K. M. Landy, and C. L. Haynes, "Understanding Nanoparticle Toxicity Mechanisms To Inform Redesign Strategies To Reduce Environmental Impact," *Acc Chem Res*, vol. 52, no. 6, pp. 1632–1642, Jun. 2019, doi: 10.1021/acs.accounts.9b00053.

[34] L. Ou *et al.*, "Toxicity of graphene-family nanoparticles: a general review of the origins and mechanisms," *Part Fibre Toxicol*, vol. 13, no. 1, p. 57, 2016, doi: 10.1186/s12989-016-0168-y.

[35] C. Yan *et al.*, “Highly Stretchable Piezoresistive Graphene-Nanocellulose Nanopaper for Strain Sensors,” *Advanced materials (Weinheim)*, vol. 26, no. 13, pp. 2022–2027, 2014, doi: 10.1002/adma.201304742.

[36] J. Zhao, G.-Y. Zhang, and D.-X. Shi, “Review of graphene-based strain sensors,” *Chinese Physics B*, vol. 22, no. 5, p. 057701, May 2013, doi: 10.1088/1674-1056/22/5/057701.

[37] F. S. Irani *et al.*, “Graphene as a Piezoresistive Material in Strain Sensing Applications,” *Micromachines (Basel)*, vol. 13, no. 1, p. 119, Jan. 2022, doi: 10.3390/mi13010119.

[38] I. I. Kondrashov, M. G. Rybin, E. A. Obraztsova, and E. D. Obraztsova, “Controlled Graphene Synthesis from Solid Carbon Sources,” *physica status solidi (b)*, vol. 256, no. 9, p. 1800688, Sep. 2019, doi: 10.1002/pssb.201800688.

[39] H. Brody, “Graphene,” *Nature*, vol. 483, no. 7389, pp. S29–S29, Mar. 2012, doi: 10.1038/483S29a.

[40] T. Ma *et al.*, “Tailoring the thermal and electrical transport properties of graphene films by grain size engineering,” *Nat Commun*, vol. 8, no. 1, p. 14486, Feb. 2017, doi: 10.1038/ncomms14486.

[41] Md. S. A. Bhuyan, Md. N. Uddin, Md. M. Islam, F. A. Bipasha, and S. S. Hossain, “Synthesis of graphene,” *Int Nano Lett*, vol. 6, no. 2, pp. 65–83, Jun. 2016, doi: 10.1007/s40089-015-0176-1.

[42] W. Choi and J. Lee, Eds., *Graphene*. CRC Press, 2016. doi: 10.1201/b11259.

[43] N. I. Zaaba, K. L. Foo, U. Hashim, S. J. Tan, W.-W. Liu, and C. H. Voon, “Synthesis of Graphene Oxide using Modified Hummers Method: Solvent Influence,” *Procedia Eng*, vol. 184, pp. 469–477, 2017, doi: 10.1016/j.proeng.2017.04.118.

[44] F. M. Casallas Caicedo *et al.*, “Synthesis of graphene oxide from graphite by ball milling,” *Diam Relat Mater*, vol. 109, p. 108064, Nov. 2020, doi: 10.1016/j.diamond.2020.108064.

[45] K. Y. Chong, C. H. Chia, S. W. Chook, S. Zakaria, and D. Lucas, “Simplified production of graphene oxide assisted by high shear exfoliation of graphite with controlled oxidation,” *New Journal of Chemistry*, vol. 42, no. 6, pp. 4507–4512, 2018, doi: 10.1039/C7NJ04911K.

[46] J.-O. Carlsson and P. M. Martin, “Chemical Vapor Deposition,” in *Handbook of Deposition Technologies for Films and Coatings*, Elsevier, 2010, pp. 314–363. doi: 10.1016/B978-0-8155-2031-3.00007-7.

[47] E. P. Randviir, D. A. C. Brownson, and C. E. Banks, “A decade of graphene research: production, applications and outlook,” *Materials Today*, vol. 17, no. 9, pp. 426–432, Nov. 2014, doi: 10.1016/j.mattod.2014.06.001.

[48] W. Liu and G. Speranza, “Tuning the Oxygen Content of Reduced Graphene Oxide and Effects on Its Properties,” *ACS Omega*, vol. 6, no. 9, pp. 6195–6205, Mar. 2021, doi: 10.1021/acsomega.0c05578.

[49] J. M. González-Domínguez, V. León, M. I. Lucío, M. Prato, and E. Vázquez, “Production of ready-to-use few-layer graphene in aqueous suspensions,” *Nat Protoc*, vol. 13, no. 3, pp. 495–506, 2018, doi: 10.1038/nprot.2017.142.

[50] M. Rezaee, L.-C. Tsai, M. I. Haider, A. Yazdi, E. Sanatizadeh, and N. P. Salowitz, “Quantitative peel test for thin films/layers based on a coupled parametric and statistical study,” *Sci Rep*, vol. 9, no. 1, 2019, doi: 10.1038/s41598-019-55355-9.

[51] L.-C. Tsai, M. Rezaee, M. I. Haider, A. Yazdi, and N. P. Salowitz, “Quantitative measurement of thin film adhesion force,” in *ASME 2019 Conference on Smart Materials, Adaptive Structures and Intelligent Systems, SMASIS 2019*, 2019. doi: 10.1115/SMASIS2019-5615.

[52] M. Rezaee, L. Chih Tsai, A. Elyasigorji, M. Istiaque Haider, A. Yazdi, and N. P. Salowitz, "Quantification of the Mechanical Strength of Thermally Reduced Graphene Oxide Layers on Flexible Substrates," *Eng Fract Mech*, p. 107525, Jan. 2021, doi: 10.1016/j.engfracmech.2021.107525.

[53] M. I. Haider, A. Yazdi, M. Rezaee, L. C. Tsai, and N. Salowitz, "Mechanics of post constrained recovery residual stress produced by NiTi," *ASME 2019 Conference on Smart Materials, Adaptive Structures and Intelligent Systems, SMASIS 2019*, pp. 1–6, 2019, doi: 10.1115/SMASIS2019-5619.

[54] A. Yazdi, L.-C. Tsai, and N. Salowitz, "Investigation of the Resistive Response of Reduced Graphene Oxide for Sensing Large Strains (\\>10\\%)," in Smart Materials, Adaptive Structures and Intelligent Systems, vol. ASME 2022. 2022. doi: 10.1115/SMASIS2022-90349.

[55] X. M. Zhang, X. L. Yang, and K. Y. Wang, "Conductive graphene/polydimethylsiloxane nanocomposites for flexible strain sensors," *Journal of Materials Science: Materials in Electronics*, vol. 30, no. 21, pp. 19319–19324, 2019, doi: 10.1007/s10854-019-02292-y.

[56] Paras and A. Kumar, "Anti-Wetting Polymeric Coatings," in *Encyclopedia of Materials: Plastics and Polymers*, Elsevier, 2022, pp. 786–795. doi: 10.1016/B978-0-12-820352-1.00141-3.

[57] A. Holm, C. J. Wrasman, K.-C. Kao, A. R. Riscoe, M. Cargnello, and C. W. Frank, "Langmuir–Blodgett Deposition of Graphene Oxide Identifying Marangoni Flow as a Process that Fundamentally Limits Deposition Control," *Langmuir*, vol. 34, no. 33, pp. 9683–9691, 2018, doi: 10.1021/acs.langmuir.8b00777.

[58] H. Kim *et al.*, "Optoelectronic properties of graphene thin films deposited by a Langmuir–Blodgett assembly," *Nanoscale*, vol. 5, no. 24, p. 12365, 2013, doi: 10.1039/c3nr02907g.

[59] A. Holm, C. J. Wrasman, K.-C. Kao, A. R. Riscoe, M. Cargnello, and C. W. Frank, "Langmuir–Blodgett Deposition of Graphene Oxide—Identifying Marangoni Flow as a Process that Fundamentally Limits Deposition Control," *Langmuir*, vol. 34, no. 33, pp. 9683–9691, Aug. 2018, doi: 10.1021/acs.langmuir.8b00777.

[60] S. Azizighannad and S. Mitra, "Stepwise Reduction of Graphene Oxide (GO) and Its Effects on Chemical and Colloidal Properties," *Sci Rep*, vol. 8, no. 1, p. 10083, Dec. 2018, doi: 10.1038/s41598-018-28353-6.

[61] T. N. I. for O. S. and H. (NIOSH), "Hydrazine," *Centers for Disease Control and Prevention*, 2019. https://www.cdc.gov/niosh/topics/hydrazine/default.html#print

[62] D. Karačić *et al.*, "Electrochemical reduction of thin graphene-oxide films in aqueous solutions – Restoration of conductivity," *Electrochim Acta*, vol. 410, p. 140046, Apr. 2022, doi: 10.1016/j.electacta.2022.140046.

[63] S. Santoso and H. W. Beaty, *Standard Handbook for Electrical Engineers*, 17th ed. McGraw Hill, 2018.

[64] J. S. Wilson, *Sensor Technology Handbook*. Oxford: Elsevier Science & Technology, 2004.

[65] W. M. Murray and W. R. Miller, *The Bonded Electrical Resistance Strain Gage: An Introduction*. Cary: Oxford University Press, Incorporated, 1992.

[66] R. Mukherjee, "Correlation effects in nanoparticle composites: Percolation, packing and tunneling," Wayne State University, Michigan, 2014.

[67] S. R. Broadbent and J. M. Hammersley, "Percolation processes," *Mathematical Proceedings of the Cambridge Philosophical Society*, vol. 53, no. 3, pp. 629–641, Jul. 1957, doi: 10.1017/S0305004100032680.

[68] H. Yao, M. Hempel, Y.-P. Hsieh, J. Kong, and M. Hofmann, “Characterizing percolative materials by straining,” *Nanoscale*, vol. 11, no. 3, pp. 1074–1079, 2019, doi: 10.1039/C8NR09120J.

[69] B. M. Pirzada and S. Sabir, “5 - Polymer-based nanocomposites for significantly enhanced dielectric properties and energy storage capability,” in *Polymer-based Nanocomposites for Energy and Environmental Applications*, M. Jawaid and M. M. Khan, Eds., in Woodhead Publishing Series in Composites Science and Engineering. Woodhead Publishing, 2018, pp. 131–183. doi: https://doi.org/10.1016/B978-0-08-102262-7.00005-2.

[70] M. F. Clayton, R. A. Bilodeau, A. E. Bowden, and D. T. Fullwood, “Nanoparticle orientation distribution analysis and design for polymeric piezoresistive sensors,” *Sens Actuators A Phys*, vol. 303, p. 111851, Mar. 2020, doi: 10.1016/j.sna.2020.111851.

[71] A. J. Marsden *et al.*, “Electrical percolation in graphene–polymer composites,” *2d Mater*, vol. 5, no. 3, p. 032003, Jun. 2018, doi: 10.1088/2053-1583/aac055.

[72] A. Kumar, “Electrical Percolation in Metal Wire Network-Based Strain Sensors,” *IEEE Sens J*, vol. 19, no. 22, pp. 10373–10378, 2019, doi: 10.1109/JSEN.2019.2933239.

[73] A. Stauffer, Dietrich; Aharony, *Introduction To Percolation Theory*, 2nd ed. Taylor & Francis, 1994.

[74] D. Wang, X. Zhang, J.-W. Zha, J. Zhao, Z.-M. Dang, and G.-H. Hu, “Dielectric properties of reduced graphene oxide/polypropylene composites with ultralow percolation threshold,” *Polymer (Guildf)*, vol. 54, no. 7, pp. 1916–1922, Mar. 2013, doi: 10.1016/j.polymer.2013.02.012.

[75] T. Chelidze and Y. Gueguen, “Pressure-induced percolation transitions in composites,” *J Phys D Appl Phys*, vol. 31, no. 20, pp. 2877–2885, Oct. 1998, doi: 10.1088/0022-3727/31/20/023.

[76] S. De, P. J. King, P. E. Lyons, U. Khan, and J. N. Coleman, “Size Effects and the Problem with Percolation in Nanostructured Transparent Conductors,” *ACS Nano*, vol. 4, no. 12, pp. 7064–7072, Dec. 2010, doi: 10.1021/nn1025803.

[77] M. Sahini and M. Sahimi, *Applications Of Percolation Theory*. CRC Press, 1994. doi: 10.1201/9781482272444.

[78] G. B. West, J. H. Brown, and B. J. Enquist, “A General Model for the Origin of Allometric Scaling Laws in Biology,” *Science (1979)*, vol. 276, no. 5309, pp. 122–126, Apr. 1997, doi: 10.1126/science.276.5309.122.

[79] Z. Jiang, J. Zhao, and H. Xie, “Scaling Laws,” in *Microforming Technology*, Elsevier, 2017, pp. 53–71. doi: 10.1016/B978-0-12-811212-0.00003-0.

[80] J. Wang, H. L. Duan, Z. P. Huang, and B. L. Karihaloo, “A scaling law for properties of nano-structured materials,” *Proceedings of the Royal Society A: Mathematical, Physical and Engineering Sciences*, vol. 462, no. 2069, pp. 1355–1363, May 2006, doi: 10.1098/rspa.2005.1637.

[81] W. Bauhofer and J. Z. Kovacs, “A review and analysis of electrical percolation in carbon nanotube polymer composites,” *Compos Sci Technol*, vol. 69, no. 10, pp. 1486–1498, Aug. 2009, doi: 10.1016/j.compscitech.2008.06.018.

[82] N. Johner, C. Grimaldi, I. Balberg, and P. Ryser, “Transport exponent in a three-dimensional continuum tunneling-percolation model,” *Phys. Rev. B*, vol. 77, no. 17, p. 174204, May 2008, doi: 10.1103/PhysRevB.77.174204.

[83] D. Toker, D. Azulay, N. Shimoni, I. Balberg, and O. Millo, “Tunneling and percolation in metal-insulator composite materials,” *Phys. Rev. B*, vol. 68, no. 4, p. 41403, Jul. 2003, doi: 10.1103/PhysRevB.68.041403.

[84] B. Nigro, C. Grimaldi, and P. Ryser, “Tunneling and percolation transport regimes in segregated composites,” *Phys. Rev. E*, vol. 85, no. 1, p. 11137, Jan. 2012, doi: 10.1103/PhysRevE.85.011137.

[85] S. Vionnet-Menot, C. Grimaldi, T. Maeder, S. Strässler, and P. Ryser, “Tunneling-percolation origin of nonuniversality: Theory and experiments,” *Phys. Rev. B*, vol. 71, no. 6, p. 64201, Feb. 2005, doi: 10.1103/PhysRevB.71.064201.

[86] G. Ambrosetti, N. Johner, C. Grimaldi, T. Maeder, P. Ryser, and A. Danani, “Electron tunneling in conductor-insulator composites with spherical fillers,” *J Appl Phys*, vol. 106, no. 1, p. 016103, Jul. 2009, doi: 10.1063/1.3159040.

[87] S. Sorel, P. E. Lyons, S. De, J. C. Dickerson, and J. N. Coleman, “The dependence of the optoelectrical properties of silver nanowire networks on nanowire length and diameter,” *Nanotechnology*, vol. 23, no. 18, p. 185201, Apr. 2012, doi: 10.1088/0957-4484/23/18/185201.

[88] S. De *et al.*, “Flexible, Transparent, Conducting Films of Randomly Stacked Graphene from Surfactant-Stabilized, Oxide-Free Graphene Dispersions,” *Small*, vol. 6, no. 3, pp. 458–464, Feb. 2010, doi: 10.1002/smll.200901162.

[89] P. E. Lyons *et al.*, “High-Performance Transparent Conductors from Networks of Gold Nanowires,” *J Phys Chem Lett*, vol. 2, no. 24, pp. 3058–3062, Dec. 2011, doi: 10.1021/jz201401e.

[90] S. De *et al.*, “Flexible, Transparent, Conducting Films of Randomly Stacked Graphene from Surfactant-Stabilized, Oxide-Free Graphene Dispersions,” *Small*, vol. 6, no. 3, pp. 458–464, Feb. 2010, doi: 10.1002/smll.200901162.

[91] M. Iqra, F. Anwar, R. Jan, and M. A. Mohammad, “A flexible piezoresistive strain sensor based on laser scribed graphene oxide on polydimethylsiloxane,” *Sci Rep*, vol. 12, no. 1, p. 4882, 2022, doi: 10.1038/s41598-022-08801-0.

[92] K. Madhavi, M. Krishna, and C. Murthy, “Effect of Diaphragm Geometry and Piezoresistor Dimensions on the Sensitivity of a Piezoresistive Micropressure Sensor using Finite Element Analysis,” *Ijese.Org*, no. 9, pp. 35–40, 2013.

[93] N. Shayan, M. Tayyaba, M. Muhammad, and A. M. Mohammad, “A laser scribed graphene oxide and polyimide hybrid strain sensor,” *Key Eng Mater*, vol. 778 KEM, pp. 169–174, 2018, doi: 10.4028/www.scientific.net/KEM.778.169.

[94] INSTRON, “5980 Series Universal Testing System | Up to 600 kN Force Capacity.” https://www.instron.com/en-us/products/testing-systems/universal-testing-systems/high-force-universal-testing-systems/5989-floor-model (accessed Mar. 23, 2022).

[95] A. Yazdi, L.-C. Tsai, and N. Salowitz, “Investigation of the Resistive Response of Reduced Graphene Oxide for Sensing Large Strains (>10%),” in *ASME 2022 Conference on Smart Materials, Adaptive Structures and Intelligent Systems*, American Society of Mechanical Engineers, Sep. 2022. doi: 10.1115/SMASIS2022-90349.

[96] A. Yazdi, L.-C. Tsai, M. Rezaee, S. Gore, and N. Salowitz, “Low Flow Rate Measurement and Leak Detection for Health Monitoring of Water Equipment,” in *10th European Workshop on Structural Health Monitoring (10th EWSHM)*, Palermo: Springer Nature, 2023, pp. 963–971.

[97] T. Trantidou, Y. Elani, E. Parsons, and O. Ces, “Hydrophilic surface modification of PDMS for droplet microfluidics using a simple, quick, and robust method via PVA deposition,” *Microsyst Nanoeng*, vol. 3, no. 1, p. 16091, Apr. 2017, doi: 10.1038/micronano.2016.91.

[98] The Dow Chemical Company ("Dow"), "SYLGARD™ 186 Silicone Elastomer Technical Datasheet," *The Dow Chemical Company ("Dow")*, 2017. https://www.dow.com/content/dam/dcc/documents/en-us/productdatasheet/11/11-12/11-1253-sylgard-186-silicone-elastomer.pdf?iframe=true (accessed Jul. 07, 2020).

[99] Plasma Etch, "Palsma Etch PE-25 Plasma Etcher Datasheet," *Plasma Etch*, 2020. https://www.plasmaetch.com/images/pe25-flyer.pdf (accessed Jul. 07, 2020).

[100] Sigma-Aldrich, "(3-Aminopropyl)triethoxysilane Datasheet," *Sigma-Aldrich*, 2020. https://www.sigmaaldrich.com/Graphics/COfAInfo/SigmaSAPQM/SPEC/44/440140/440140-BULK_____ALDRICH__.pdf (accessed Jul. 07, 2020).

[101] Graphenea, "Graphenea Graphene Oxide (GO) Datasheet," *Graphenea*, 2019. https://cdn.shopify.com/s/files/1/0191/2296/files/Graphenea_GO_4mgmL_Datasheet_201905.pdf?22 (accessed Jul. 07, 2020).

[102] Cole Parmer, "Cole Parmer Ultrasonic Bath M-Series Operating Manual," *Cole Parmer*. https://pim-resources.coleparmer.com/instruction-manual/08895-xx.pdf (accessed Jul. 07, 2020).

[103] MTI Corporation, "OTF-1200 Series Split Tube Furnaces Operational Manual," *MTI Corporation*, 2009. https://www.ti.com/lit/ds/symlink/ina125.pdf?ts=1594693485905&ref_url=https%253A%252F%252Fwww.ti.com%252Fproduct%252FINA125 (accessed Jul. 07, 2020).

[104] Maysam Rezaee, "Bonding Evaluation of Graphene-Oxide Layers on Flexible Substrates," University of Wisconsin Milwaukee, 2021.

[105] Tektronix, “MDO3000 Series Datasheet,” *Tektronix*, 2020. https://download.tek.com/datasheet/MDO3000-Oscilloscope-Datasheet-48W3002012.pdf (accessed Jul. 07, 2020).

[106] Arduino, “Arduino Uno Board Specifications,” *Arduino*, 2020. https://www.makerspaces.com/wp-content/uploads/2017/02/Arduino-For-Beginners-REV2.pdf (accessed Jul. 07, 2020).

[107] J. L. Gómez-Urbano, J. L. Gómez-Cámer, C. Botas, T. Rojo, and D. Carriazo, “Graphene oxide-carbon nanotubes aerogels with high sulfur loadings suitable as binder-free cathodes for high performance lithium sulfur batteries,” *J Power Sources*, vol. 412, pp. 408–415, Feb. 2019, doi: 10.1016/j.jpowsour.2018.11.077.

[108] H. Lee *et al.*, “Preparation of fabric strain sensor based on graphene for human motion monitoring,” *J Mater Sci*, vol. 53, no. 12, pp. 9026–9033, Jun. 2018, doi: 10.1007/s10853-018-2194-7.

[109] M. Krystek *et al.*, “High-Performance Graphene-Based Cementitious Composites,” *Advanced Science*, vol. 6, no. 9, p. 1801195, May 2019, doi: 10.1002/advs.201801195.

[110] Graphenea, “Graphene Oxide Water Dispersion (0.4 wt% Concentration).”

[111] Graphenea, “Frequently Asked Questions-Graphenea.”

[112] W. A. Altabey, L. Wang, and M. Noori, *Using ANSYS for Finite Element Analysis, Volume I: A Tutorial for Engineers*. Momentum Press, 2018.

[113] A. Alawadhi and D. M. Tartakovsky, “Bayesian Update and Method of Distributions: Application to Leak Detection in Transmission Mains,” *Water Resour Res*, vol. 56, no. 2, Feb. 2020, doi: 10.1029/2019WR025879.

[114] Centers for Disease Control and Prevention (CDC), “Global Water, Sanitation, & Hygiene (WASH).” https://www.cdc.gov/healthywater/global/wash_statistics.html#:~:text=Access to Clean Water%2C Sanitation%2C and Hygiene&text=The latest published information on,have safe water to drink. (accessed Sep. 02, 2022).

[115] EPA.GOV, “WaerSense-Statistics and Facts.” https://www.epa.gov/watersense/statistics-and-facts#:~:text=Water Stats,gallons of water annually nationwide. (accessed Jul. 02, 2022).

[116] J. Choi, G. Jeong, and D. Kang, “Multiple Leak Detection in Water Distribution Networks Following Seismic Damage,” *Sustainability*, vol. 13, no. 15, p. 8306, Jul. 2021, doi: 10.3390/su13158306.

[117] Q. Xu, R. Liu, Q. Chen, and R. Li, “Review on water leakage control in distribution networks and the associated environmental benefits,” *Journal of Environmental Sciences*, vol. 26, no. 5, pp. 955–961, May 2014, doi: 10.1016/S1001-0742(13)60569-0.

[118] R. Collins, J. Boxall, M.-C. Besner, S. Beck, and B. Karney, “Intrusion Modelling and the Effect of Ground Water Conditions,” in *Water Distribution Systems Analysis 2010*, Reston, VA: American Society of Civil Engineers, Dec. 2011, pp. 585–594. doi: 10.1061/41203(425)55.

[119] D. Vacs Renwick, A. Heinrich, R. Weisman, H. Arvanaghi, and K. Rotert, “Potential Public Health Impacts of Deteriorating Distribution System Infrastructure,” *Journal AWWA*, vol. 111, no. 2, pp. 42–53, Feb. 2019, doi: 10.1002/awwa.1235.

[120] M. W. LeChevallier, R. W. Gullick, M. R. Karim, M. Friedman, and J. E. Funk, “The potential for health risks from intrusion of contaminants into the distribution system from pressure transients.,” *J Water Health*, vol. 1, no. 1, pp. 3–14, Mar. 2003.

[121] N. R. Council, *Drinking Water Distribution Systems: Assessing and Reducing Risks*. Washington, DC: The National Academies Press, 2006. doi: 10.17226/11728.

[122] S. El-Zahab and T. Zayed, “Leak detection in water distribution networks: an introductory overview,” *Smart Water*, vol. 4, no. 1, p. 5, 2019, doi: 10.1186/s40713-019-0017-x.

[123] R. Xiao, Q. Hu, and J. Li, “Leak detection of gas pipelines using acoustic signals based on wavelet transform and Support Vector Machine,” *Measurement*, vol. 146, pp. 479–489, Nov. 2019, doi: 10.1016/j.measurement.2019.06.050.

[124] S. Li, Y. Song, and G. Zhou, “Leak detection of water distribution pipeline subject to failure of socket joint based on acoustic emission and pattern recognition,” *Measurement*, vol. 115, pp. 39–44, Feb. 2018, doi: 10.1016/j.measurement.2017.10.021.

[125] W. Wang, X. Mao, H. Liang, D. Yang, J. Zhang, and S. Liu, “Experimental research on in-pipe leaks detection of acoustic signature in gas pipelines based on the artificial neural network,” *Measurement*, vol. 183, p. 109875, Oct. 2021, doi: 10.1016/j.measurement.2021.109875.

[126] W. Wang and Y. Gao, “Pipeline leak detection method based on acoustic-pressure information fusion,” *Measurement*, vol. 212, p. 112691, May 2023, doi: 10.1016/j.measurement.2023.112691.

[127] Y. Yu, A. Safari, X. Niu, B. Drinkwater, and K. V Horoshenkov, “Acoustic and ultrasonic techniques for defect detection and condition monitoring in water and sewerage pipes: A review,” *Applied Acoustics*, vol. 183, p. 108282, 2021, doi: https://doi.org/10.1016/j.apacoust.2021.108282.

[128] T. Wang, X. Wang, and M. Hong, “Gas Leak Location Detection Based on Data Fusion with Time Difference of Arrival and Energy Decay Using an Ultrasonic Sensor Array,” *Sensors*, vol. 18, no. 9, p. 2985, Sep. 2018, doi: 10.3390/s18092985.

[129] S. Hamilton and B. Charalambous, *Leak Detection: Technology and Implementation*. 2013. doi: 10.26530/oapen_578133.

[130] E. Pauline, Carreño-Alvarado, and G. R. Meza, “Water Leak Detection by Termographic Image Analysis, In Laboratory Tests,” *Proc West Mark Ed Assoc Conf*, vol. 48, no. 1, p. 15, May 2020, doi: 10.3390/ECWS-4-06440.

[131] M. Nakhkash and S. Ardekani, “Water leak detection using ground penetrating radar,” in *Tenth International Conference on Ground Penetrating Radar*, IEEE Xplore, 2004. doi: 10.1109/ICGPR.2004.179793.

[132] Seung-Yeup Hyun, Yu-Sun Jo, Heon-Cheol Oh, and Se-Yun Kirn, “An experimental study on a ground-penetrating radar for detecting water-leaks in buried water transfer pipes,” in *6th International SYmposium on Antennas, Propagation and EM Theory, 2003. Proceedings. 2003*, IEEE, 2003, pp. 596–599. doi: 10.1109/ISAPE.2003.1276761.

[133] J. H. Goh *et al.*, “Water pipe leak detection using electromagnetic wave sensor for the water industry,” in *2011 IEEE Symposium on Computers & Informatics*, IEEE, Mar. 2011, pp. 290–295. doi: 10.1109/ISCI.2011.5958929.

[134] S. G. Buchberger and G. Nadimpalli, “Leak Estimation in Water Distribution Systems by Statistical Analysis of Flow Readings,” *J Water Resour Plan Manag*, vol. 130, no. 4, pp. 321–329, Jul. 2004, doi: 10.1061/(ASCE)0733-9496(2004)130:4(321).

[135] R. S. Pudar and J. A. Liggett, “Leaks in Pipe Networks,” *Journal of Hydraulic Engineering*, vol. 118, no. 7, pp. 1031–1046, Jul. 1992, doi: 10.1061/(ASCE)0733-9429(1992)118:7(1031).

[136] J. A. Liggett and L. Chen, “Inverse Transient Analysis in Pipe Networks,” *Journal of Hydraulic Engineering*, vol. 120, no. 8, pp. 934–955, Aug. 1994, doi: 10.1061/(ASCE)0733-9429(1994)120:8(934).

[137] D. J. Tritton, *Physical Fluid Dynamics-Oxford Science Publications*, 2nd ed. Clarendon Press, 1988.

[138] G. K. Batchelor, *An Introduction to Fluid Dynamics (Cambridge Mathematical Library)*. Cambridge University Press, 2000.

[139] J. Cengel, Yunus; Cimbala, *Fluid Mechanics: Fundamentals and Applications*, 4th ed. McGraw-Hill Education, 2017.

[140] I. B. I. and A. H. K. L. S. Taura, "The use of a continuity equation of fluid mechanics to reduce the abnormality of the cardiovascular system: A control mechanics of the human heart," *Journal of Biophysics and Structural Biology*, vol. 4, no. 1, Mar. 2012, doi: 10.5897/JBSB11.010.

[141] T. Kambe, *Elementary Fluid Mechanics*. World Scientific Publishing Company, 2007. doi: 10.1142/5895.

[142] R. C. Baker, *Flow Measurement Handbook, Industrial Designs, Operating Principles, Performance, and Applications*, 2nd ed. 2016. doi: 10.1017/cbo9781107054141.

[143] F. Cascetta, "Short history of the flowmetering," *ISA Trans*, vol. 34, no. 3, pp. 229–243, 1995, doi: 10.1016/0019-0578(95)00021-q.

[144] H. M. Shen, X. Fu, J. D. Chen, and P. Ye, "Development of a vortex flowmeter with good performance at low-flowrate," *15th International Flow Measurement Conference 2010, FLOMEKO 2010*, vol. 1, pp. 524–530, 2010.

[145] M. Takamoto, H. Ishikawa, K. Shimizu, H. Monji, and G. Matsui, "New measurement method for very low liquid flow rates using ultrasound," *Flow Measurement and Instrumentation*, vol. 12, no. 4, pp. 267–273, 2001, doi: 10.1016/S0955-5986(01)00023-1.

[146] E. Sanatizadeh, "Experimental and Analytical Study of the Novel Static Flow Meters," 2019.

[147] L. Russell, R. Goubran, F. Kwamena, and F. Knoefel, “Sensor modality shifting in IoT deployment : measuring non-temperature data using tempeSensor modality shifting in IoT deployment:measuring non-temperature data using temperature sensors,” *1*, pp. 1–6, 2017, doi: 10.1109/SAS.2017.7894057.

[148] L. P. WILLIAMS, “Michael Faraday and the Evolution of the Concept of the Electric and Magnetic Field,” *Nature*, vol. 187, no. 4739, pp. 730–733, Aug. 1960, doi: 10.1038/187730a0.

[149] M. Reader-Harris, “Differential Pressure (DP) Flowmeters,” in *Handbook of Measuring System Design*, Chichester, UK: John Wiley & Sons, Ltd, 2005. doi: 10.1002/0471497398.mm260.

[150] M. Wang, D. Zheng, J. Mei, Y. Mao, and J. Hu, “A new method for processing ultrasonic gas flowmeter signal in wet gas,” *IET Science, Measurement & Technology*, vol. 15, no. 1, pp. 2–13, Jan. 2021, doi: 10.1049/smt2.12001.

[151] S. K. J, K. A, K. S. C, S. G, and K. G, “A comprehensive review on accuracy in ultrasonic flow measurement using reconfigurable systems and deep learning approaches,” *AIP Adv*, vol. 10, no. 10, p. 105221, Oct. 2020, doi: 10.1063/5.0022154.

[152] X. Nan, M. Yan, T. Jinghua, H. Liru, and C. Weimin, “Development on Intelligent Small-Flow Target Flow Meter,” in *2009 International Forum on Computer Science-Technology and Applications*, 2009, pp. 315–317. doi: 10.1109/IFCSTA.2009.317.

[153] F. C. L. Almeida, M. J. Brennan, A. T. Paschoalini, P. F. Joseph, and Y. Gao, “On the signum function and its effect on acoustic correlation for leak location in buried plastic water pipes,” *Procedia Eng*, vol. 199, pp. 1344–1349, 2017, doi: 10.1016/j.proeng.2017.09.346.

[154] Z. Ahmad Fuad, H. S. Eddy, Y. Badronnisa, and I. Syazwani, "Water leak detection method in water distribution network," *IOP Conf Ser Earth Environ Sci*, vol. 357, p. 012033, Nov. 2019, doi: 10.1088/1755-1315/357/1/012033.

[155] L. Wong *et al.*, "Leak Detection in Water Pipes Using Submersible Optical Optic-Based Pressure Sensor," *Sensors*, vol. 18, no. 12, p. 4192, Nov. 2018, doi: 10.3390/s18124192.

[156] J. Gong *et al.*, "In-pipe fibre optic pressure sensor array for hydraulic transient measurement with application to leak detection," *Measurement*, vol. 126, pp. 309–317, Oct. 2018, doi: 10.1016/j.measurement.2018.05.072.

[157] Y. Abrahamian, R. Martirossyan, F. Gasparyan, and K. Kocharyan, "Physical Principles of Infrared Radiometric Systems," in *Methods and Materials for Remote Sensing*, Boston, MA: Springer US, 2004, pp. 51–91. doi: 10.1007/978-1-4419-9025-9_2.

[158] S. Adsul, A. K. Sharma, and R. G. Mevekari, "Development of leakage detection system," in *2016 International Conference on Automatic Control and Dynamic Optimization Techniques (ICACDOT)*, IEEE, Sep. 2016, pp. 673–677. doi: 10.1109/ICACDOT.2016.7877671.

[159] J. H. Goh *et al.*, "Water pipe leak detection using electromagnetic wave sensor for the water industry," in *2011 IEEE Symposium on Computers & Informatics*, IEEE, Mar. 2011, pp. 290–295. doi: 10.1109/ISCI.2011.5958929.

[160] MakerBot, "MakerBot Replicator + User Manual," *MakerBot*, 2009. http://www.makerbot.com/wp-content/uploads/2018/09/Replicator_User_Manual.pdf (accessed Jul. 06, 2020).

[161] Uni-Bell PVC Pipe Association, *Handbook of PVC Pipe Design and Construction*, 5th ed. Industrial Press, Inc., 2012.